UNIVERSITY OF CALIFORNIA SAN DIEGO

Coordination of hippocampo-cortical waves and single unit spiking in human memory

A dissertation submitted in partial satisfaction of the
requirements for the degree Doctor of Philosophy

in

Neurosciences
with a Specialization in Computational Neurosciences

by

Charles William Dickey

Committee in charge:

Professor Eric Halgren, Chair
Professor Maxim Bazhenov
Professor Eran Mukamel
Professor Christine Prey Smith
Professor Terrence Sejnowski

2021

The Dissertation of Charles William Dickey is approved, and it is acceptable in quality and form for publication on microfilm and electronically.

University of California San Diego

2021

DEDICATION

To my family, friends, and colleagues

TABLE OF CONTENTS

LIST OF FIGURES

LIST OF TABLES

ACKNOWLEDGEMENTS

I would like to express my gratitude to my advisor, Eric Halgren, for his four years of outstanding mentorship. Over the years, he has impressed upon me the importance of approaching the data from all angles to understand what it does and does not mean. His eye for detail and solution-focused mindset in particular were critical to the success of the work herein. I am especially grateful that when the pandemic was in its infancy, Eric foresaw its long-term consequences, and was able to help me restructure my plans such that I was able to complete my thesis work without delay.

I would also like to acknowledge Bill Moody, whose mentorship during my undergraduate years was crucial for my early scientific development and ensuing decision to pursue a career as a physician scientist. My early career goals were also influenced by Claire Wyart, who gave me the wonderful opportunity to conduct research in Paris before starting medical school, and who helped convince me to do research using patient data in graduate school.

Furthermore, I would like to acknowledge my many professors and colleagues for supporting and inspiring me in more ways than I can count. Thank you to the rest of my committee for providing such thoughtful input that has shaped the work in this dissertation: Maxim Bazhenov, Eran Mukamel, Christine Smith, Terrence Sejnowski. I also indebted to my current and former lab mates: Burke Rosen, Chris Gonzalez, Xi Jiang, Erik Kaestner, Dan Cleary, Jacob Garrett, Adam Niese, Sophie Kajfez, Yihan Zi, Wahab Alasfour, and Zarek Siegel. Notably, I would also like to recognize Ilya Verzhbinsky for his hard work and important contributions to the work in this dissertation.

I am so grateful to my family and friends for providing a persistent source of positivity. Thank you to my mother, Barbara, and my father, Chuck, for always being there when I need you. Thank you to my friend Elischa Sanders for many years of unwavering support.

Importantly, I would like to acknowledge the patients whose data are included in this work as well as the studies that inspired this research. This includes patients with drug-resistant epilepsy who stayed in the hospital for days to weeks while undergoing direct recordings from their brains for seizure

onset localization prior to therapeutic resection. During this diagnostic process, these patients selflessly agreed to participate in our research studies. These patients have made incalculable contributions to the fields of neuroscience, engineering, medicine, and beyond.

As a graduate student I was fortunate to receive the following fellowship that helped make the research in my dissertation possible: Institute for Neural Computation Predoctoral Fellowship in Cognitive Neuroscience.

Chapter 1, in full, is a reprint of the material as it appears in: Dickey CW, Sargsyan A, Madsen JR, Eskandar EN, Cash SS, Halgren E. Travelling spindles create necessary conditions for spike-timing-dependent plasticity in humans. *Nature Communications*. 2021;12(1):1027. doi:10.1038/s41467-021-21298-x.

Chapter 2, in full, is a reprint of the material as it has been written in a manuscript submitted for publication: Dickey CW, Verzhbinsky IA, Jiang X, Rosen BQ, Kajfez S, Eskandar EN, Gonzalez-Martinez J, Cash SS, Halgren E. Cortical ripples provide the conditions for consolidation during NREM sleep in humans. Preprint available at *bioRxiv*. 2021. doi:10.1101/2021.05.11.443637.

Chapter 3, in full, is a reprint of the material as it has been written in a manuscript submitted for publication: Dickey CW, Verzhbinsky IA, Jiang X, Rosen BQ, Kajfez S, Stedelin B, Shih JJ, Ben-Haim S, Raslan AM, Eskandar EN, Gonzalez-Martinez J, Cash SS, Halgren E. Widespread ripples synchronize human cortical activity during sleep, waking, and memory recall. Preprint available at *bioRxiv*. 2021. doi:10.1101/2021.02.23.432582.

VITA

Education

2021 Ph.D., Neurosciences with a Specialization in Computational Neurosciences	University of California San Diego
2014 B.S., Neurobiology	University of Washington
2014 B.F.A., Digital Arts & Experimental Media	University of Washington

Publications

Dickey CW, Verzhbinsky IA, Jiang X, Rosen BQ, Kajfez S, Stedelin B, Shih JJ, Ben-Haim S, Raslan AM, Eskandar EN, Gonzalez-Martinez J, Cash SS, Halgren E. Widespread ripples synchronize human cortical activity during sleep, waking, and memory recall. Preprint available at *bioRxiv*. 2021. doi:10.1101/2021.02.23.432582.

Dickey CW, Verzhbinsky IA, Jiang X, Rosen BQ, Kajfez S, Eskandar EN, Gonzalez-Martinez J, Cash SS, Halgren E. Cortical ripples provide the conditions for consolidation during NREM sleep in humans. Preprint available at *bioRxiv*. 2021. doi:10.1101/2021.05.11.443637.

Dickey CW, Sargsyan A, Madsen JR, Eskandar EN, Cash SS, Halgren E. Travelling spindles create necessary conditions for spike-timing-dependent plasticity in humans. *Nature Communications*. 2021;12(1):1027. doi:10.1038/s41467-021-21298-x.

Knafo S, Fidelin K, Prendergast A, Po-En BT, Parrin A, Dickey CW, Bohm UL, Figueiredo SN, Thouvenin O, Pascal-Moussellard H, Wyart C. Mechanosensory neurons control the timing of spinal microcircuit selection during locomotion. Calabrese RL, ed. *eLife*. 2017;6:e25260. doi:10.7554/eLife.25260.

Easton CR, Dickey CW, Moen SP, Neuzil KE, Barger Z, Anderson TM, Moody WJ, Hevner RF. Distinct calcium signals in developing cortical interneurons persist despite disorganization of cortex by Tbr1 KO. *Developmental Neurobiology*. 2016;76(7):705-20. doi:10.1002/dneu.22354.

Conference Presentations

Kavli Symposium, Oral Presentation (2020)
iEEG Workshop, Oral Presentation (2019)
Society for Neuroscience, First Author Poster (2018)
Mary Gates Research Symposium, Oral Presentation (2014)
Society for Neuroscience, First Author Poster (2013)
Mary Gates Research Symposium, First Author Poster (2013)

Awards

Institute for Neural Computation Predoctoral Fellowship in Cognitive Neuroscience (2019 – 2020)
Chancellor's Interdisciplinary Collaboratories Fellowship (2017 – 2019)
Phi Beta Kappa (2014)
Gonfaloniere at University of Washington Commencement (2014)
Mary Gates Research Scholarship (2014)
Mary Gates Travel Award (2013)

Mary Gates Research Scholarship (2013)

Research Experience

Ph.D. Candidate (2017 – present)
Advisor: Professor Eric Halgren, Ph.D., Departments of Neurosciences and Radiology, University of California San Diego

Post-Baccalaureate Researcher (2014 – 2015)
Supervisor: Dr. Claire Wyart, The Brain and Spine Institute, Paris, France

Undergraduate Researcher (2012 – 2015)
Supervisor: Professor William Moody, Department of Biology, University of Washington

Undergraduate Researcher (2011 – 2012)
Supervisor: Lise Johnson, Center for Sensorimotor and Neural Engineering, University of Washington

Volunteering Experience

UCSD Pacific Beach Free Clinic, Neurology Clinic Manager (2016 – 2017)
UCSD Pacific Beach Free Clinic, Labs Manager (2016 – 2017)
Full Life Care: Adult Health and Disability Services (2014 – 2015)

Fields of Study

Major Field: Neurosciences
Specialization: Computational Neurosciences

ABSTRACT OF THE DISSERTATION

Coordination of hippocampo-cortical waves and single unit spiking in human memory

by

Charles William Dickey

Doctor of Philosophy in Neurosciences with a Specialization in Computational Neurosciences

University of California San Diego, 2021

Professor Eric Halgren, Chair

In mammals, the consolidation of memories from previous waking is facilitated through the coordination of hippocampo-cortical waves during non-rapid eye movement sleep (NREM). Specifically, it is thought that consolidation in the cortex is guided by the coordination of cortical sleep waves (downstates, spindles, upstates) with high-frequency oscillations in the hippocampus called 'ripples,' which in rodents mark the replay of neuronal firing sequences established during waking. However, it is not well-understood how these waves facilitate plasticity. While it has been shown that cortical ripples are involved in memory recall in humans, it is not known whether they are generated during human sleep.

Furthermore, it remains unknown how the different elements of a memory are bound across the cortex into a cohesive representation. In this dissertation, I collected and analyzed human intracranial macro- and micro-electrode recordings to investigate how interactions between cortical waves, hippocampal waves, and single unit spiking may underlie memory during sleep and waking. Chapter 1 shows how sleep spindles modulate neuron spike-timing to create conditions necessary for spike-timing-dependent plasticity (STDP). This study reveals that spindles facilitate short latency co-firing between neurons that may lead to STDP. Furthermore, it reports the spatial organization and propagation of spindles and spiking within a few millimeters of cortex. Chapter 2 provides the first report and comprehensive characterization of 80 Hz cortical ripples during human NREM, and provides evidence for their role in memory consolidation. This study shows that ripples are ubiquitous throughout the cortex during NREM as well as waking. During sleep, cortical ripples occur during spindles on down-to-upstates, with unit-firing patterns suggesting generation by pyramidal-interneuron feedback. Furthermore, cortical ripples mark the recurrence of spatiotemporal activity patterns from preceding waking and group co-firing, which could further enhance spindle-mediated STDP. Chapter 3 reveals that ripples occur simultaneously in multiple lobes in both hemispheres, and in the hippocampus, generally during sleep and waking, and with enhancements preceding memory recall. Ripples phase-lock local cell-firing, and phase-synchronize with little decay between locations separated by up to 25 cm, enabling long distance integration. Indeed, co-rippling sites have increased correlation of very-high-frequency activity which reflects cell-firing. Thus, ripples may help bind information across the cortex in memory.

Chapter 1: Travelling spindles create necessary conditions for spike-timing-dependent plasticity in humans

Abstract:

Sleep spindles facilitate memory consolidation in the cortex during mammalian non-rapid eye movement sleep. In rodents, phase-locked firing during spindles may facilitate spike-timing-dependent plasticity by grouping pre-then-post-synaptic cell firing within ~25ms. Currently, microphysiological evidence in humans for conditions conducive for spike-timing-dependent plasticity during spindles is absent. Here, we analyze field potentials and unit firing from middle/upper layers during spindles from 10x10 microelectrode arrays at 400μm pitch in humans. We report strong tonic and phase-locked increases in firing and co-firing within 25ms during spindles, especially those co-occurring with down-to-upstate transitions. Co-firing, spindle co-occurrence, and spindle coherence are greatest within ~2mm, and high co-firing of units on different contacts depends on high spindle coherence between those contacts. Spindles propagate at ~0.28m/s in distinct patterns, with correlated cell co-firing sequences. Spindles hence organize spatiotemporal patterns of neuronal co-firing in ways that may provide pre-conditions for plasticity during non-rapid eye movement sleep.

Introduction:

Sleep spindles are bursts of 10-16Hz oscillations that last for 0.5-2s at the scalp and occur spontaneously during mammalian non-rapid eye movement (NREM) sleep (Fernandez et al., 2020). It is widely accepted that spindles are important for memory consolidation (Klinzing et al., 2019). Spindles are generated by an interaction of intrinsic currents and local circuits within the thalamus (Destexhe et al., 2003; McCormick et al., 2015), and are projected to all cortical areas (Mak-McCully et al., 2017; Piantoni et al., 2017). Spindles often occur on upstates following downstates (Gonzalez et al., 2018; Mak-McCully et al., 2017).

In the two-stage model of memory, short-term memories are encoded in the hippocampus and then subsequently consolidated into long-term storage by repeated activation of cortical networks during sleep (Buzsáki, 1998; McClelland et al., 1995). It is hypothesized that hippocampal-to-cortical transfer of memories involves the replay of cell firing sequences during sleep (Skaggs et al., 1996), correlated with hippocampal sharp-wave ripples, cortical slow oscillations, and cortical spindles (Buzsaki, 2015; Jiang et al., 2019a, 2019b; Jiang et al., 2017; Johnson et al., 2010). Disrupting this association in rodents impairs consolidation (Maingret et al., 2016), and spindle density is correlated with consolidation in humans (Cox et al., 2012; Mednick et al., 2013), suggesting that cortical spindles contribute to the consolidation process (Diekelmann et al., 2010). However, the mechanisms underlying this phenomenon are not well understood.

It was first proposed that spindles facilitate plasticity by Timofeev et al. (2002), who showed that spindles in cats are associated with long-term changes of responsiveness in cortical neurons. Recent studies in rodents have shown that spindles are associated with dendritic Ca^{2+} influxes (Seibt et al., 2017), which may be enhanced through coupling with down-to-upstates (Niethard et al., 2018), and could support plasticity underlying memory consolidation. In support of this hypothesis, *in vitro* stimulation of rat cortical pyramidal cells pattern matched to *in vivo* firing sequences during spindles promotes Ca^{2+}-dependent long-term potentiation (LTP) of excitatory postsynaptic potentials (Rosanova et al., 2005). Potentiation was dependent on coordinated pre-synaptic potentials and post-synaptic spiking. These observations suggest that spindles may promote spike-timing-dependent plasticity (STDP), which is a Ca^{2+}-dependent mechanism where correlated pre- and post-synaptic spiking within a short time window modulates synaptic strength (Feldman, 2012). In the standard model, STDP facilitates LTP when pre-synaptic spiking occurs within 25ms before post-synaptic spiking, or long-term depression (LTD) when the post-synaptic cell fires first.

Indirect evidence in humans supports the hypothesis that spindles facilitate STDP. Specifically, electrocorticography recordings show that spindles travel across the cortex at ~3-9m/s, which may be optimal for inducing STDP across distant regions (Muller et al., 2016). Furthermore, intracranial studies

show that spindle phase modulates high gamma (Gonzalez et al., 2018; Hagler et al., 2018), which may reflect increased cortical unit co-firing, required for STDP. However this remains controversial as a previous human intracranial study did not find an increase in unit spiking during spindles (Andrillon et al., 2011). While several limitations preclude the recording of dendritic Ca^{2+} currents in humans, it is possible to test if the unit spike timing requirements for STDP are fulfilled during spindles. Specifically, the most prominent requirement for STDP is co-firing within 25ms.

Here, we analyzed intracranial microelectrode recordings from a 10x10 grid at 400μm pitch in cortical supragranular layers II/III, and possibly as low as layer IV, in patients undergoing evaluation of pharmaco-resistant intractable epilepsy. We detected putative pyramidal (PY) and interneuron (IN) units and spindles in the local field potential (LFP). Cortical firing was strongly modulated with spindle phase, and increased tonically during spindles, especially when co-occurring with a down-to-upstate. Critically, co-firing within 25ms of cells recorded by different contacts strongly increased during spindles beyond even what would be expected from the increased firing rate, fulfilling a critical precondition for STDP. Some unit pairs had a preferred order of co-firing, which could support directional plasticity. Spindles tended to co-occur and were highly coherent within ~1.5-2.0 mm, and increased co-firing of units on different contacts was highly enriched when those contacts had highly coherent spindles. Spindles and associated co-firing propagated at ~0.28m/s with multiple patterns within and between spindles. Thus, spindles spatiotemporally organize neuronal co-firing on a sub-centimeter scale in a manner that could facilitate plasticity across multiple networks.

Results:

Characterizations of units and spindles

A mean and standard deviation of 133±50 minutes of NREM sleep data was selected for analysis from recordings by the Utah Array implanted in supragranular layers II/III, and possibly as low as granular layer IV, of the superior or middle temporal gyrus in 4 patients (Table 1.1; Fig. 1.1A-B) with focal epilepsy undergoing monitoring for seizure localization prior to resection. A total of 156 PYs, 39

INs, and 158 MUs were detected, classified, and analyzed (Fig. 1.1C-F; see Supplementary Fig. 1.1 for quality and isolation metrics). Therefore, among the single units, 80% were PY and 20% were IN. A total of 340,743 sleep spindles were analyzed across 265 average referenced channels. The mean and standard deviation spindle density per channel was 10.82±3.39 occurrences/minute, duration was 470.32±174.32ms (Supplementary Fig. 1.2A), and oscillation frequency was 12.52±1.18Hz (Supplementary Fig. 1.2B), which are consistent with previous intracranial studies in humans (Hagler et al., 2018; Mak-McCully et al., 2017). The mean and standard deviation percent of spindles during which there was at least one spike on the same recording contact from a PY was 7.92±7.33% and from an IN was 36.46±24.31%. The mean and standard deviation percent of co-occurring spindles on different contacts when there was at least one spindle occurring was 29.46±17.11% (Supplementary Fig. 1.2D).

Table 1.1. Patient demographics, array implantation locations, and unit characteristics. The total units and total spikes for each unit type across all four patients are reported. The mean and standard deviation across units for all patients for valley-to-peak amplitude, firing rate, valley-to-peak width, half peak width, and bursting index are reported. PY=pyramidal unit, IN=interneuron unit, MU=multi-unit.

Patient Demographics and Array Implantation						
Patient	Age	Sex	Handedness	Utah Array implantation location	Probe length (mm)	Recording time (min)
1	51	F	R	Left middle temporal gyrus	1.0	200
2	31	M	L	Left superior temporal gyrus	1.5	132
3	47	M	R	Right middle temporal gyrus	1.5	120
4	21	M	R	Left middle temporal gyrus	1.0	80

Unit Characteristics							
Unit Type	Total Units	Total Spikes	Valley-to-Peak Amplitude (μV)	Firing Rate (Hz)	Valley-to-Peak Width (ms)	Half Peak Width (ms)	Bursting Index
PY	156	352992	84.02 ± 59.45	0.19 ± 0.17	0.49 ± 0.057	0.61 ± 0.038	0.046 ± 0.033
IN	39	785571	41.60 ± 26.09	1.71 ± 1.70	0.30 ± 0.054	0.35 ± 0.052	0.012 ± 0.016
MU	158	5256429	26.53 ± 14.89	2.82 ± 2.68	0.48 ± 0.086	0.57 ± 0.070	0.046 ± 0.033

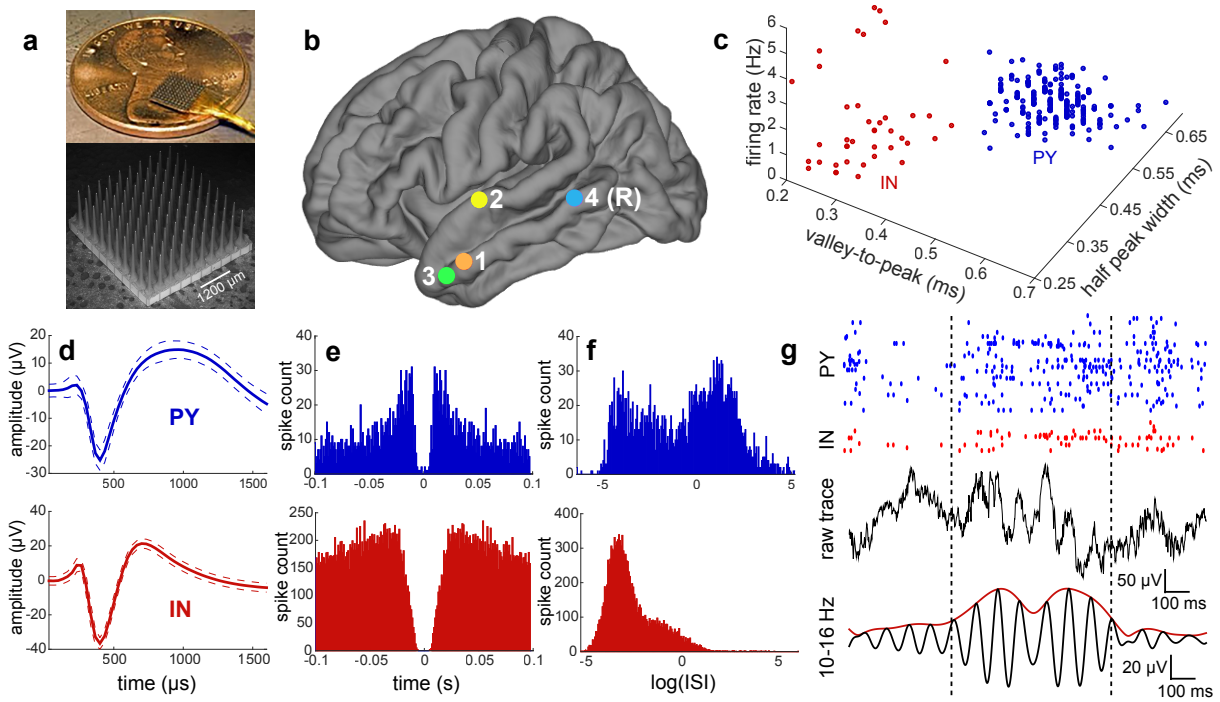

Fig. 1.1. Array implantation, single unit classification, spindle detection, and unit spiking during spindles. (**A**) Images of the Utah Array. (**B**) Utah Array implantation locations for all 4 patients. All sites of implantation were on the left except for patient 4, which was on the right (R). (**C**) PY (blue) and IN (red) form separate clusters based on mean waveform half peak width duration, valley-to-peak duration, and firing rate. (**D-F**) Mean and standard deviation spike waveform (**D**), spike autocorrelation (**E**), and ISI distribution (**F**) for an example PY and IN. (**G**) Raw and 10-16Hz bandpassed traces of an example spindle with raster plot of associated spiking of an example PY and IN. IN=putative interneuron unit, PY=putative pyramidal unit.

Spindles are associated with an increase in unit spike rates

Prior to testing for co-firing by pairs of units during spindles, our main focus, we characterized neuronal firing during spindles because they provide the context of such co-firing. Specifically, increased firing during spindles, clustered at consistent phases, could result in increased co-firing. Spike rates for each unit were quantified and analyzed during spindles detected on the unit's channel and compared to baseline, which was comprised of randomly selected epochs in between spindles on the same channel that were matched in number and duration to the spindles. PYs and INs increased firing during spindles (Fig. 1.2A-B). The mean and standard deviation baseline spike rate of PYs was 0.15±0.16Hz and INs was 1.61±1.63Hz. The mean and standard deviation spike rate during spindles for PYs was 0.25±0.29Hz and

INs was 2.33±2.35Hz. There was a significant increase in the mean percent of baseline spike rate during spindles for PYs of 226.97±18.41% (SEM) and for INs of 180.13±21.95% (Fig. 1.2B, p_{PY}=6e-22, p_{IN}=6e-6, Bonferroni-corrected α=0.025 for 2 unit types, one sample two-sided Wilcoxon signed-rank test, z_{PY}=9.64, z_{IN}=4.54). The increase in spike rates during spindles was present for individual patients (Supplementary Table 1.1A) and also for shorter (<500ms) compared to longer (>500ms) spindles (Supplementary Fig. 1.3). MU spiking is reported in Supplementary Fig. 1.4A-D. At shorter distances to spindles, units had higher spike rates, and this fall off across distance was sharper for PYs than INs within the first millimeter (Supplementary Fig. 1.5).

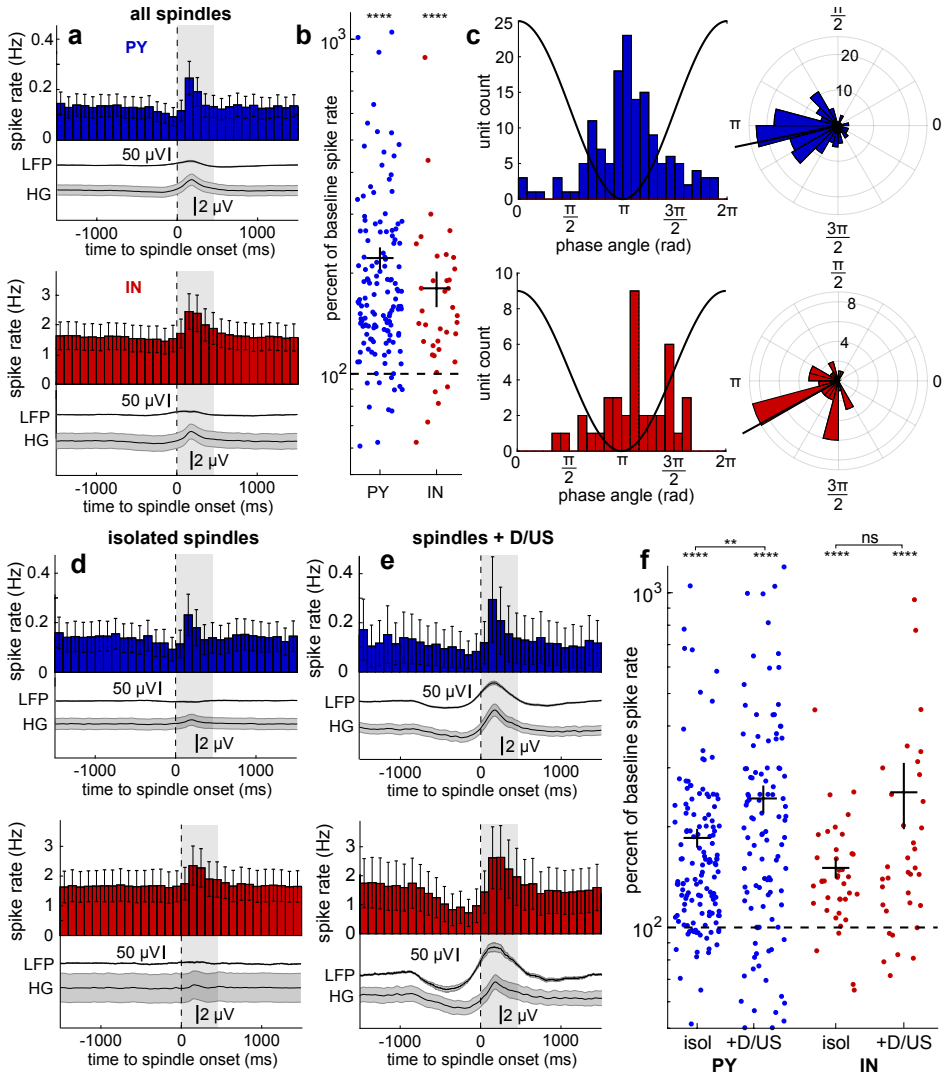

Fig. 1.2. Single unit spiking during spindles. (**A**) Mean PY (n=156) and IN (n=39) spike rates and associated mean LFP and HG envelope locked to spindle onsets at t=0. Shaded gray box shows the mean spindle duration of 470ms. (**B**) PY (n=156) and IN (n=39) spike rates during concatenated spindle epochs as a log-percent of baseline spike rates (p_{PY}=6e-22, p_{IN}=6e-6). Baseline spike rate of each unit was computed as the spike rate during concatenated randomly selected NREM sleep epochs between spindles that were matched in number and duration. Color circles represent units. Solid horizontal lines show mean and vertical show SEM. Dashed horizontal line shows baseline spike rate (100%). (**C**) Non-polar and polar histograms show circular mean spindle phases of spiking for PYs and INs. One cycle of a spindle is superimposed on non-polar histograms to visualize the phase-spike timing relationship. Black lines extending from polar histograms show circular means. (**D-E**) Same as (A) except for isolated spindles (**D**), which were those that did not coincide with down/upstates, and spindles that coincided with down/upstates (**E**). (**F**) Same as (B) except for isolated spindles ("isol"; p_{PY}=7e-18, p_{IN}=1e-6 for spiking compared to baseline) and spindles that coincided with down or upstates ("+D/US") (p_{PY}=4e-11, p_{IN}=4e-5 for spiking compared to baseline; p_{PY}=0.003, p_{IN}=0.22 for isol vs. +D/US). HG=high gamma, IN=putative interneuron unit, LFP=local field potential, NREM=non-rapid eye movement, PY=putative pyramidal unit, ISI=inter-spike interval. Error bars and shaded errors show SEM. **p<0.01, ****p<0.0001, one sample two-sided Wilcoxon signed-rank test for comparisons with baseline, paired two-sided Wilcoxon signed-rank test for isol vs. +D/US.

Unit spiking phase-locks to the spindle with PY preceding IN

Grouping of unit spikes by spindle phase could further increase the probability of co-firing between units. PY and IN each had prominent increases in unit spike rates locked to the spindle trough (Supplementary Fig. 1.6). The circular mean spindle phase of spikes across the PY (n=145) and IN (n=39) that spiked during spindles was 3.39rad and 3.64rad, respectively (Fig. 1.2C). There was a significant spindle phase preference of 17.24% of PYs and 64.10% of INs (α=0.05, Hodges-Ajne test with bootstrapping). For units with significant spindle phase preferences, the circular mean spindle phase of spikes across PYs was 3.30rad (Supplementary Fig. 1.7A) and INs was 3.99rad (Supplementary Fig. 1.7B). There was a significant difference between the circular mean spindle phase angle distributions of PY spikes vs. IN spikes, with PY spikes preceding IN spikes (p=0.023, parametric Watson-Williams multi-sample test) for units with a significant phase preference. For 10-16 Hz spindles, this corresponds to a 6.86-10.98ms delay from PY to IN spiking, and for the mean spindle frequency of 12.52Hz that we calculated, this corresponds to a 8.77ms delay. See Supplementary Table 1.1B for results from individual patients. MU spike-phase results are reported in Supplementary Fig. 1.4E and Supplementary Fig. 1.7C.

Unit spiking increases more during spindles coupled to down-to-upstates

Spindles often occur during upstates (Mak-McCully et al., 2017), and this coupling appears to be important for memory consolidation (Klinzing et al., 2019). We sought to identify such spindles that coincided with either downstates (which are typically followed by upstates) or upstates (which are typically preceded by downstates) (Supplementary Fig. 1.8). We found that 45.11% of spindles did not begin within ±1000ms of downstates or upstates (henceforth referred to as “isolated” spindles), and 7.78% had a downstate peak within 750ms preceding spindle onset and 6.36% had an upstate peak within 500ms following spindle onset. The remainder of spindles had downstate or upstate peaks outside of these windows but within ±1000ms of the spindle (e.g., downstates with peaks following spindle onset) and/or had large positive or negative deflections that were not confirmed as downstates or upstates based on

changes in high gamma but were excluded to reduce the chance of contamination of the isolated spindle group by downstates or upstates. There was a significant increase in the baseline spike rate during isolated spindles for PYs of 185.17±11.98% (SEM) and for INs of 150.66±10.35% (Fig. 1.2D,f; p_{PY}=7e-18, p_{IN}=1e-6, Bonferroni-corrected alpha=0.025 for 2 unit types, one sample two-sided Wilcoxon signed-rank test, z_{PY}=8.61, z_{IN}=4.87). There was no significant difference for spindles that coincided with downstates vs. those that coincided with upstates (p_{PY}=0.11, p_{IN}=0.79, Bonferroni-corrected α=0.025 for 2 unit types, paired two-sided Wilcoxon signed-rank test, z_{PY}=-1.61, z_{IN}=0.26). Therefore, for the remainder of our analyses on spindle interactions with downstates and upstates, we pooled these events into spindles that coincided with down or upstates. There was a significant increase in spindles that coincided with down/upstates for PYs of 243.06±22.66% and for INs of 253.62±56.94% (Fig. 1.2E-F; p_{PY}=4e-11, p_{IN}=4e-5, Bonferroni-corrected α=0.025 for 2 unit types, one sample two-sided Wilcoxon signed-rank test, z_{PY}=6.62, z_{IN}=4.10; see Supplementary Fig. 1.9 for separate spindles coinciding with downstates or upstates results). Furthermore, there was a significantly greater increase in PY spiking during spindles that coincided with down/upstates vs. isolated spindles (p_{PY}=0.003, p_{IN}=0.22, Bonferroni-corrected α=0.025 for 2 unit types, paired two-sided Wilcoxon signed-rank test, z_{PY}=2.94, z_{IN}=1.23). Therefore, PY and IN spiking increase during spindles and the increase in PY spiking in particular is enhanced when spindles coincide with down/upstates.

Spindles group unit pair co-firing within the window of STDP

Having established that cortical cells fire more during spindles, that this firing is phase-locked to individual spindle waves, and is accentuated during down-to-upstates, we turned to our main focus, whether firing is increased within the 25ms window of STDP during spindles. Unit pair co-firing was quantified by computing peri-spike time occurrences of spikes from all pairs of simultaneously-recorded units, excluding pairs where both units were detected on the same contact. We plotted the spike rate in 1ms bins across 8026 PY_1-PY_2 pairs of units during non-spindle epochs (Fig. 1.3A), spindles (Fig. 1.3B), isolated spindles that did not coincide with downstates or upstates (Fig. 1.3C), and spindles that coincided

with down or upstates (Fig. 1.3D), as well as the same for 2127 PY_1-IN_2 (Fig. 1.3E-H), 580 IN_1-IN_2 (Supplementary Fig. 1.10a-d), and 2127 IN_1-PY_2 (Supplementary Fig. 1.10e-h) pairs. For all four types of unit pairs, the spindle distributions were shifted upward and there was a concentrated increase within ~±25ms for spindle vs. non-spindle epochs, reflecting overall and specific increases in co-firing during spindles. To test the statistical significance of this increase in co-firing within 25ms, we compared the number of spikes from one unit that occurred within 25ms before the spikes of another unit for all possible pairs during co-occurring spindles at those two sites individually vs. 1000 sets of randomly selected non-spindle epochs matched in number and duration. There was a significant increase in unit pair co-firing within 25ms for 16.01% of PY_1-PY_2, 44.66% of IN_1-IN_2, 26.28% of PY_1-IN_2, and 32.96% of IN_1-PY_2 pairs during spindles vs. non-spindle epochs (α=0.001, bootstrapped significance, Table 1.2A). See Supplementary Table 1.2A for results from individual patients.

Table 1.2. Significance of paired and ordered unit co-firing. (**A-C**) Percent of unit pairs with significantly increased (α=0.001, bootstrapped significance) co-firing within 25ms during spindles vs. non-spindles (**A**), spindles vs. shuff-spindles (**B**), and both (**C**). (**D**) Percent of unit pairs in (C), which also had a minimum number of co-firing events of 10, with significant order preference of co-firing within 25ms (α=0.05. two-sided χ^2 test of proportions).

Unit Pair (1→2)	a Paired co-firing: spindles vs. non-spindles	b Paired co-firing: spindles vs. shuff-spindles	c Paired co-firing: Both	d Ordered co-firing
PY_1-PY_2	16.01%	6.18%	5.41%	19.15%
IN_1-IN_2	44.66%	32.41%	25.00%	15.52%
PY_1-IN_2	26.28%	7.10%	5.88%	16.67%
IN_1-PY_2	32.96%	11.05%	10.06%	21.31%

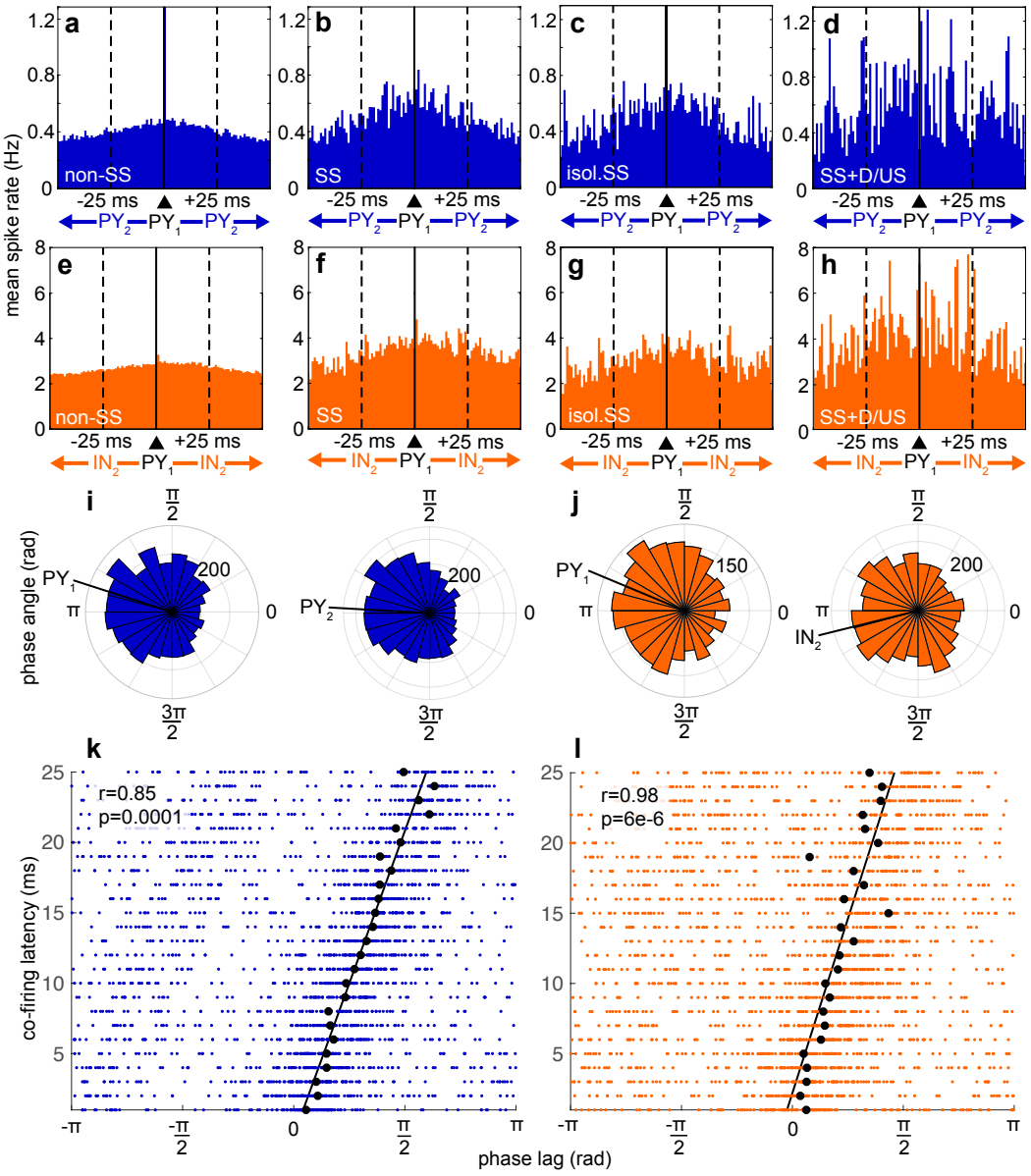

Fig. 1.3. Unit pair co-firing during spindles. (**A-D**) In all pairs of PY recorded from different contacts, the firing of one (PY_2) is plotted relative to the time of the other (PY_1, at t=0) during non-spindle (baseline) epochs (**A**), co-occurring spindles (**B**), isolated co-occurring spindles that did not coincide with down/upstates (**C**), and co-occurring spindles that coincided with down/upstates (**D**). Solid vertical line shows t=0. Dashed vertical lines show the ±25ms interval where paired pre- and post-synaptic spiking facilitates STDP. (**E-H**) Same as (A-D), except for PY_1-IN_2. (**I**) Polar histograms showing spindle phases of PY_1 and PY_2 spikes when there was co-located co-firing during co-occurring spindles within 25ms. Phases are according to the spindle detected on the same channel as PY_1. Black lines show circular means. (**J**) Same as (I) except for PY_1-IN_2. (**K**) Co-firing within 25ms as a function of spindle phase lag. Co-located unit pair co-firing was identified during co-occurring spindles, and the phase lag of the spindle was computed between the spindles on the two channels co-located with the two units. Black circles indicate circular means for each 1ms binned latency and black line indicates circular-linear best fit of these means. P-value reports the significance of the correlation coefficient. (**l**) Same as (K) except for PY_1-IN_2.

Increased co-firing during spindles is not only due to increased spike rates

Increased co-firing within the 25ms window of STDP during spindles could simply be due to the tonic increase in spike rates during spindles vs. baseline. However, unit co-firing distributions have steeper slopes within 25ms during spindles (Fig. 1.3A-H and Supplementary Fig. 1.10), indicating a specific increase in co-firing. To test if unit pair co-firing increases within 25ms during spindles independent of firing rates, we compared unit pair co-firing within 25ms during spindles vs. shuff-spindles (spindles with spike times of each unit randomly shuffled 1000 times). Of note, since the shuffling occurs within spindles, any neuronal drift over time would apply equally to both organized and control spike rates. There was a significant increase in paired spiking during spindles vs. shuff-spindles for 6.18% of PY_1-PY_2, 32.41% of IN_1-IN_2, 7.10% of PY_1-IN_2, and 11.05% of IN_1-PY_2 (α=0.001, bootstrapped significance, Table 1.2B). About 85% of these unit pairs also increased co-firing significantly during spindles vs. non-spindles (5.41% of PY_1-PY_2, 25.00% of IN_1-IN_2, 5.88% of PY_1-IN_2, and 10.06%, α=0.001, bootstrapped significance, Table 1.2C). Therefore, the increase in unit pair co-firing during spindles is due not only to the overall firing rate increase, but also to a specific grouping within 25ms, which is consistent with spindle phase-locked firing. See Supplementary Table 1.2B-C for results from individual patients.

Co-firing is greatest during spindles coupled to down-to-upstates

We next tested whether spindles associated with downstates or upstates had a greater increase in co-firing within 25ms. We computed the average co-firing rate across unit pairs based on the spikes of PY_1 or IN_1 within the 25ms preceding the spikes of PY_2 or IN_2. The mean and SEM co-firing rate for baseline vs. isolated spindles vs. spindles that coincided with down/upstates for PY_1-PY_2 was 0.44±0.0072 vs. 0.56±0.029 vs. 0.66±0.063 Hz (Fig. 1.3A,C,D), for PY_1-IN_2 was 2.76±0.071 vs. 3.27±0.15 vs. 4.60±0.32 Hz (Fig. 1.3E,G,H). The co-firing rate during isolated spindles was significantly higher than non-spindles ($p_{PY\text{-}PY}\approx0$, $p_{PY\text{-}IN}$=9e-33, Bonferroni-corrected α=0.025 for 2 spindle types,

paired two-sided Wilcoxon signed-rank test, $z_{PY\text{-}PY}$=41.93, $z_{PY\text{-}IN}$=11.92), and the co-firing rate during spindles that coincided with down/upstates was significantly higher than during isolated spindles ($p_{PY\text{-}PY}$=8e-24, $p_{PY\text{-}IN}$=5e-11, Bonferroni corrected α=0.025 for 2 spindle types, paired two-sided Wilcoxon signed-rank test, $z_{PY\text{-}PY}$=10.07, $z_{PY\text{-}IN}$=6.57). Therefore, there is an increase in unit pair co-firing during spindles that is enhanced when spindles coincide with down-to-upstates. Results for IN_1-IN_2 and IN_1-PY_2 are reported in Supplementary Fig. 1.10.

Unit pairs have ordered co-firing during spindles

In the canonical model, STDP is an order-dependent process that can lead to LTP or LTD (Feldman, 2012). We first tested whether the unit pairs with significant co-firing were significant in one direction or both directions. Among pair sets that were at least significant in one direction, about 15-25% of PY_1-PY_2 and 55-65% of IN_1-IN_2 were significant in both directions (Supplementary Table 1.3). Next, we tested whether unit pairs with significantly increased co-firing within 25ms for both spindles vs. non-spindles and spindles vs. shuff-spindles had a preferred order of firing within this window. Of 94 PY_1-PY_2, 116 IN_1-IN_2, 72 PY_1-IN_2, and 183 IN_1-PY_2 pairs, which were only those with ≥10 co-firing spikes within ±25ms, 19.15% of PY_1-PY_2, 15.52% of IN_1-IN_2, 16.67% of PY_1-IN_2, and 21.31% of IN_1-PY_2 had a preferred order of co-firing within 25ms (α=0.05, two-sided χ^2 test of proportions, Table 1.2D). See Supplementary Table 1.2D for results from individual patients.

Co-firing delays are correlated with spindle phase lags

Since unit spiking is locked to spindle phase and there is an increase in co-firing during spindles, we tested whether co-firing was also locked to spindle phase. For PY_1-PY_2, when PY_2 fired within 25ms following PY_1, PY_1 spikes had a circular mean spindle phase of 2.83rad and PY_2 spikes had a circular mean phase of 3.07rad (Fig. 1.3I), as measured according to the phases of the spindle co-located with PY_1. Likewise for PY_1-IN_2, PY_1 had a circular mean phase of 2.75rad and IN_2 had a circular mean phase of 3.22rad (Fig. 1.3J). There was no significant difference between spindle phase of PY_1 in PY_1-PY_2 vs.

PY_1 in PY_1-IN_2, or between spindle phase of PY_2 in PY_1-PY_2 vs. IN_2 in PY_1-IN_2 ($p=0.11$ and $p=0.91$, respectively, Bonferroni-corrected $\alpha=0.025$ for 2 pair types, parametric Watson Williams multi-sample test). When we analyzed co-firing delay vs. circular mean spindle phase lag, computed between the spindles co-located with each unit, there was a significant circular-linear relationship for both PY_1-PY_2 (Fig. 1.3K, $r=0.85$, $p=0.0001$, upper tail probability of the χ^2 distribution) and PY_1-IN_2 (Fig. 1.3L, $r=0.98$, $p=6e-6$, upper tail probability of the χ^2 distribution). Thus, when two cells recorded by different contacts fire within 25ms of each other during spindles, the latency between their spikes is highly correlated with the phase lag between the spindles recorded by the two contacts.

Increased co-firing during spindles is enhanced at short distances

The proportion of unit pairs with significantly increased co-firing within 25ms during spindles vs. shuff-spindles had a significant negative linear relationship to contact separation for PY_1-PY_2 (Fig. 1.4A, $r=-0.39$, $p=0.02$, significance of the correlation coefficient), indicating that at shorter distances there is more organized 25ms co-firing. The increased tendency of cortical neurons to fire within 25ms of each other was confirmed with the spike time tiling coefficient (Cutts et al., 2014), an alternative analysis method that is independent of firing rates, for both PY_1-PY_2 and IN_1-IN_2. This method also revealed a similar drop-off in co-firing with distance (Supplementary Fig. 1.11). Based on the relationship between co-firing and distance (Fig. 1.4A), as well as the previously reported neuron densities in human anterior temporal lobe (DeFelipe et al., 2002), we estimated that the number of layer III PY that co-fire more during spindles with a given PY within a radius of 4mm, beyond what would be expected from a simple increase in firing rate, was 37,532 (see Methods).

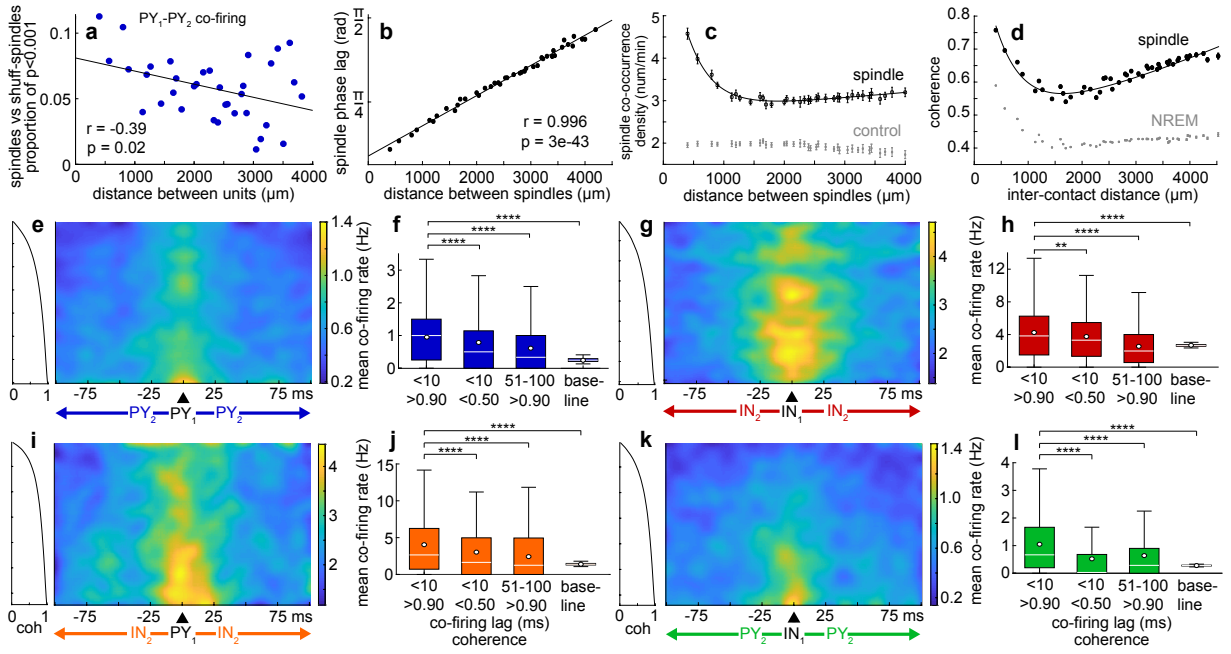

Fig. 1.4. Spindle coherence and unit pair co-firing. (**A**) Mean proportion of unit pairs with significant co-firing within 25ms for spindles vs. shuff-spindles over inter-contact distance for PY_1-PY_2. Shuff-spindles=spindles with spike times randomly shuffled 1000 times. (**B**) Magnitude of the phase lag between co-occurring spindles as a function of distance (n=1000 minimum spindle pairs per bin). P-values in (A-B) report the significance of the correlation coefficient. (**C**) Density of co-occurrence of spindle pairs (black) and spindles with inter-spindle intervals randomly shuffled 100 times for each channel of each channel pair (gray) over distance (n=100 minimum channel pairs per bin). (**D**) Magnitude squared coherence in the 10-16Hz band during co-occurring spindles (black) and during randomly selected NREM epochs matched in number and duration (gray) over distance (n=100 minimum channel pairs per bin). (**E**) PY_1-PY_2 heatmaps of unit pair co-firing rates in pseudo-color as a function of co-firing delay on the abscissa and spindle-spindle coherence within the 10-16Hz band on the ordinate. Co-firing values are in 1ms bins and coherence values are binned with a minimum numbers of spindles per bin (see Methods) with the coherence indicated in the plot on the left (coherence increases non-linearly from 0 to 1 from north to south). Heatmaps were smoothed with a 2D Gaussian filter with α=5. (**F**) Mean co-firing rates were quantified from the data in **e** within heatmap regions with shorter co-firing delays (<10ms) and higher coherence (>0.90) in the left distribution (n=777 bins), compared to shorter delays and lower coherence (<0.50) (p=3e-4, n=525 bins), longer delays (51-100ms) and higher coherence (p=4e-39, n=4736 bins), and longer delays and lower coherence during baseline NREM periods in between spindles (p=9e-17, n=102 bins). (**G-L**) Same as (E-F), except for IN_1-IN_2 (**G-H**) (first comparison: p=0.0042, n=798 and n=651 bins; second comparison: p=6e-46, n=798 and n=4864 bins; third comparison: p=5e-6, n=798 and n=102 bins), PY_1-IN_2 (**I-J**) (first comparison: p=8e-5, n=861 and n=315 bins; second comparison: p=1e-43, n=861 and n=5248 bins; third comparison: p=2e-11, n=861 and n=102 bins), and IN_1-PY_2 (**K-L**) (first comparison: p=3e-16, n=756 and n=441 bins; second comparison: p=4e-29, n=756 and n=4608 bins; third comparison: p=4e-11, n=756 and n=102 bins). Boxplot central line shows median, circle shows mean, box limits show lower and upper quartiles, whiskers show 1.5 × interquartile range, and outliers are not depicted. Heatmaps were smoothed with a 2D Gaussian filter with α=5. **p<0.01, ****p<0.0001, Bonferroni-corrected α=0.017 for 3 comparisons of delay/coherence, two sample two-sided t-test.

Spindles propagate across the microarray at a characteristic velocity

Spindles have previously been shown to propagate across the cortex on a macro-scale, which was proposed as a mechanism for facilitating STDP between distant cortical regions (Muller et al., 2016). The velocity of a traveling wave that oscillates at a known frequency can be calculated based on its phase lag across distance. We found a significant positive linear relationship between distance and the magnitude of the spindle phase lag between co-occurring spindles (Fig. 1.4B, r=0.996, p=3e-43, significance of the correlation coefficient). This strong linear relationship indicates unified spindling across multiple contacts of the array. Based on the magnitude of phase lag between co-occurring spindles as a function of distance, we estimated the spindle propagation velocity using the slope of the equation of the linear least squares regression, y=2.82e-4x+0.28, and the mean spindle frequency of 12.52Hz (see Methods). This calculation yielded a spindle propagation velocity of 0.28m/s. Of note, the phase lag between spindles recorded by different contacts is not consistent with the recording of a common generator that volume conducts between contacts because volume conduction is effectively instantaneous.

Co-firing is correlated with spindle coherence

Spindle co-occurrence density (the rate of spindle co-occurrence between two contacts) was greatest at the smallest inter-contact distance of 400μm and decreased sharply until ~1000μm, and then plateaued up to the maximum inter-contact distance of ~4000μm (Fig. 1.4C; R^2=0.98, two term exponential least squares regression). The spindle co-occurrence density was greater than chance at all distances (Bonferroni-corrected α=0.001 for 35 distance bins, mean p=2e-32, range=8e-120 - 7e-31, paired two-sided t-test, mean t=22.43, range=16.13-30.28, mean Cohen's d=1.46, range=1.19-1.91), when the chance spindle co-occurrence density was computed by randomly shuffling the inter-spindle intervals 100 times for each channel of each channel pair and then finding the mean co-occurrence density. We next tested if coherence within the 10-16Hz band between contacts during co-occurring spindles was associated with co-firing recorded by those contacts. Coherence was used to evaluate the relationship between spindles because it depends on both the phases and co-amplitude of signals, which are relevant to

the underlying neuronal activity. The magnitude squared coherence of focal LFP within the 10-16Hz band during spindles was greater at all distances compared to randomly selected NREM epochs matched in number and duration (Fig. 1.4D; Bonferroni-corrected α=0.001 for 47 distance bins, mean p≈0. range≈0, two sample two-sided t-test, mean t=98.79, range=28.30-190.02, mean Cohen's d=0.51, range=0.35-0.71). High levels of co-firing between units recorded by different contacts were restricted to high levels of spindle coherence (>~0.90) between those contacts during co-occurring spindles (Fig. 1.4E-L). This co-firing was concentrated at short delays (<~10ms), and was observed for all unit pair types. The mean PY_1-PY_2 <10ms co-firing rate was significantly higher for high (>0.90) vs. lower (<0.50) spindle coherence (Fig. 1.4F; p=3e-4, Bonferroni-corrected α=0.017 for 3 combinations of delay/coherence, two sample two-sided t-test, t=3.67, Cohen's d=0.21). The mean PY_1-PY_2 co-firing rate was also significantly higher during spindles with high coherence and short (<10ms) vs. longer (51-100ms) co-firing delays (p=4e-39, Bonferroni-corrected α=0.017 for 3 comparisons of delay/coherence, two sample two-sided t-test, t=13.19, Cohen's d=0.51). The mean PY_1-PY_2 co-firing rate increased by ~385% compared to baseline NREM periods between spindles with longer delays and lower coherence (p=9e-17, Bonferroni-corrected α=0.017 for 3 combinations of delay/coherence, two sample two-sided t-test, t=8.48, Cohen's d=0.89). See Supplementary Table 1.4 for additional details. Thus, short latency unit co-firing depends critically on spindle coherence being close to 1.

Spindles travel across the microarray in multiple patterns

Spindle propagation could facilitate sequential neuronal co-firing events leading to patterned synaptic strengthening within a network. Different waves within an individual spindle were capable of exhibiting different patterns of propagation (Fig. 1.5). For example, one spindle wave had a circular propagation pattern, based on its z-score normalized amplitude (Fig. 1.5A,E) and phase (Fig. 1.5B,F), and in subsequent wave cycles showed a planar propagation pattern (Fig. 1.5C-F). We used the MATLAB: *NeuroPatt Toolbox* (Townsend et al., 2018) (see Methods) to find spatiotemporal modes, represented as phase velocity vector fields, that explained the greatest percent variance of the phase velocity vector time

series for each spindle (Fig. 1.6). Controls were generated by randomly shuffling the positions of the good channels once for each spindle prior to interpolation and spatiotemporal analysis. The percent explained variances of modes 1 and 2, i.e., those with the greatest percent explained variance, were greater for spindles (mean and SEM for mode 1 was 22.42±0.15% and for mode 2 was 14.67±0.06%) vs. controls (mode 1 was 11.99±0.04% and mode 2 was 10.20±0.03%) in all subjects (Fig. 1.6A-B, mode 1: $p \approx 0$, $t=47.86$, Cohen's $d=0.93$, and mode 2 $p \approx 0$, $t=36.16$, Cohen's $d=0.73$, paired two-sided t-test), providing confirmation of propagating spindles. There were a variety of propagation patterns within and across patients and spindles (representative examples of mode 1 in Fig. 1.6C), demonstrating that spindles have multiple patterns of propagation within 3.6 x 3.6mm of cortex.

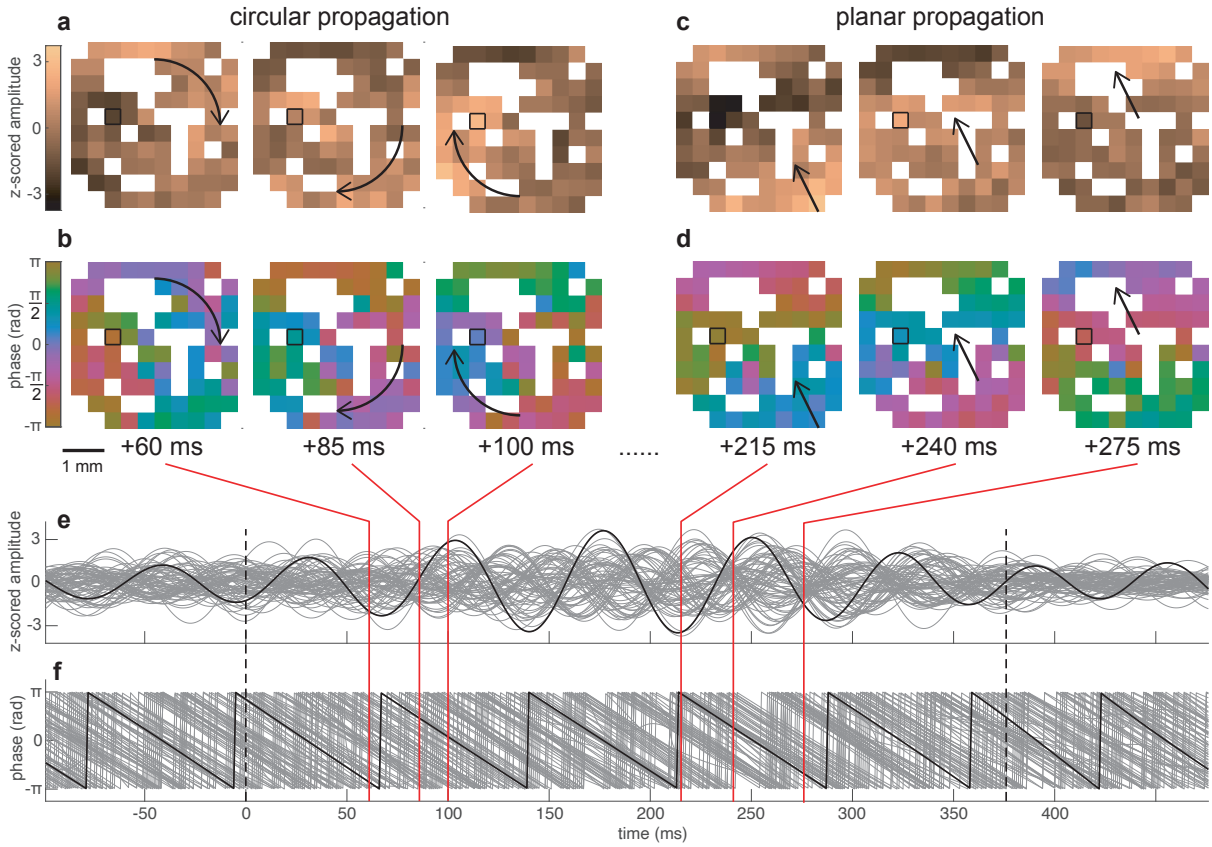

Fig. 1.5. Spindles propagate on a sub-centimeter scale. (**A-B**) Circular propagation of a spindle wave depicted in 3 frames of the instantaneous z-score normalized amplitude (**A**) and instantaneous phase (**B**). A cyclic colormap was used to show phase. (**C-D**) Same as (A-B) but for linear propagation for a different wave within the same spindle. White spaces indicate non-existent or bad channels. The channel outlined in black corresponds to the channel on which the spindle was detected. Arrows indicate approximate trajectory of propagation. (**E-F**) Traces of z-score normalized amplitude (**E**) and phase (**F**) of the same spindle in (A-D). Black trace corresponds to the channel on which the spindle was detected and gray traces show the rest of the channels. Red lines extending from (E) and (F) show the times of the frames in (A-D).

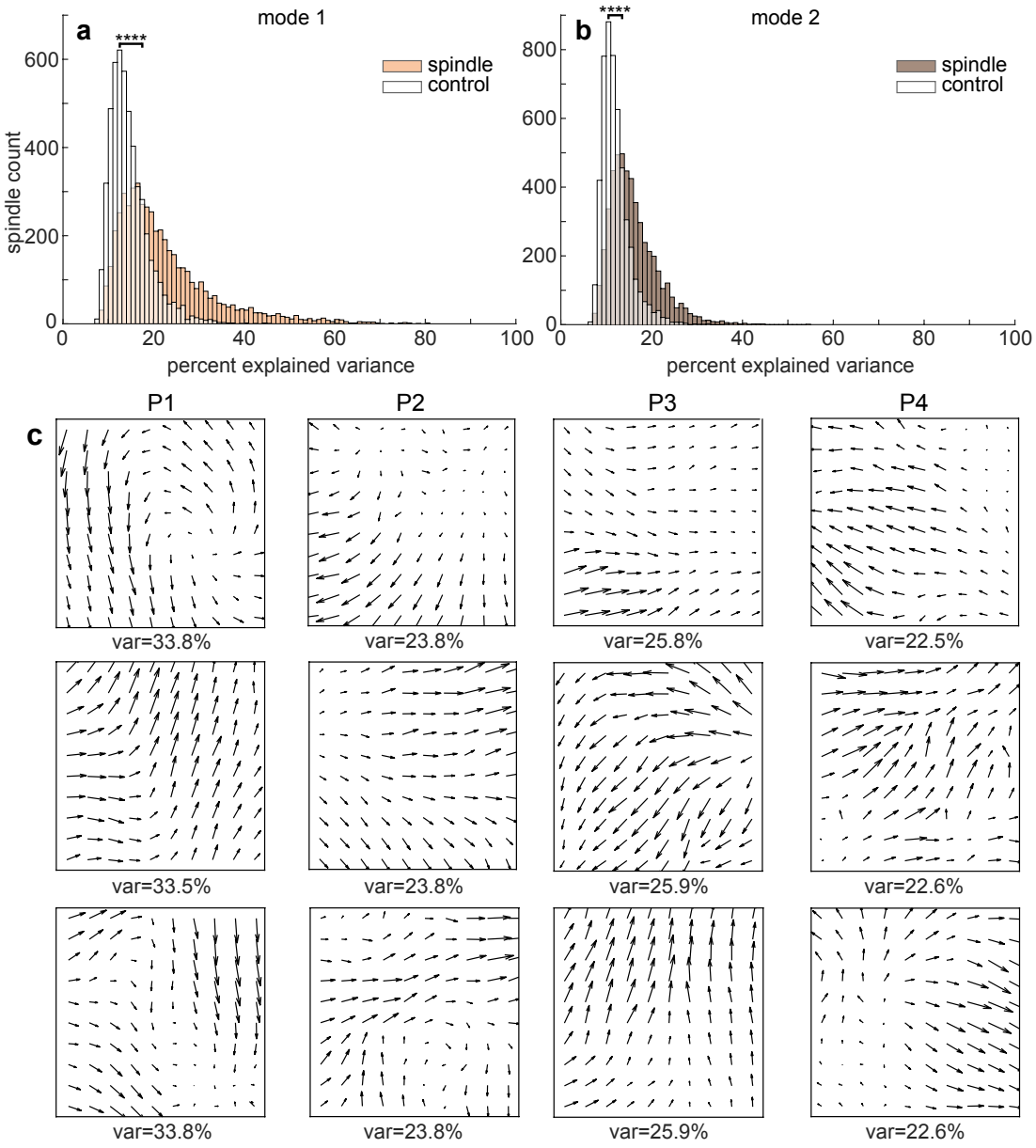

Fig. 1.6. Spatiotemporal propagation patterns of spindles. (**A**) Percent explained variance (var) for most dominant spatiotemporal mode (mode 1) across spindles (tan) and controls where good channel positions were randomly shuffled once per spindle prior to interpolation (white) ($p \approx 0$). ****$p<0.0001$, paired two-sided t-test. (**B**) Same as (A) except for mode 2 ($p \approx 0$). (C) Three representative examples of mode 1 phase velocity vector fields showing individual spindle propagation patterns for each patient (P1-4).

Distinct co-firing and spindle propagation patterns are linked

The above spindle propagation analysis was performed for each spindle independently, and so the patterns could also change across spindles. In order to analyze the relationship to co-firing it was

necessary to identify consistent propagation patterns. Thus, a second analysis was performed on a concatenation of all spindles from each patient. Again, distinct modes were consistently found as in Fig. 1.6C. PY_1-PY_2 co-firing was then quantified separately for modes 1 and 2 of the concatenated spindles for each patient when SVD component scores exceeded the 75th percentile, representing periods when each mode was most prominent. Among 187 pairs where PY_2 co-fired within 25ms following PY_1 at least 10 times between modes 1 and 2, 177 pairs (94.65%) had a significant difference in co-firing for modes 1 vs. 2 (α=0.05, two-sided χ^2 test of proportions). Thus, different patterns of plasticity may be induced by different patterns of spindle propagation.

Discussion:

We identified the spatiotemporally-patterned inter-relations of LFPs and neuronal firing during human sleep spindles over a 10x10 microelectrode array with 400μm pitch. Firing of individual putative cortical PYs and INs increased during spindles, with an additional increase at certain spindle phases. Co-firing within 25ms between neurons recorded on different microcontacts, a pre-requisite for STDP, also increased during spindles in a phase-locked manner. Co-firing of cells and co-occurrence of spindles were greatest at inter-contact separations <1mm but extended over the entire array. Both firing and co-firing were greatest when spindles occurred on down-to-upstates, which is consistent with the proposition that spindles that occur on this transition are especially important for memory consolidation (Maingret et al., 2016). The mean co-firing delay between cells and phase lag between coherent spindles increased linearly with distance. Conduction speed and PY-IN phase relations were consistent with direct cortico-cortical spindle propagation. Short-latency co-firing was concentrated between contact pairs with highly coherent spindles. Multiple two-dimensional spindle propagation patterns and associated distinct co-firing patterns occurred across each array, intermixed within and between spindles. Overall, these microphysiological mechanisms may support and organize memory consolidation by creating the necessary conditions for STDP and activating spatiotemporal networks through travelling spindles.

We found that part of the increase in co-firing during spindles is due to the two-fold increase in firing they induce. This finding was in contrast to (Andrillon et al., 2011) who found no increase in firing during spindles in humans. This difference could be because they sampled medial limbic cortex whereas we sampled lateral temporal cortex. Furthermore, they correlated unit spiking detected by microwires with LFP recorded by a macroelectrode contact ~4mm away, whereas we correlated unit spiking with LFP recorded from the same contacts, and they recorded from all cortical layers whereas we only recorded from supragranular and possibly granular layers. Indeed, the increase in unit firing during spindles was ~50% smaller at a distance of ~4mm, and it has been previously shown that spindle-phase modulation of high gamma in humans and of unit firing in rodents is greater in supragranular vs. infragranular layers (Hagler et al., 2018; Peyrache et al., 2011). Thus, our recordings focused on the most responsive layers. We furthermore found that PY and IN spiking was locked to the phase of individual spindle waves, which is consistent with what has been previously shown for PY and IN in rodents (Peyrache et al., 2011) and for units without cell type classification in humans (Andrillon et al., 2011), and suggests one mechanism whereby spindles specifically coordinate co-firing beyond a mere general tonic increase in firing.

Our study provides the first direct evidence that the essential pre-condition for STDP, unit pair co-firing within 25ms, is met in the human cortex during spindles in NREM sleep. This finding helps resolve a major issue in understanding how STDP could occur under normal conditions: the large number of repetitions, up to hundreds, that are needed to produce long-term changes (Wittenberg et al., 2006). Co-firing during spindles could address this requirement because in a normal night's sleep, ~1000 spindles will occur at most cortical sites, and each spindle has ~10 cycles, so there are ample opportunities for STDP repetitions. Furthermore, spindle frequency lies within the repetition rate for which such pairings are effective (Feldman, 2012). In addition, memory-related cortical input from the hippocampus associated with ripples may be available on multiple spindle peaks often seen in the posterior hippocampus, phase-locked with cortical spindles (Jiang et al., 2019b; Staresina et al., 2015). Of note, all of the recordings in this study were from the anterolateral temporal cortex, which is not part of

the medial prefrontal cortex-hippocampal network that is typically associated with sleep-dependent memory consolidation in rodents. However, rodents have no clear homologue to the anterolateral temporal cortex, which in humans is thought to be a key part of the memory system (Vaz et al., 2019; Vaz et al., 2020).

In canonical PY_1-PY_2 STDP, pre-before-postsynaptic spiking leads to LTP and the reverse leads to LTD (Feldman, 2012). Plasticity underlying memory consolidation may involve both (Clopath, 2012). Increased co-firing within 25ms for all combinations of PY and IN was found during co-occurring spindles over 4mm, suggesting an extensive network of co-firing cells. Based on neuronal density in the human cortex, and the co-firing probability-distance function we observed, it can be roughly estimated that the number of PY that co-fire more during spindles with a given PY within a radius of 4mm, beyond what would be expected from a simple increase in firing rate, is ~37,500 for layer III alone. Many of the pairs with increased co-firing had a preferred order of spiking, which could support unidirectional plasticity. However, we did not explicitly test whether the units modulated during spindles underwent synaptic weight changes or were involved in plasticity underlying memory consolidation, which should be assessed in future work. Human slice recordings have shown that local excitatory connectivity between layers II/III PYs is 13-18% (Peng et al., 2019), substantially higher than in mice (Seeman et al., 2018). However, most co-firing within 25ms is probably by unit pairs that are not directly connected but belong to the same local network. In some cases this is directional, however there could be multiple pathways between co-firing units, some in one direction and others in the opposite direction, and network tuning would involve strengthening some routes and weakening others. In any case, the network of co-firing cells appears to be extensive.

Human magnetoencephalography (Dehghani et al., 2011) and intracranial macroelectrode (Andrillon et al., 2011; Piantoni et al., 2017) recordings have shown that spindles, once thought to be a global phenomenon, are often focal at a centimeter scale. Human laminar recordings have furthermore shown that spindles localize to specific cortical layers (Hagler et al., 2018; Halgren et al., 2018), however the lateral extent of spindles in human cortex has not been reported on a sub-centimeter scale. We show

that spindle co-occurrence and coherence in human cortex peaks at the shortest inter-contact distance of 400μm, decreasing sharply to a plateau at ~1000μm. Since an average reference would eliminate spindles that are equal across all leads, there may also be co-occurrence at a larger scale, and indeed, asymptotic co-occurrence and coherence exceeded chance. Taken together, the data indicate that the cortical extent engaged by spindles can range from a few columns to much of the cortex.

Traveling waves may gate the flow of spiking in cortical circuits (Davis et al., 2020). We found that spindles propagated within the microgrid at ~0.28m/s. This is within the range of or slightly lower than previously reported intracortical axon conduction velocities, including for layers II/III, of 0.28m/s and 0.15-0.44m/s in rat visual cortex (Lohmann et al., 1994; Murakoshi et al., 1993), 0.35-0.45m/s in rat neocortex (Telfeian et al., 2003), and 0.35m/s in cat visual cortex (Hirsch et al., 1991). The true axonal conduction velocity of spindles may be faster than 0.28m/s because our calculation assumes a direct path of travel and does not take synaptic delays into account. This velocity is much slower than what was reported by Muller et al. (2016) for human cortical spindles (3-9m/s) and Halgren et al. (2019) for human cortical alpha (0.91m/s), both using ECoG recordings, presumably because they were measuring fast conduction via myelinated fibers passing through the white matter, whereas we were measuring slow conduction via unmyelinated fibers within the cortical gray matter. The different velocities may promote plasticity in networks of different spatial extents (Muller et al., 2018; Muller et al., 2016).

Direct cortico-cortical propagation of spindles is at odds with the common conception of cortical spindles being driven from the thalamus. In cats, the thalamus continues to spindle after cortical removal, but the cortex does not spindle after disconnection from the thalamus (Contreras et al., 1997). In mice, rhythmic optogenetic activation of the thalamic reticular nucleus triggers spindles (Halassa et al., 2011). In humans, thalamic spindles occur more frequently and begin before cortical, and in rare cases show tight phase-locking with thalamus leading the cortex (Mak-McCully et al., 2017). Thus, spindles are thought to originate thalamically and project cortically (De Gennaro et al., 2003). Thalamocortical projections in mice to both primary sensory and limbic cortices drive INs more strongly and at shorter latencies than PYs (Cruikshank et al., 2007; Delevich et al., 2015). Thus, our finding that PY spiking

precedes IN spiking is not consistent with cortical spindles in humans being mainly driven by the thalamus. Rather, it is possible that while cortical spindles in humans are initially driven by the thalamus, intrinsic cortical circuits may subsequently amplify and spread the spindle. Local generation seems plausible because the thalamic mechanism underlying spindle generation involves reciprocal connections between excitatory and inhibitory cells, and activations of h and T currents (Destexhe et al., 2003; McCormick et al., 2015), all of which are present in human supragranular cortex (Kalmbach et al., 2018). Furthermore, the consistently higher spindle frequency in the human thalamus compared to cortex is hard to explain if cortical spindles are all directly driven by the thalamus (Mak-McCully et al., 2017). This thalamocortical frequency difference increases over the course of a spindle, as the spindle spreads across the cortex, and is correlated with the amount of such spread (Gonzalez et al., unpublished). Direct cortico-cortical spindle propagation may be necessary in humans, who have ~1400 cortical neurons for every thalamocortical cell (calculations based on previously reported cell counts (Azevedo et al., 2009; Xuereb et al., 1991)).

In summary, we show here that human cortical neurons have a strong increase in firing during spindles, both tonically and at particular spindle phases. This contributes to enhanced co-firing within 25ms, a pre-condition for STDP, by neurons separated by ~0.4-4mm. Spindles are focally organized within this microdomain and co-firing is greatest at short distances when spindle coherence is high. Multiple patterns of wave propagation occur both within and between spindles, and are associated with distinct co-firing sequences. Therefore, spindles are associated with highly organized and dynamic spatiotemporal patterns of neuronal co-firing that may facilitate plasticity within local cortical networks.

Methods:

Participants and data collection

Four adult patients (Table 1.1) with focal, pharmaco-resistant epilepsy underwent 4-21 days of continuous electrocorticography and invasive EEG recordings for the localization of seizure foci prior to resection. The decision to implant and the duration of implantation were based entirely on clinical

grounds. While undergoing clinical recording these patients also underwent intracranial microelectrode recordings with the Utah Array (Fig. 1.1A; Utah Array – © 2020 Blackrock Microsystems, LLC). The Utah Arrays were implanted after thorough review by the duly constituted Institutional Review Board (IRB) of Partners HealthCare, the parent institution of Massachusetts General Hospital and Brigham and Women's Hospital, which are academically part of Harvard Medical School. The IRB follows procedures defined by the US Department of Health and Human Services and is certified by that institution. In all cases the Utah Array was implanted in a location that was strongly suspected based on pre-implant clinical information to be included within the boundary of the therapeutic resection, and in all cases it was later resected in order to gain surgical access to the focus which lay in deeper structures (Fig. 1.1B). The resected tissue in which the Utah Array was implanted was determined not to be an epileptogenic zone in any of these patients. No seizures originated from the area implanted with the Utah Array in any of the patients included in the study and no seizures occurred during the epochs analyzed. The arrays were implanted for research purposes and did not affect clinical monitoring. All ethical regulations for work with human participants were followed, and fully informed written consent for research was obtained prior to implantation of the Utah Arrays from all patients included in this study according to the Declaration of Helsinki guidelines as monitored by the local IRB at Partners HealthCare.

Electrodes and localization

The Utah Array is a 10x10 microelectrode grid, with corners omitted, that has 400μm contact pitch (Fig. 1.1A). Each silicon probe is 1 or 1.5mm long (summarized in Table 1.1) and 35-75μm wide at its base, tapering to 3-5μm at the tip, and is insulated except for the tip, which is platinum-coated. Each patient in the study had one array implanted into the superior or middle temporal gyrus, in a region that was outside of the epileptogenic focus but which had to be removed in order to gain surgical access to the focus. Probes were placed under direct visualization perpendicular to the cortical surface. Based on a previous histological examination of human brain tissue, temporal cortex layer II begins at a mean of 252μm and layer III ends at a mean of 1201μm (Mohan et al., 2015). Therefore, we expect that the 1.0-

1.5mm long probes of the Utah array were implanted in supragranular layers II/III and possibly as low as upper granular layer IV.

Recording and preprocessing

Data were acquired at 30kHz sampling (Blackrock Microsystems), from 0.3 to 7.5kHz. Data were subsequently low-passed at 500Hz and down-sampled to 1kHz for the LFPs. Data were saved for offline analysis in MATLAB 2019b (MathWorks). LFPs were visualized in MATLAB: *FieldTrip* (Oostenveld et al., 2011). Channels were excluded when there were large amounts of noise or no units detected. Out of the 96 recording channels the mean number excluded from analysis was 29.75 (range 13-47). The 1kHz data was average-referenced to negate the effects of the distant subdural reference, which could have detected neural activity distant from the array.

Sleep staging and data selection

After the data were collected, NREM sleep periods were determined during overnight periods by a neurologist trained in sleep staging according to the standard guidelines (Silber et al., 2007) as N2 (corresponding to S2 in the prior terminology) and N3 (combining S3 and S4 from the prior terminology), based on visual examination of 30s epochs of electrocorticography data and concurrent video recording of the patient. All data analyzed were from overnight sleep. The night and sleep periods to be analyzed were chosen based on quality of sleep, quality of recordings, absence of ictal events, and time since prior ictal event. We required that there be at least 60 minutes of overnight N2/3 epochs that did not include seizures or large amounts of epileptic spiking as determined visually. Periods marked as N2 and N3, based on the presence of slow waves, K-complexes, and spindles, were selected for analysis. These periods were validated as N2 and N3 based on increases in delta (0.1-4Hz) and sigma (10-16Hz) band powers. Data from patients were only analyzed if the Utah Array was implanted in tissue that was determined clinically as not epileptogenic. Based on these criteria, four patients were selected for inclusion in this study out of

ten implanted with Utah Arrays. One limitation to our study is that due to the clinical context (e.g., patients being awoken to measure vital signs), the sleep architecture of the patients could be disrupted.

Spike detection and sorting

The 30kHz data recorded from each electrode contact was bandpassed at 300-3000Hz with an 8th order elliptic filter with a pass-band ripple of 0.1dB and a stop-band attenuation of 40dB. Putative unit spikes were detected when the filtered signal exceeded 5 times the estimated standard deviation of the background noise (Donoho et al., 1994), computed as:

$$\text{spike threshold} = 5 \times \frac{\text{median}(|x|)}{0.6745} \quad (1)$$

Where x is the 300-3000Hz bandpassed data. The first three principal components of each spike were computed and unit clusters were manually selected. The remaining data points underwent clustering by k-means and a Kalman filter mixture model (Calabrese et al., 2011). Visual inspection of the clusters identified by these two algorithms was used to determine which achieved better separation. Spikes were examined visually and those with abnormal waveform shapes or amplitudes far exceeding the majority of the spikes from their putative unit, such as those that may have been due to epileptiform activity, were excluded from analysis.

Single unit classification

PYs fire at low rates (~0.1Hz in humans), with frequent bursting, and have short refractory periods and sharp spike autocorrelations, whereas INs typically fire at high rates (>1Hz), with infrequent bursting, and have long refractory periods and broad spike autocorrelations. We classified units based on established methods in rodents (Barthó et al., 2004; McCormick et al., 1985) that have been adapted for use in humans (Peyrache et al., 2012), with additional considerations for MUs, which had spikes that were larger than the background noise and thus exceeded the detection threshold but could not be clustered into separable units. For each unit we computed the firing rate, valley-to-peak time interval, half peak width

time interval, and bursting index (summarized in Table 1.1; Fig. 1.1C shows distinct clusters of PY and IN based on firing rate, valley-to-peak interval, and half width interval). As bursting results in a bimodal distribution of inter-spike intervals (ISIs), the bursting index was determined by running the Hartigan dip test for unimodality on the logarithm of distribution of ISIs (Hartigan et al., 1985). Units were classified as putative PYs if they had spike rates of ~0.1-0.8Hz, long valley-to-peak and half width intervals (Fig. 1.1D), sharp autocorrelations (Fig. 1.1E), and a bimodal ISI distribution (Fig. 1.1F) reflecting a propensity for bursting. By contrast, units were classified as putative INs if they had spike rates of ~1-5Hz, short valley-to-peak and half width intervals, broad autocorrelations, and a predominantly unimodal ISI distribution (Fig. 1.1D-F). All single units were required to have a refractory period ≥1ms. Units that had lower amplitude spikes and higher firing rates were classified as MUs (Supplementary Fig. 1.4A-B). While this overall classification method is indirect and INs in particular have heterogeneous spiking properties (Tremblay et al., 2016), previous studies using human extracellular recordings have supported the classification of putative PYs and INs using similar metrics (Le Van Quyen et al., 2008; Truccolo et al., 2011).

Single unit quality and isolation

In order to confirm that the PY and IN that we detected and classified were distinct single units, we evaluated the quality of the units according to criteria used by Kamiński et al. (2020). The mean and standard deviation peak signal-to-noise ratio for PY was 8.82±3.42 and for IN was 5.18±2.85 (Supplementary Fig. 1.1A-B), indicating that the unit spikes well-exceeded the noise floor. Since the refractory period is ~3ms, the percentage of ISIs <3ms suggests the amount of single unit contamination by spikes from other units. The mean and standard deviation of the percent of ISIs <3ms for PY was 0.28±0.49% and for IN was 0.33±0.58% (Supplementary Fig. 1.1C-D), which indicate very little single unit contamination by spikes from other units. Since multiple single units were detected on certain contacts, we evaluated the degree to which their single unit clusters were separable using the projection test (Pouzat et al., 2002), which measures the pairwise projection distance in units of standard deviations.

The mean and standard deviation projection distance of PY pairs on the same contact was 94.01±85.64 standard deviations and of IN pairs was 82.51±83.24 standard deviations, indicating that when there were multiple units detected on the same contact they were highly separable (Supplementary Fig. 1.1E-F). To verify the temporal stability of units across the recordings, we divided each patient's recording period into quartiles and confirmed through visual inspection that the mean waveform shape and amplitude of each unit was consistent across quartiles.

Sleep spindle detection and analysis

Spindle detection was performed using a previously established method (Hagler et al., 2018) that is primarily based on the standard criterion of sustained power in the spindle band (Fig. 1.1G). Each channel was bandpassed at 10-16Hz using an 8th order zero-phase frequency domain filter with transition bands equal to 30% of the cutoff frequencies. Absolute values of the bandpassed data were smoothed via convolution with a tapered 300ms Tukey window and median values of 10-16Hz band amplitudes were then subtracted from each channel to account for differences between channels. The data were then normalized by the median absolute deviation. Spindles were detected when the peaks in the normalized data exceeded 1 for at least 300ms, and onsets and offsets were marked when these amplitudes fell below 1 (see Supplementary Fig. 1.2A for durations). Putative spindles that coincided with large increases in lower (4-8Hz) or higher (18-25Hz) band power were rejected prior to analysis to exclude interictal epileptiform activity and broad spectrum artifacts, as well as 5-8Hz theta bursts, which may extend into the lower end of the spindle range (Gonzalez et al., 2018). All data analyzed were visually inspected in an LFP viewer to ensure that there were no seizures or large artifacts (MATLAB: *FieldTrip* (Oostenveld et al., 2011)). Subsets of spindles from each channel of each patient were also inspected visually to confirm that these events contained multiple prominent 10-16Hz cycles and were not contaminated with interictal epileptiform discharges or artifacts. Spindle frequency was calculated by dividing the number of zero crossings in the spindle band by two times the spindle duration (frequency distribution shown in Supplementary Fig. 1.2B). Coherence between co-occurring spindles was computed by finding the

magnitude squared covariance of the 10-16Hz bandpassed spindle-spindle co-occurring epoch. Spindle propagation velocity was calculated as:

$$v = \frac{2\pi f d}{\varphi} \quad (2)$$

Where f is the spindle frequency, d is the distance between the contacts recording the two waves, and φ is the phase offset between the waves.

Interictal spike rejection

To reject events or baseline periods contaminated with interictal epileptiform discharges, we detected interictal spikes (IIS) when the z-score of the analytic amplitude of the 20Hz highpass and the 200Hz highpass of the signal exceeded 7. We excluded baseline periods, spindles, downstates, and upstates from analysis when they fell within ±100ms of IIS. Since interictal epileptiform discharges may impact spindle generation (Gelinas et al., 2016), we confirmed that the spindles kept for analysis were not coupled to IIS (Supplementary Fig. 1.2C)

Downstate and upstate detection and analysis

To evaluate unit spiking during spindles that occurred in association with downstates or upstates, we detected downstates and upstates using a previously established method (Gonzalez et al., 2018; Mak-McCully et al., 2017). Data from each channel were bandpassed at 0.1-4Hz and consecutive zero crossings within 0.25-3s were detected. The top and bottom 20% of amplitude peaks between zero crossings were then selected. The average high gamma (70-190Hz) analytic amplitude was found within ±100ms of each peak. Since the polarity of downstates vs. upstates for each channel was not known, we determined whether the average peak-locked high gamma envelope was higher for positive vs. negative peaks for each channel and assigned the polarity of upstates (more high gamma) vs. downstates (less high gamma) accordingly. We then selected individual downstates and upstates for analysis only if the mean ±100ms peak-locked high gamma envelope was for downstates less than the mean and for upstates

greater than the mean of a -4000 to -2000ms baseline period relative to the peaks. Therefore, this method confirms the channel polarity for downstates vs. upstates, and ensures that each event is associated with the expected change in high gamma. Spindles that coincided with downstates were identified as those where the downstate peak preceded the spindle onset within 750ms, and spindles that coincided with upstates were identified as those where the upstate peak followed the spindle onset within 500ms (Supplementary Fig. 1.8). Isolated spindles, i.e., those that did not coincide with downstates or upstates, were identified as those that did not have a top 20% positive or negative amplitude peak, detected as described above, within ±1000ms.

Unit spike rate and phase analysis

The percent of baseline spike rate during spindles for each unit detected on the same channel as the spindle was computed by multiplying 100 times the spike rate during all concatenated spindles on the unit's channel divided by the spike rate of all of the concatenated randomly selected non-spindle epochs that were matched in number and duration to the spindles and did not contain periods within ±100ms of IIS. Spindle phases of unit spikes were determined by computing the Hilbert transform of the 10-16Hz bandpassed signal and then finding the angle of the analytic signal at the times of the spikes. The circular mean spindle phase angle was computed for each unit using MATLAB: CircStat (Berens, 2009).

Unit pair co-firing analysis

Prior to analysis, co-occurring spindle periods were identified when there were co-occurring spindles on two channels. The first onset and last offset of the two spindles was used as the co-occurring spindle epoch. Non-spindle epochs were selected as the NREM periods when there was no spindle, with 100ms padded before the onset and after the offset of every spindle, detected on either channel of a given unit pair. Unit pair co-firing of PY_1-PY_2, IN_1-IN_2, PY_1-IN_2, and IN_1-PY_2 during co-occurring spindles was compared to: (1) co-firing during non-spindle epochs, where 1000 sets of randomly selected epochs in between spindles (during baseline) that were matched in number and duration to the spindles, and (2) co-

firing during "shuff-spindles" where spike times of each unit of the pair during the co-occurring spindles were randomly shuffled 1000 times. Unit pair co-firing was quantified by counting the number of spikes from one unit (e.g., PY_1) during the 25ms preceding each spike from the second unit (e.g., PY_2). Pairs with units detected on the same channel were not included in the analysis. Unit pairs with significantly increased co-firing within 25ms were tested for co-firing order preference. For each pair, the number of spikes during the 25ms window before vs. after the spikes of the other unit were compared. Co-firing latency was compared to spindle phase lag by identifying unit pair co-firing within 25ms during co-located spindles. The angular difference of spindle phases was used to compute the spindle phase lag for each co-firing event.

Estimation of population of co-firing cells

To estimate how many PY had greater co-firing during spindles with a given PY within a 4mm radius for cells from layer III, beyond what would be expected from a simple increase in firing rate, we used cell counts from (DeFelipe et al., 2002), who showed that within a 50x50µm column of anterior temporal cortex in humans there are ~35 cells in layer III. We multiplied by this by 0.8 to determine the approximate number of PY, 28, resulting in 11200 PY within a square millimeter column of layer III. We then used the following equation to estimate the number of PY that had greater co-firing with a given PY:

$$D\int_0^4 PAdr \tag{3}$$

Where D is the estimated density of PY per square millimeter, $A=\pi r^2$, with radius r, and P is the probability of significant co-firing at a given r:

$$P = \mathrm{P}_{\mathrm{r=4}} + \frac{(4-r)(\mathrm{P}_{\mathrm{r=0}} - \mathrm{P}_{\mathrm{r=4}})}{4} \tag{4}$$

Where $P_{r=0}$ and $P_{r=4}$ were approximated as 0.08 and 0.04, respectively, and P decreasing linearly with r, based on our results in Fig. 1.4A. Note that this estimate is conservative in that it only considers cells in layer III. (DeFelipe et al., 2002) estimated ~158 in all layers within the 50x50µm column so the estimate

would be scaled by 158/35 to account for all layers. Also, this estimate is conservative because it only considers PY, and it assumes that the co-firing continues to increase linearly from r=0.4 to r=0, whereas it may be supralinear in that region. Finally, this estimate is conservative because it only counts neurons with co-firing beyond that expected from the spindle-related firing rate increase, while P is >2.5X greater when including all co-firing relative to baseline.

Spike time tiling coefficient

The correlation of co-firing within ±25ms between units was computed using the spike time tiling coefficient (STTC), which unlike the correlation index, is independent of firing rates (Cutts et al., 2014). For a given unit pair, for example PY_1-PY_2, the STTC was computed as:

$$\mathrm{STTC} = \frac{1}{2}\left(\frac{P_{\mathrm{PY}_1} - T_{\mathrm{PY}_2}}{1 - P_{\mathrm{PY}_1}\mathrm{T}_{\mathrm{PY}_2}} + \frac{P_{\mathrm{PY}_2} - T_{\mathrm{PY}_1}}{1 - P_{\mathrm{PY}_2}T_{\mathrm{PY}_1}}\right) \quad (5)$$

Where *P* is the proportion of spikes from a given unit in a pair that occur within ±25ms of the spikes from the other unit in the pair, and *T* is the proportion of the total recording time within ±25ms of the spikes from a given unit.

Spatial analysis of spindles and unit spiking

The spatial layout of the recording array resulted in a highly variable number of contacts at different inter-contact distances. In order to approximately equalize the sample size in different distance bins, channel-pairs were grouped progressively at increasing inter-contact distances until a minimum number was attained, and then a new bin was begun. For example, for determining the spatial fall-off of spindle co-occurrence, for each channel pair the number of co-occurring spindles with any overlap was determined, and then binned with at least 100 minimum channel pairs per distance bin. If there were subsequent pairs after 100 that had the same inter-contact distance then the values were included within that same bin. The distance values plotted show the mean inter-contact distance for each bin. The same progressive binning method was used for the analysis of spindle coherences (minimum per bin=100), unit

spike rates as a function of time and spindle coherence (minimum per bin=200-500), spindle phase lags (minimum per bin=1000), unit spike rates (minimum per bin=50), unit co-firing significances (minimum per bin=50), and unit STTCs (minimum per bin=30) as a function of inter-contact distances.

Analysis of spindle propagation

Visualization of sleep spindle propagation was done by z-scoring the 10-16Hz bandpassed data from each channel, which reduces effects of the average reference, as well as finding the phase of the 10-16Hz bandpassed data using the angle of the analytic signal. Prior to characterizing spatiotemporal patterns, epochs during which at least 20% of non-rejected channels were spindling were selected so that spatiotemporal analysis was limited to times when there was active spindling across the grid. Rejected channels were spatially interpolated by performing a 2D biharmonic spline interpolation (MATLAB*: griddata)* of the analytic signal and then extracting the real signal since the following analysis steps require no missing channels. Spindle spatiotemporal patterns of propagation were characterized for each spindle using the *NeuroPatt Toolbox* (Townsend et al., 2018), which uses optical flow estimation and singular value decomposition (SVD) to extract dominant spatiotemporal patterns from phase velocity vector field time series. This method is closely related to principal component analysis (PCA) as it reduces the dimensionality of the data to extract patterns that comprise the most variance. However, this method differs from PCA in that it extracts spatial modes that are vector fields, which represent spatiotemporal propagation patterns. The input data were bandpassed at 10-16Hz and the analysis was performed according to the phase within this band for each channel. The smoothing and non-linearity penalty optical flow parameters were set to $\alpha=0.5$ and $\beta=1$, respectively, and real singular value decomposition was performed on the velocity vector fields for spatiotemporal mode extraction. To analyze a sufficient number of co-firing events in relation to propagation patterns, the same spatiotemporal analysis was performed but with concatenated spindles for each patient.

Statistical analyses

Unit spike rates during spindles vs. baseline (randomly selected non-spindle epochs during NREM that were matched in number and duration to the spindles) were evaluated by testing if the ratio minus one was significantly different than zero by using a one sample two-sided Wilcoxon signed-rank test. To test whether there were differences between spindle conditions (e.g., isolated spindles vs. spindles that coincided with downstates or upstates), the ratios were evaluated using a paired two-sided Wilcoxon signed-rank test. To test if there was a difference between the spindle phase distributions of PY and IN, a parametric Watson-Williams multi-sample test for equal circular means was used. To test for spindle phase preferences of unit spiking, a Hodges-Ajne test was first used to determine if the distribution of the spindle phases of the spikes of each unit was non-uniform. Next, the spikes were randomly shuffled 1000 times and the Hodges-Ajne test was used to determine the 1000 p-values of the spindle phase distributions. Finally, a unit was determined to have a significant phase preference if the p-value of its spindle phase distribution was in the 5th percentile of the 1000 p-values from the shuffled distribution. To compare unit pair co-firing during co-occurring spindles vs. baseline, we randomly selected 1000 sets of non-spindle epochs, during which no spindles in either channel were detected, and which were matched in number and duration to the spindle co-occurrence epochs. The p-value was calculated as the percent of the 1000 sets of randomly shuffled non-spindle epochs that had more spikes from one unit in the 25ms preceding the spikes of the second unit. For example, for a given PY_1-IN_2 the number of PY_1 unit spikes within 25ms preceding all IN_2 spikes was counted. To compare unit pair co-firing during spindles vs. shuff-spindles, where the times of the spikes of each unit during each co-occurring spindle were randomly shuffled 1000 times, the p-value was calculated as described above. To test whether there was greater co-firing for spindles that coincided with downstates or upstates (which were pooled due to the small number of events) vs. isolated spindles, we computed the average co-firing rate across unit pairs based on the spikes of PY_1 (or IN_1) within the 25ms preceding the spikes of PY_2 (or IN_2) using a paired two-sided Wilcoxon signed-rank test. This same test was also used to confirm that there was more co-firing during isolated spindles vs. non-spindles. The significance of ordered co-firing of each unit pair was computed

by comparing the proportion of the spikes from one unit occurring in the 25ms before vs. after the spikes from the other unit using a two-sided χ^2 test of proportions (MATLAB: *prop_test* (Laurie, 2020)) for all pairs with a minimum of 10 co-firing events during the ±25ms windows. To evaluate spindle co-occurrence vs. chance, we compared the spindle co-occurrence density vs. the chance spindle co-occurrence density using a paired two-sided t-test. For each channel pair the chance spindle co-occurrence density was determined by randomly shuffling each channel's inter-spindle intervals 100 times for each channel pair and finding the mean density of chance co-occurrences. Significance was evaluated for $\alpha=0.05$, and when indicated a Bonferroni-corrected α was used to account for multiple comparisons. All fits were approximated with a linear least squares regression, and for fits with $R^2<0.3$, exponential least squares regressions were instead used if they met $R^2>0.3$. If both fits met $R^2>0.3$ then a linear fit was used unless the R^2 of the exponential fit was >10% larger. Fits are only shown for significant linear relationships or well-approximated exponential relationships. To test for the significance of a linear relationship, the significance of the correlation coefficient was used. To visualize the instantaneous phase of a propagating spindle, a cyclic color map was used (Thyng et al., 2016). To generate controls for the analysis of spatiotemporal propagation patterns, we randomly shuffled the positions of the good channels once for each spindle prior to interpolation. The Cohen's d was calculated according to MATLAB: *computeCohen_d* (Bettinardi, 2020).

Data availability

Figure source data are provided with this paper. The authors' data sharing agreement currently does not permit making the raw data publicly available. The raw data that support the findings of this study are available from the corresponding authors upon reasonable request.

Code availability

The code that support the findings of this study are available from the corresponding authors upon reasonable request.

Supplementary Information:

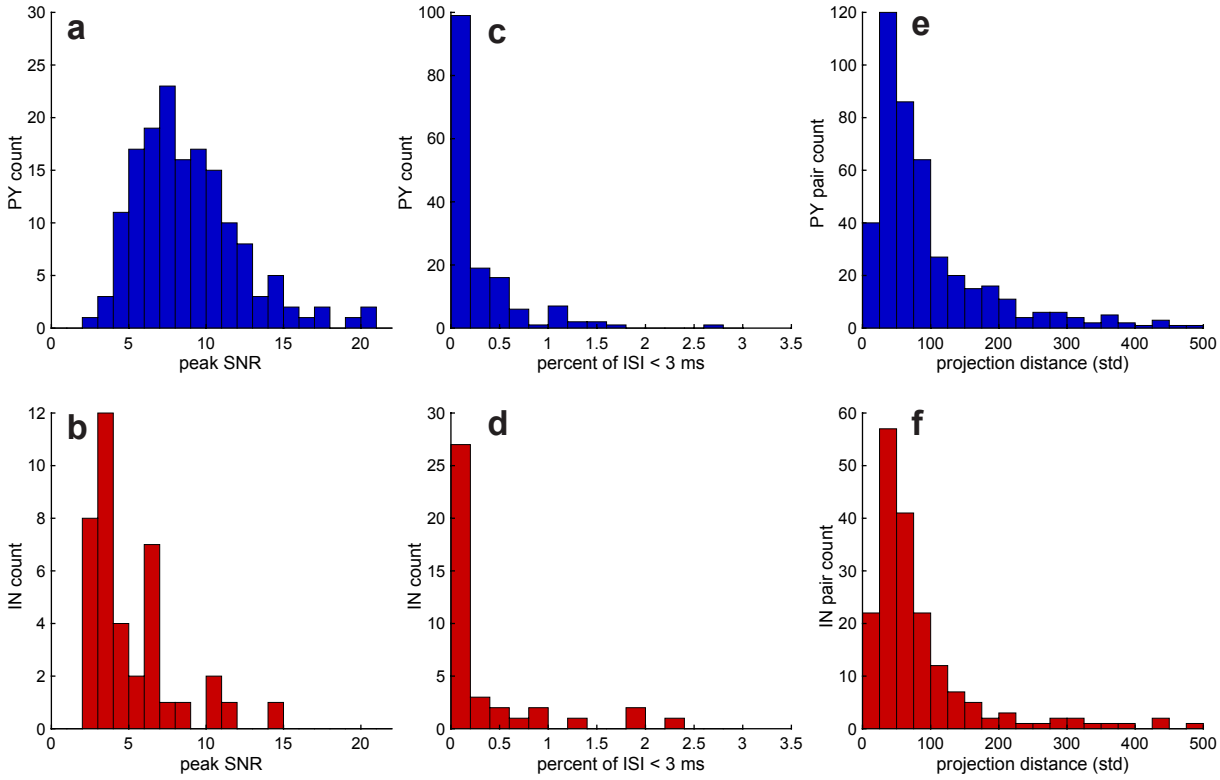

Supplementary Fig. 1.1. Unit quality and isolation metrics. (**A-B**) Histograms of peak signal-to-noise ratio of PY (**A**) and IN (**B**). (**C-D**) Histograms of percent of ISIs shorter than 3 ms for PY (**C**) and IN (**D**). Most cells had no, or very few, ISIs <3 ms. (**E-F**) Histograms of pairwise projection distances between all unit pairs detected on the same contact in units of standard deviation for PY (**E**) and IN (**F**). ISI=inter-spike interval.

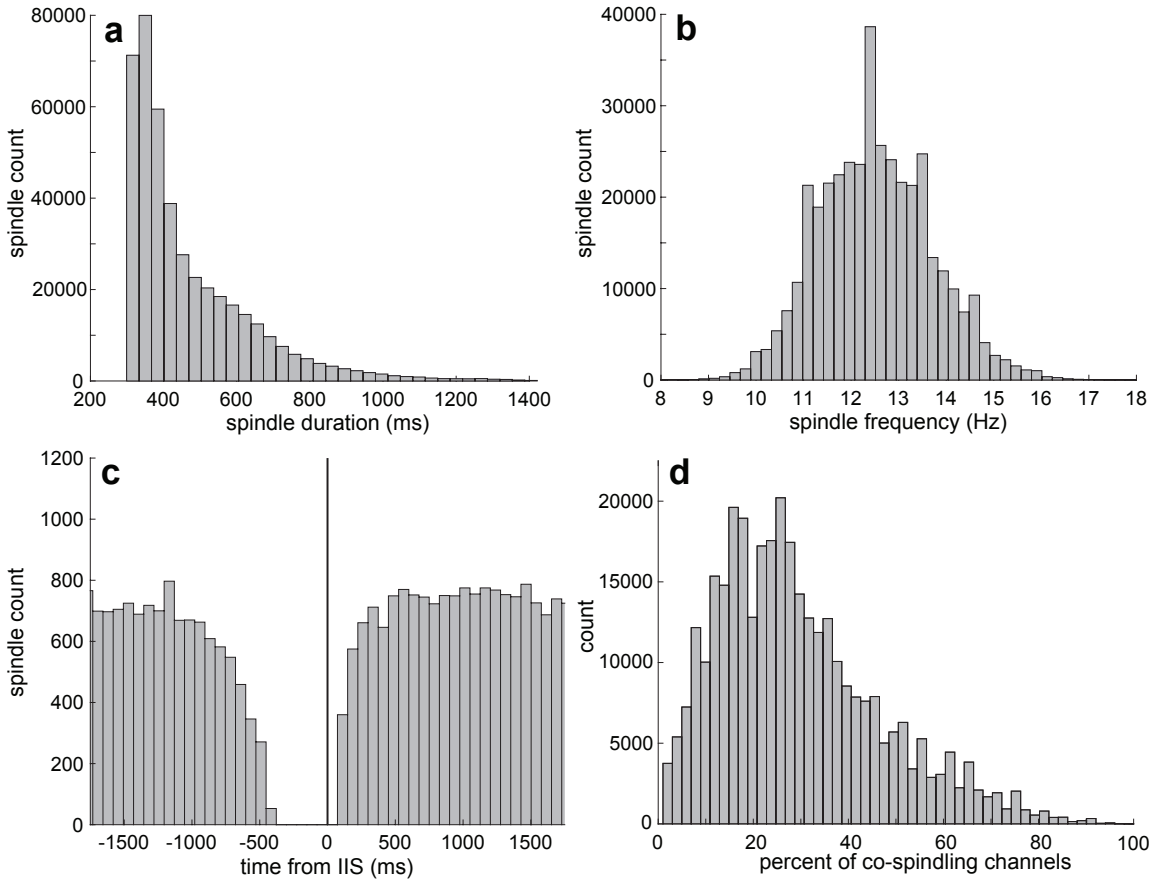

Supplementary Fig. 1.2. Spindle metrics. (**A**) Histogram of spindle durations. (**B**) Histogram of spindle oscillation frequencies. (**C**) Peri-IIS histogram of spindle onsets post-rejection of spindles that occurred within ±100 ms of IIS. (**D**) Percent of co-spindling channels when there was at least one spindle occurring. Note that about 15-40% of the channels were co-spindling in most events. IIS=inter-ictal spike.

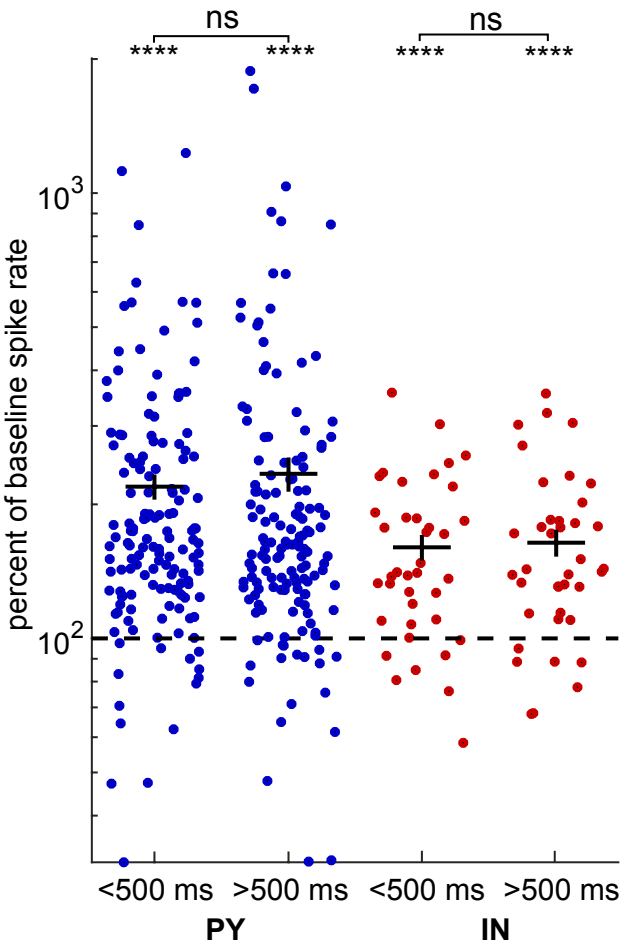

Supplementary Fig. 1.3. Unit spiking during shorter compared to longer spindles. Spike rates of PY (n=156) and IN (n=39) during concatenated spindle epochs as log-percent of baseline spike rate during shorter (<500 ms) spindles and longer (>500 ms) spindles. Baseline spike rate was computed as the spike rate during concatenated NREM epochs between spindles matched in number and duration to the spindles. Color circles show the mean firing rate of each unit. Solid horizontal lines show mean and vertical show SEM. Dashed horizontal line shows baseline spike rate (100%). The mean percent of baseline spike rate for PY during shorter spindles was 219.16±14.22% and longer spindles was 234.55±20.68%. These were both significant increases from baseline ($p_{PY,short}$=7e-22, $p_{PY,long}$=3e-21, Bonferroni-corrected α=0.025 for 2 spindle types, one sample two-sided Wilcoxon signed-rank test, $z_{PY,short}$=9.62, $z_{PY,long}$=9.45). The mean percent of baseline spike rate for IN during shorter spindles was 160.16±10.46% and longer spindles was 164.36±11.41%. These were also both significant increases from baseline ($p_{IN,short}$=4e-6, $p_{IN,long}$=2e-6, Bonferroni-corrected α=0.025 for 2 spindle types, one sample two-sided Wilcoxon signed-rank test, $z_{IN,short}$=4.61, $z_{IN,long}$=4.71). There was no significant difference between PY for shorter vs. longer spindles or IN for shorter vs. longer spindles (p_{PY}=0.40, p_{IN}=0.18, Bonferroni-corrected α=0.025 for 2 unit types, paired two-sided Wilcoxon signed-rank test, z_{PY}=0.84, z_{IN}=-1.34). ****p<0.0001.

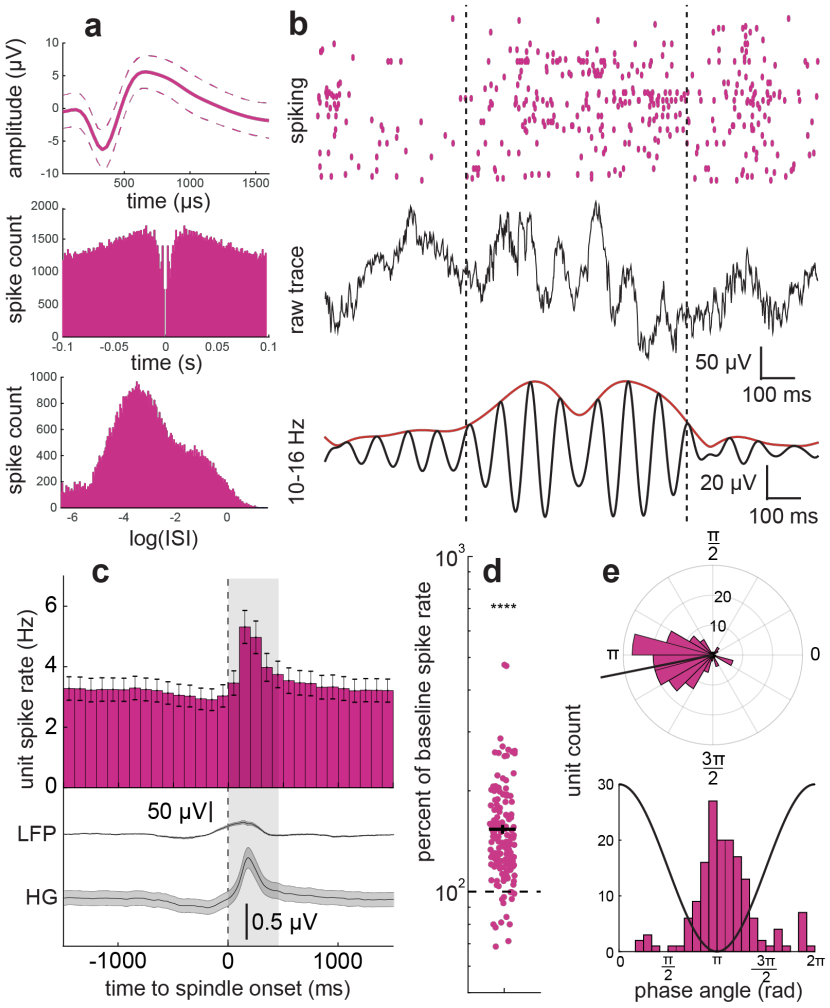

Supplementary Fig. 1.4. Multi-unit classification, spiking during spindles, and spindle phase preferences of spiking. (**A**) Average and standard deviation spike waveform (top), spike autocorrelation (middle), and ISI distribution (bottom) for an example MU. (**B**) Raw and 10-16 Hz bandpassed traces of an example spindle with raster plot of associated spiking of an example MU. (**C**) Mean MU spike rates, LFP, and HG envelope locked to spindle onsets at t=0 (n=158 units). Shaded gray box shows the mean spindle duration of 470 ms. Errors show SEM. (**D**) Mean MU spike rates during concatenated spindle epochs as log-percent of baseline spike rate (n=158 units). The mean and standard deviation baseline spike rate of MUs was 2.74±2.67 Hz. The mean and standard deviation spike rate of MUs during spindles was 3.70±3.38 Hz. MUs had a significant increase of 153.69±4.54% (SEM) in the mean percent of baseline spike rate during spindles (p=1e-27, one sample two-sided Wilcoxon signed-rank test, z=10.90). Baseline spike rate of each unit was computed by concatenating randomly selecting NREM epochs in between spindles that were matched in number and duration to the spindles. Color circles show the mean firing rate of each unit. Solid horizontal lines show mean and vertical show SEM. Dashed horizontal line shows baseline spike rate (100%). (**E**) Polar and non-polar histograms show circular mean spindle phases of MU spikes (mean=3.33 rad). There was a significant spindle phase preference for 58.23% of MUs (α=0.05, Hodges-Ajne test with bootstrapping significance). One cycle of a spindle is superimposed on the non-polar histogram to visualize the phase-spike relationship. Black line extending from polar histogram shows circular mean. HG=high gamma, LFP=local field potential, MU=multi-unit. ****p<0.0001.

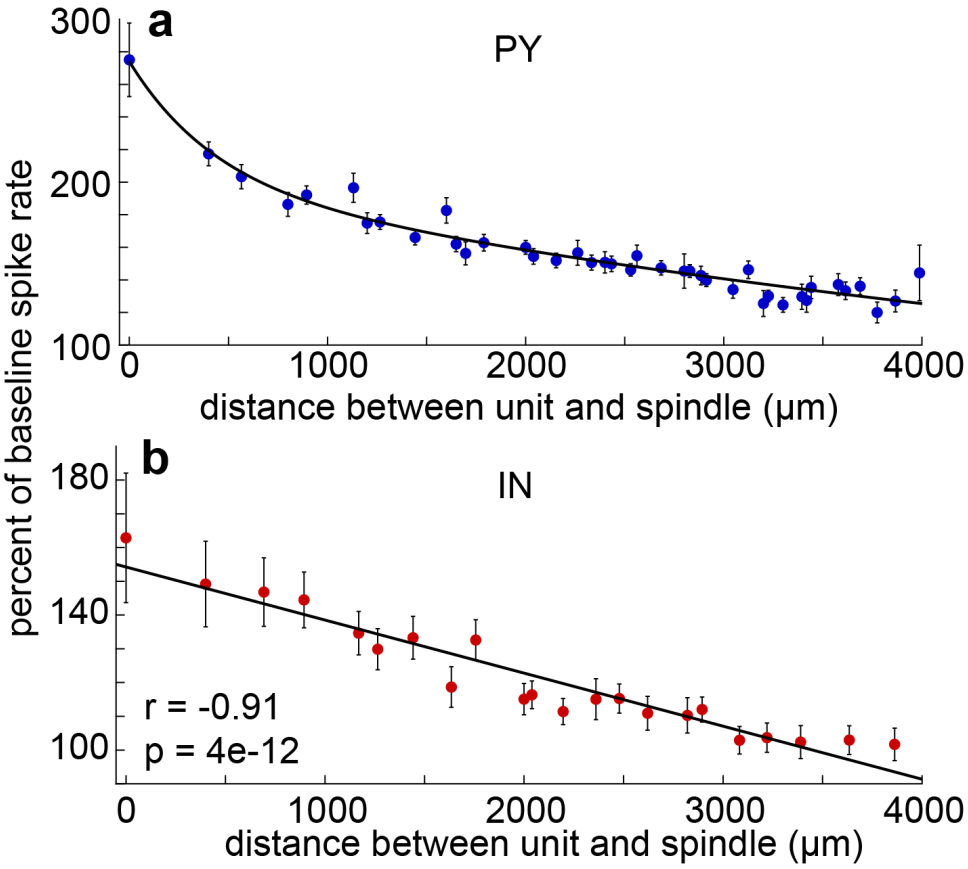

Supplementary Fig. 1.5. Unit spiking relative to distance to spindle. (**A**) Percent of baseline spike rate of PY for a co-located spindle (distance=0) or for spindles at progressively greater distances (n=50 unit-spindle channel pairs per point). Fit is two term exponential least squares regression (R^2=0.95). Note that PY unit spiking was greatest (~275% of baseline) when the unit channel was spindling (i.e., distance of 0) and decreased most sharply until ~1000 μm (~185% of baseline), at which point it decreased gradually (~125% of baseline at 4000 μm). (**B**) Same as (A) but for IN (n=50 unit-spindle channel pairs per point). IN unit spiking was also greatest when the unit's channel was spindling (~155% of baseline), and gradually decreased across space (~100% of baseline at 4000 μm) with a linear relationship (r=-0.91, p=4e-12, linear least squares regression, significance of the correlation coefficient). Therefore, the gradual decrease from ~1000-4000 μm for PY was similar to the gradual decrease from ~400-4000 μm for IN, and at shorter distances from the spindle PY spiking was greatly increased. Error bars show SEM.

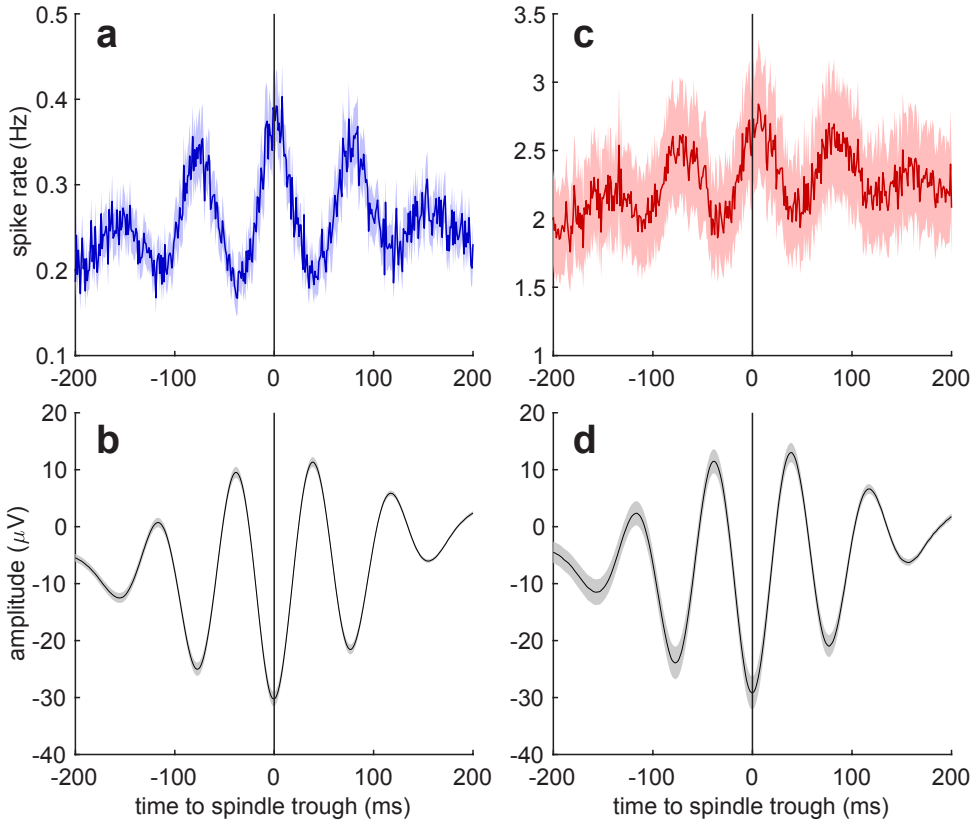

Supplementary Fig. 1.6. Spindle trough-locked unit spiking. (**A-B**) Mean spike rate of PY (**A**) and associated mean LFP (**B**) locked to all spindle troughs at t=0. (**C-D**) Same as (A-B) except for IN. Mean spike rates were Gaussian smoothed with a 50 ms window. Shaded error shows SEM.

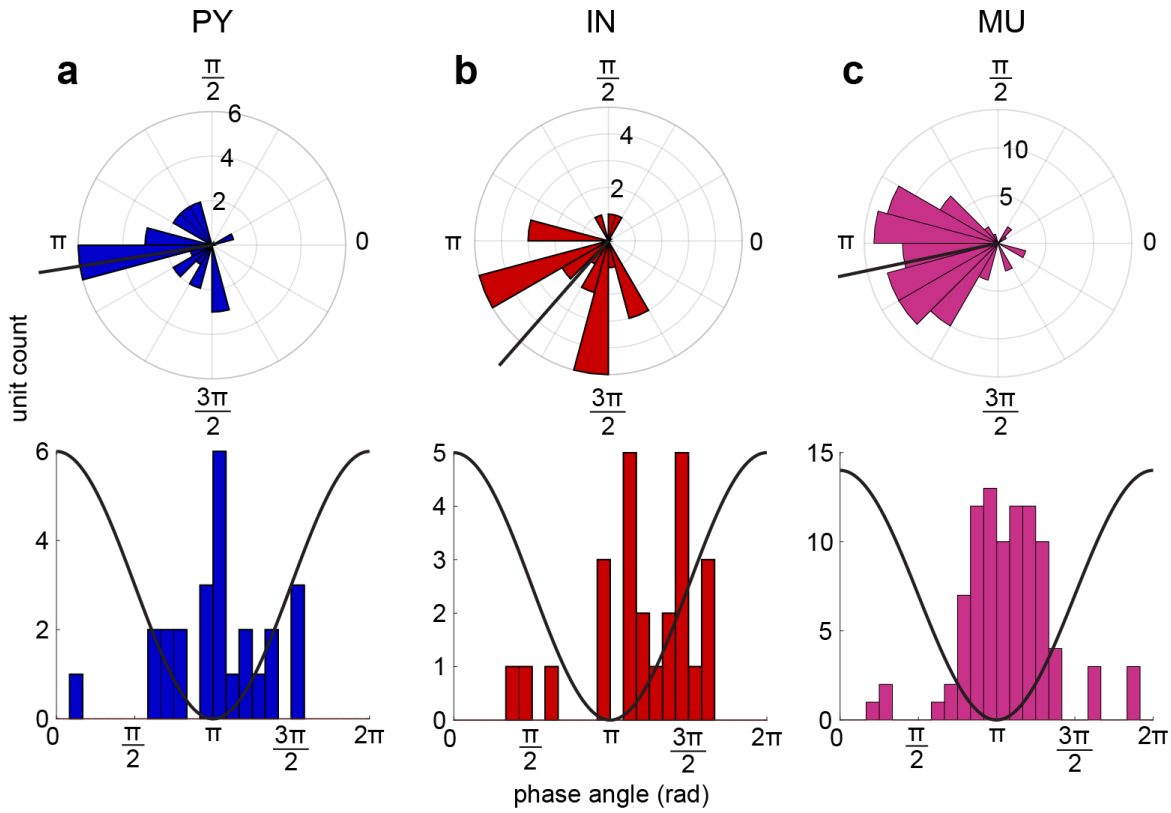

Supplementary Fig. 1.7. Spindle phase preference of units with statistically significant non-uniform spiking distributions. (**A-C**) Polar and non-polar histograms show circular mean spindle phases of spiking of PYs (**A**), INs (**B**), and MUs (**C**) with statistically significant non-uniform spike distributions (see Methods). Among the MUs with significant spindle phase preferences, the circular mean spindle phase of spiking was 3.34 rad. One cycle of a spindle is superimposed on non-polar histograms to visualize the phase-spike timing relationships. Black lines extending from polar histograms show circular means. MU=multi-unit.

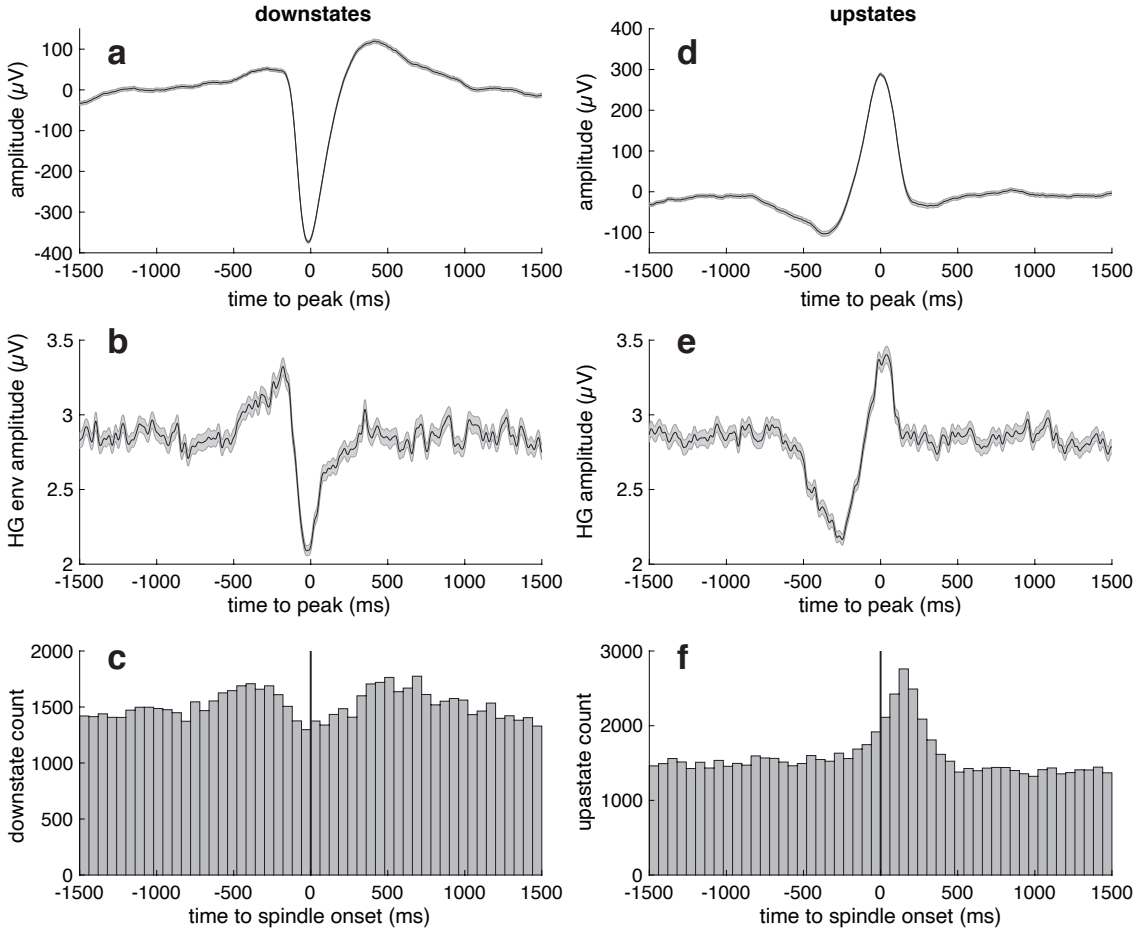

Supplementary Fig. 1.8. Downstates, upstates, and associated spindles. (**A-B**) Mean LFP (**A**) and HG analytic amplitude (**B**) of polarity corrected downstates for a representative channel. Means for both LFP and HG are relative to the LFP peak at t=0. Note that selected downstates were accompanied by upstates, and vice versa. (**C**) Peri-spindle onset time histogram of downstate peaks. (**D-F**) Same as (**A-C**) except for upstates. Shaded error shows SEM. HG=high gamma, LFP=local field potential.

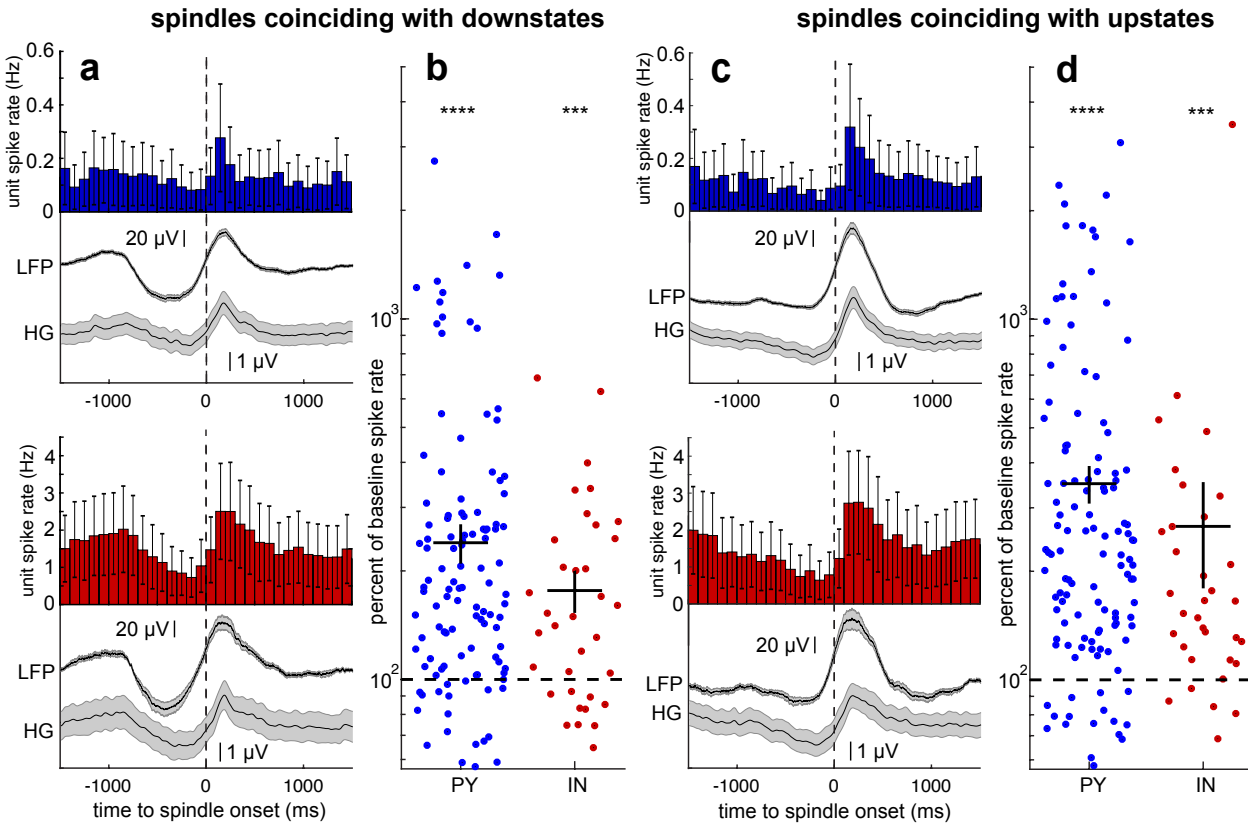

Supplementary Fig. 1.9. Unit spiking during spindles that occur with downstates or upstates. (**A**) PY (n=140) and IN (n=38) mean spike rates across units, and LFP and HG across unit channels relative to the onsets of spindles (t=0) that coincided with downstates, which were defined as spindles that had a downstate within 750 ms preceding their onsets. (**B**) PY (n=140) and IN (n=38) spike rates during concatenated spindles coinciding with downstates as a log-percent of baseline spike rates during concatenated NREM epochs matched in number and duration to the spindles. Solid horizontal lines show means. Dashed horizontal line shows baseline spike rate (100%). Spindles that coincided with downstates had a significantly increased spike rate from baseline (p_{PY}=7e-7, p_{IN}=0.001, Bonferroni-corrected α=0.025 for 2 unit types, one sample two-sided Wilcoxon signed-rank test, z_{PY}=4.97, z_{IN}=3.21). (**C-D**) Same as (**A-B**) except for spindles coinciding with upstates, which were defined as spindles that had an upstate within 500 ms following their onsets (n=125 PY, n=38 IN). Spindles that coincided with upstates also had a significantly increased spike rate from baseline (p_{PY}=2e-9, p_{IN}=0.003, Bonferroni-corrected α=0.025 for 2 unit types, one sample two-sided Wilcoxon signed-rank test, z_{PY}=6.02, z_{IN}=2.95). Only units that were detected on channels that had spindles that co-occurred with downstates (**A-B**) or upstates (**C-D**) were included. Note the similarities of the LFP traces and the similarities of the HG traces for spindles with downstates vs. upstates due to their systematic co-occurrence. These events were pooled for the analyses presented in the main text. HG=high gamma, LFP=local field potential. Errors show SEM. ****p<0.0001, ***p<0.001.

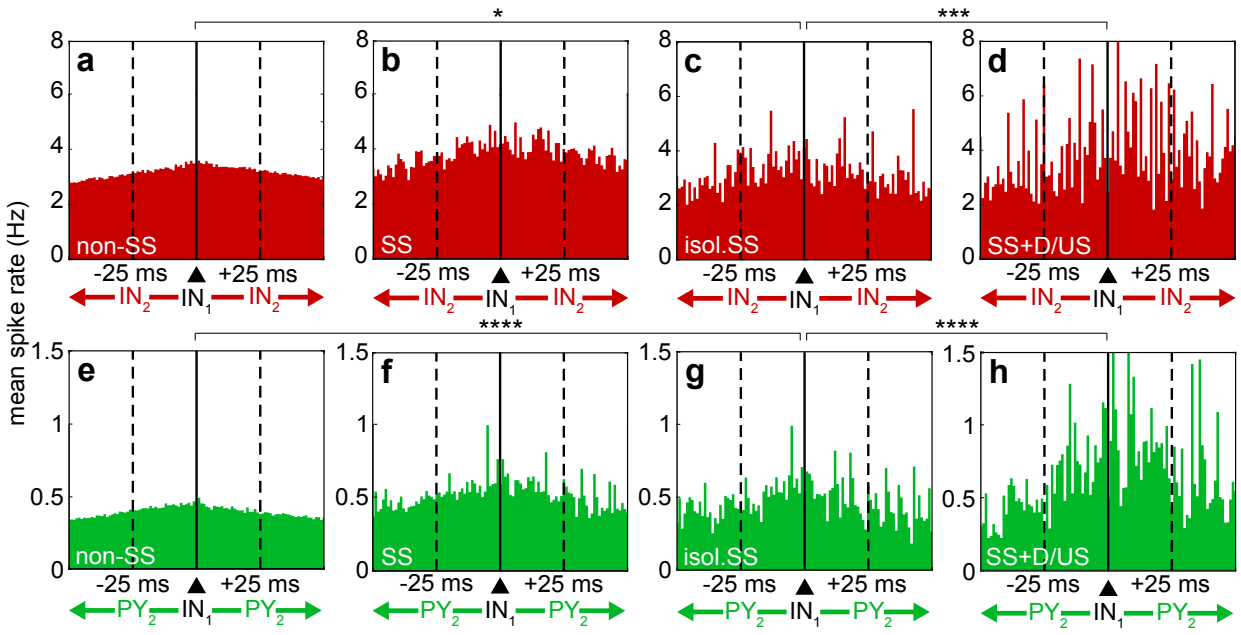

Supplementary Fig. 1.10. IN_1-IN_2 and IN_1-PY_2 co-firing during spindles. (**A**) In all pairs of IN_1-IN_2 recorded from different contacts, the firing of IN_2 is plotted relative to the time of IN_1 (at t=0) during non-spindle baseline epochs (**A**), spindles (**B**), isolated spindles that did not coincide with downstates or upstates (**C**), and spindles that coincided with down-to-upstates (**D**). (**E-H**) Same as (A-D) except for IN_1-PY_2. Solid vertical line shows t=0. Dashed vertical lines show the ±25 ms interval where paired pre- and post-synaptic spiking facilitates STDP. The mean and SEM co-firing rate within 25 ms for non-spindles vs. isolated spindles vs. spindles that coincided with down/upstates for IN_1-IN_2 was 3.31±0.17 vs. 3.60±0.27 vs. 3.97±0.35 Hz and for IN_1-PY_2 was 0.44±0.011 vs. 0.54±0.034 vs. 0.72±0.074 Hz. The co-firing rate during isolated spindles was significantly higher than non-spindles ($p_{IN\text{-}IN}$=0.016, $p_{IN\text{-}PY}$=3e-28, Bonferroni-corrected α=0.025 for 2 spindle types, paired two-sided Wilcoxon signed-rank test, $z_{IN\text{-}IN}$=2.41, $z_{IN\text{-}PY}$=11.01), and the co-firing rate during spindles that coincided with down/upstates was significantly higher than during isolated spindles ($p_{IN\text{-}IN}$=1e-4, $p_{IN\text{-}PY}$=2e-13, Bonferroni-corrected α=0.025 for 2 spindle types, paired two-sided Wilcoxon signed-rank test, $z_{IN\text{-}IN}$=3.80, $z_{IN\text{-}PY}$=7.37). *p<0.025, ***p<0.001, ****p<0.0001, paired two-sided Wilcoxon signed-rank test.

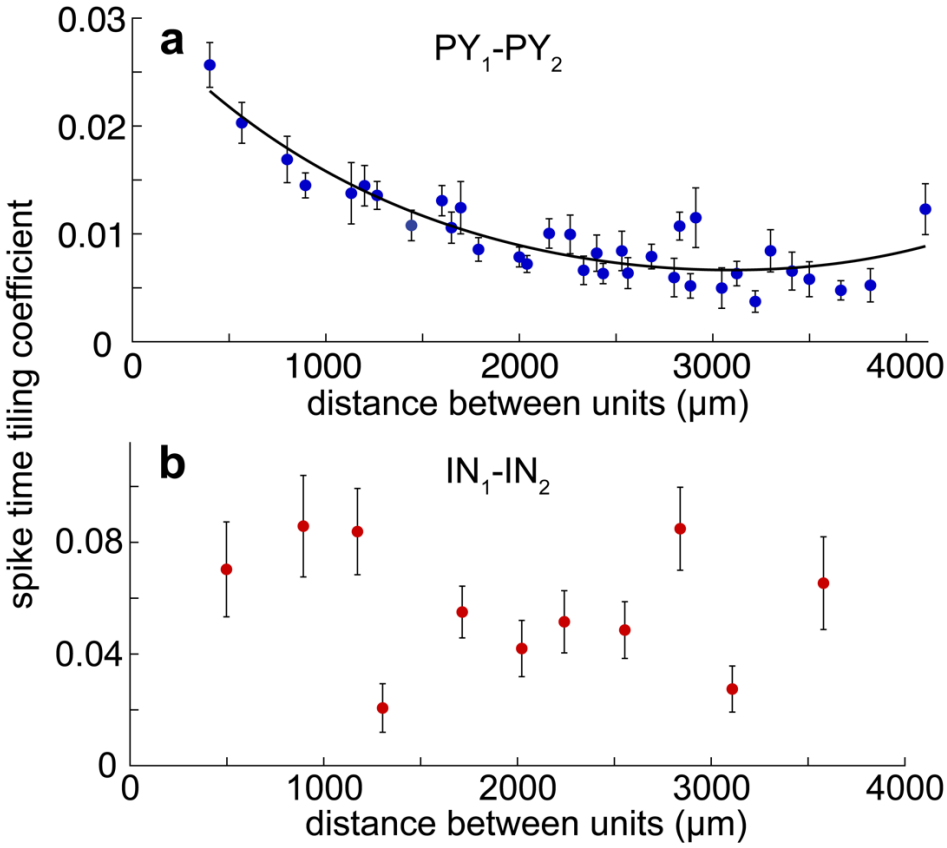

Supplementary Fig. 1.11. Unit pair co-firing across distance. The spike time tiling coefficient provides an alternative method for quantifying the tendency of units to fire in a correlated manner independent of firing rates (see Methods). We calculated the spike time tiling coefficient for PY_1-PY_2 (n=30 minimum unit pairs per point) and IN_1-IN_2 (n=30 minimum unit pairs per point) ±25 ms co-firing during all NREM periods included in this paper (consisting of stages N2 or N3). (**A-B**) Spike time tiling coefficient, which was used to measure the pairwise correlation within ±25 ms of spike trains for PY_1-PY_2 (**A**) and IN_1-IN_2 (**B**) as a function of the distance between units. PY_1-PY_2 correlations decreased with distance until ~2000 μm (R^2=0.83, two term exponential least squares regression). By contrast, IN_1-IN_2 correlations were larger overall and not dependent on distance at this scale. The PY_1-IN_2 and IN_1-PY_2 correlations are not reported since the spike time tiling coefficient test would not independently assess their correlations. Error bars show SEM.

Supplementary Table 1.1. Unit spiking and spindle phase-locking results for individual patients. (**A**) Mean spike rates during concatenated spindle epochs as a percent of spike rates during concatenated randomly selected non-spindle epochs matched in number and duration to the spindles. Error is SEM. No SEM was reported for patient 4 IN since there was only 1 IN detected in this patient. (**B**) Proportions of PY and IN with significant spindle phase preferences (α=0.05, Hodges-Ajne test with bootstrapping significance). IN=putative interneuron unit, PY=putative pyramidal unit, SEM=standard error of the mean.

Patient	a Spindle vs. baseline spike rate (%)		b Significantly phase-locked	
	PY	IN	PY	IN
1	166.50±10.28	162.34±16.26	16/69	15/23
2	342.64±49.48	260.65±91.75	3/46	4/8
3	127.73±10.98	145.20±31.23	4/16	6/7
4	232.37±24.05	189.93	2/14	0/1

Supplementary Table 1.2. Unit pair co-firing results for individual patients. (**A-C**) Percent of unit pairs with significantly increased (α=0.001, bootstrapped significance) co-firing within 25 ms during spindles vs. non-spindles (**A**), spindles vs. shuff-spindles (**B**), and both (**C**). (**D**) Percent of unit pairs in (C), which also had a minimum number of co-firing events of 10 within ±25 ms, with significant order preference of co-firing within ±25 ms (α=0.05, two-sided χ^2 test of proportions). N/A is indicated for Patient 4 IN_1-IN_2 since this patient had only 1 detected IN and otherwise when there was not a minimum of 10 co-firing events within ±25 ms.

Patient	a Paired co-firing: spindles vs. non-spindles				b Paired co-firing: spindles vs. shuff-spindles			
	PY_1-PY_2	IN_1-IN_2	PY_1-IN_2	IN_1-PY_2	PY_1-PY_2	IN_1-IN_2	PY_1-IN_2	IN_1-PY_2
1	1010/4638 21.78%	208/490 42.45%	410/1561 26.27%	547/1561 35.04%	295/4638 6.36%	140/490 28.57%	110/1561 7.05%	212/1561 13.58%
2	159/2910 5.46%	32/54 59.26%	111/430 25.81%	109/430 25.35%	151/2910 5.19%	36/54 66.67%	27/430 6.28%	8/430 1.86%
3	19/298 6.38%	19/36 52.78%	26/122 21.31%	32/122 26.23%	12/298 4.03%	12/36 33.33%	10/122 8.2%	6/122 4.92%
4	97/180 53.89%	N/A	12/14 85.71%	13/14 92.86%	38/180 21.11%	N/A	4/14 28.57%	9/14 64.29%
	c Paired co-firing: Both				d Ordered co-firing			
1	245/4638 5.28%	106/490 21.63%	89/1561 5.7%	193/1561 12.36%	14/77 18.18%	13/102 12.75%	9/64 14.06%	35/171 20.47%
2	145/2910 4.98%	28/54 51.85%	27/430 6.28%	8/430 1.86%	N/A	2/4 50%	N/A	N/A
3	8/298 2.68%	11/36 30.56%	5/122 4.1%	4/122 3.28%	N/A	3/10 30.00%	1/4 25.00%	1/3 33.33%
4	36/180 20%	N/A	4/14 28.57%	9/14 64.29%	4/17 23.53%	N/A	2/4 50.00%	3/9 33.33%

Supplementary Table 1.3. Order preference of significant unit pair co-firing. For each PY-PY or IN-IN pair included in the co-firing analyses, also included was a pair of the same units but tested in the reversed order. Values are percent of sets of pairs that were significant in one direction only ("sig one dir") or both directions ("sig both dir") for spindles vs. non-spindles, spindles vs. shuff-spindles, and both tests.

Pair Type	Directionality	Spindles vs. non-spindles	Spindles vs. shuff-spindles	Both
PY-PY	sig one dir	18.04%	8.72%	6.25%
	sig both dir	6.83%	1.74%	1.45%
IN-IN	sig one dir	20.34%	18.62%	8.62%
	sig both dir	34.48%	23.10%	16.21%

Supplementary Table 1.4. Unit pair co-firing rates according to co-firing delay and spindle coherence. Mean and standard deviation unit pair co-firing rates during co-occurring spindles for shorter co-firing lags (<10 ms) and higher spindle coherence (>0.90), shorter lags and lower coherence (<0.50), longer lags (51-100 ms) and higher coherence, and longer lags and lower coherence during baseline NREM periods in between spindles.

	<10 ms, >0.90 coh	<10 ms, <0.50 coh	51-100 ms, >0.90 coh	baseline
PY_1-PY_2	0.96±0.85 Hz	0.78±0.86 Hz	0.60±0.68 Hz	0.25±0.06 Hz
IN_1-IN_2	4.25±3.44 Hz	3.76±3.01 Hz	2.56±2.51 Hz	2.68±0.48 Hz
PY_1-IN_2	4.04±3.91 Hz	3.03±3.75 Hz	2.41±3.04 Hz	1.40±0.15 Hz
IN_1-PY_2	1.05±1.16 Hz	0.53±0.86 Hz	0.64±0.68 Hz	0.28±0.02 Hz

Chapter 1, in full, is a reprint of the material as it appears in: Dickey CW, Sargsyan A, Madsen JR, Eskandar EN, Cash SS, Halgren E. Travelling spindles create necessary conditions for spike-timing-dependent plasticity in humans. *Nature Communications*. 2021;12(1):1027. doi:10.1038/s41467-021-21298-x.

Chapter 2: Cortical ripples provide the conditions for consolidation during NREM sleep in humans

Abstract:

Hippocampal ripples index the reconstruction of spatiotemporal neuronal firing patterns essential for the consolidation of memories in the cortex during non-rapid eye movement (NREM) sleep. However, it is not known whether ripples are generated in the human cortex during sleep. Here, using human intracranial recordings, we show that ~70ms long ~80Hz ripples are ubiquitous in all regions of the cortex during NREM sleep as well as waking. During waking, cortical ripples occur on local high frequency activity peaks. During sleep, cortical ripples occur during spindles on the down-to-upstate transition, with unit-firing patterns consistent with generation by pyramidal-interneuron feedback. Cortical ripples mark the recurrence of spatiotemporal activity patterns from preceding waking, and they group co-firing within the window of spike-timing-dependent plasticity. Thus, cortical ripples guided by sequential sleep waves may facilitate memory consolidation during NREM sleep in humans.

Introduction:

Ripples have been extensively studied in rodent hippocampus during non-rapid eye movement (NREM) sleep, when they mark the replay of events from the prior waking period, and are critical for memory consolidation in the cortex (Buzsaki, 2015; Ego-Stengel et al., 2009; Maingret et al., 2016; Wilson et al., 1994). They are associated with cortical replay (Ji et al., 2007; Johnson et al., 2010; Peyrache et al., 2009), and with cortical sleep waves (spindles, downstates, upstates) (Siapas et al., 1998), a relationship crucial for consolidation (Latchoumane et al., 2017). Rat hippocampal ripples comprise a ~140Hz oscillation at the peak of a ~70ms duration sharpwave, followed by a slower local potential (Buzsaki, 2015). Human hippocampal sharpwave-ripples also occur during NREM sleep with similar temporal relationships to spindles and down-to-upstates and hippocampal topography, but with a median frequency of 80-90Hz (Jiang et al., 2019a, 2019b; Jiang et al., 2019c; Staresina et al., 2015).

Recently, ripples were found in rat association cortex but not primary sensory or motor cortices during sleep, with increased coupling to hippocampal ripples in sleep following learning (Khodagholy et al., 2017). An earlier study reported ripples in waking and sleeping cat cortex, especially during NREM sleep (Grenier et al., 2001). In humans, cortical ripples during waking were more frequently found in lateral temporal than rolandic cortex, and coupled to parahippocampal gyrus ripples more often prior to correct paired-associates recall (Vaz et al., 2019). Lateral temporal units fired in-phase with the local ripples in patterns previously observed during learning (Vaz et al., 2020). Waking hippocampal ripples were also associated with cortical activity patterns selective for faces and buildings during free recall (Norman et al., 2019).

Thus, there is an emerging appreciation that, in humans and rodents, hippocampal and cortical ripples play an important role in memory during both sleep and waking. However, many fundamental questions remain unresolved, including whether cortical ripples are generated during sleep in humans. The basic characteristics of ripples have not been compared between cortex and hippocampus, or between sleep and waking, so it is unclear how ripples may differ between their putative roles of supporting consolidation vs. recall, or indeed if they represent the same phenomenon. Knowledge of the distribution of ripples across different cortical areas during waking is limited and during sleep is absent. The relations between cortical ripples and sleep spindles, downstates, and upstates have not been determined. Such relations could support a role of cortical ripples in consolidation, as would increased unit pair co-firing within the window of spike-timing-dependent plasticity (STDP), as well as association with spatiotemporal activity patterns identified during waking that ‘replay’ during subsequent sleep. Furthermore, the relationships of human cortical pyramidal and inhibitory cell-firing to ripples and to each other, important for understanding ripple generation, have not been determined.

Here, using intracranial stereoelectroencephalography (SEEG) recordings, we provide the first demonstration that cortical ripples are generated during NREM sleep in humans, and we make the first comprehensive characterization of ripples throughout the cortex during waking and NREM sleep. We show that cortical ripples in NREM sleep couple to spindles and down-to-upstates with timing that could

support consolidation, and to spatiotemporal patterns that recur from preceding waking, suggesting a possible role for ripples in memory replay. Using single-unit recordings from cortical microarrays, we identify the probable generating circuits of cortical ripples and show that units co-fire during ripples at short delays that are optimal for STDP. Thus, cortical ripples have the necessary physiological properties to facilitate replay-guided plasticity during non-rapid eye movement sleep in humans.

Results:

Ripples are generated across states and structures

Ripples were detected using intracranial cortical and hippocampal stereoelectroencephalography (SEEG) recordings in 17 patients undergoing monitoring for seizure focus localization (STable 2.1). Bipolar derivations ensured measurement of local field potentials (LFP). Ripples were detected exclusively from non-lesional, non-epileptogenic regions and were required to have at least 3 cycles of increased 70-100Hz amplitude without contamination by epileptiform activity or artifacts (SFig. 2.1). Ripples were found during both waking and NREM sleep in all cortical areas sampled (Fig. 2.1A-B,E-H, Table 2.1, SFig. 2.2), and hippocampus (Fig. 2.1C-D).

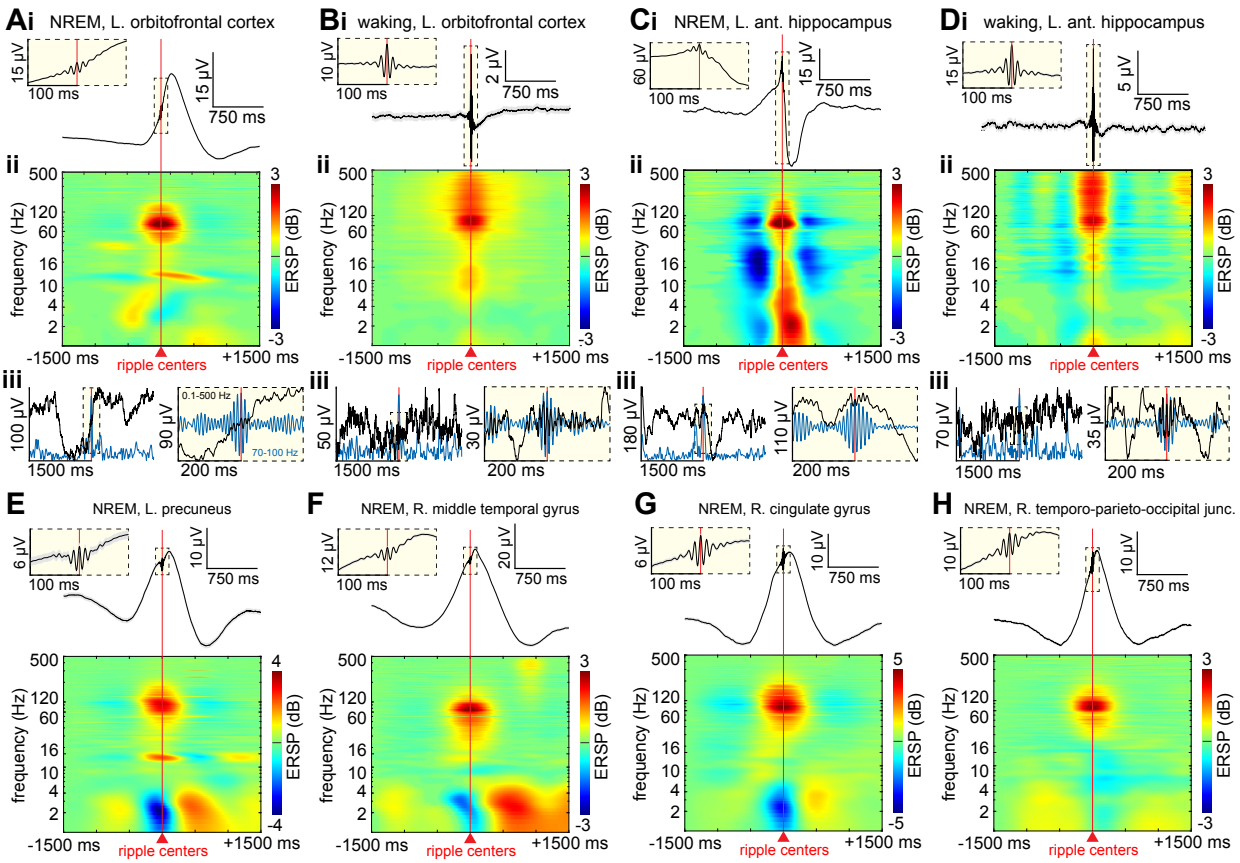

Fig. 2.1. Cortical and hippocampal ripples are generated during NREM sleep and waking. (**A**) Orbitofrontal average broadband LFP (**i**) and time-frequency (**ii**) across ripples, and example broadband ripple (**iii**) broadband sweeps (black, left–3000ms, right–400ms), and 70-100Hz bandpass (blue, left-analytic amplitude, right-sweep), from one channel during NREM sleep. Note the increased power in the 10-16Hz spindle band coinciding with the ripples. (**B**) Same as (A) except during waking. (**C**) Same as (A) except hippocampal ripples. (**D**) Same as (C) except during waking. (**E-H**) Same as (A) except for other cortical regions. Note the highly consistent occurrence of cortical ripples on the down-to-upstate transition during NREM sleep. All plots show ripples detected on trans-gray matter bipolar SEEG channels. LFP=local field potential, NREM=non-rapid eye movement, SEEG=stereoelectroencephalography.

Table 2.1. Cortical and hippocampal ripple characteristics by region in NREM sleep and waking. Cortical parcellation scheme is specified in STable 2.6. Values are counts or means and standard deviations across channels from SEEG patients S1-17.

Cortical Region	No. Chan	No. Ripples		Density (min^{-1})		Amplitude (μV)		Frequency (Hz)		Duration (ms)	
		Sleep	Waking	Sleep	Waking	Sleep	Waking	Sleep	Waking	Sleep	Waking
Orbitofrontal	14	129680	211957	9.01±2.74	4.83±3.26	1.31±0.26	2.26±1.21	80.3±0.4	80.8±0.7	64.1±4.5	57.8±3.0
Prefrontal	37	287124	609692	9.28±2.66	6.62±3.11	1.62±0.57	2.10±0.82	80.7±0.5	81.0±0.5	62.4±3.9	56.7±2.7
Rolandic	25	174262	315588	8.84±2.57	6.7±3.23	1.82±0.91	2.57±1.43	81.2±0.9	81.3±0.6	63.9±5.5	57.8±3.3
Parietal	79	491431	855766	8.18±2.68	5.17±3.45	1.76±0.64	2.44±1.09	81.3±0.7	81.3±0.5	65.5±6.6	58.2±3.7
Occipital	14	94144	103609	8.71±2.91	4.55±3.8	1.95±0.74	2.99±1.21	81.5±0.4	81.3±0.4	68.3±5.7	57.4±3.0
Superior Temporal / Insula	20	182981	324005	8.99±2.08	7.90±4.15	1.50±0.61	2.39±1.29	80.8±0.7	81.2±0.6	64.0±7.2	57.1±3.2
Lateral Temporal	47	295324	534754	6.89±2.61	4.95±3.35	1.23±0.71	1.89±1.34	80.7±0.9	81.2±0.7	63.6±8.4	58.0±3.4
Ventral Temporal	34	224478	415057	8.58±2.64	6.54±2.82	1.85±0.78	2.60±1.67	81±0.9	81.2±0.7	66.9±5.6	61.1±6.5
Cingulate	3	27078	42804	9.31±1.84	7.00±2.17	1.19±0.79	1.49±0.92	82.5±2.8	82.5±2.0	68.3±8.6	74.3±30.2
Hippocampus	28	147138	409734	6.95±4.80	7.40±5.50	5.79±2.99	5.25±3.01	78.9±4.4	80.5±4.4	85.0±34.9	69.6±28.6

Across states and structures, ripple frequency was remarkably consistent (~80Hz), durations were similar (~70ms), and spontaneous cortical ripple occurrence rate was higher during NREM sleep than waking (Figs. 2.2-3). Recording epochs and channels with possible contamination by epileptiform activity were rigorously rejected, and these basic ripple characteristics were very similar when only cortical or hippocampal channels free of interictal spikes were analyzed (SFig. 2.1B-C). Previous work in sleeping rats (Khodagholy et al., 2017) and waking humans (Vaz et al., 2019) found cortical ripples to be absent or infrequent in early sensory and motor as compared to association areas. In contrast, we found that ripple density, amplitude, and accompanying >200Hz amplitude (a proxy for unit-firing (Mukamel et al., 2005)), were all lower in association areas, as indicated by a positive correlation with the myelination index (Rosen et al., 2021) (Fig. 2.3G-H, SFig. 2.3).

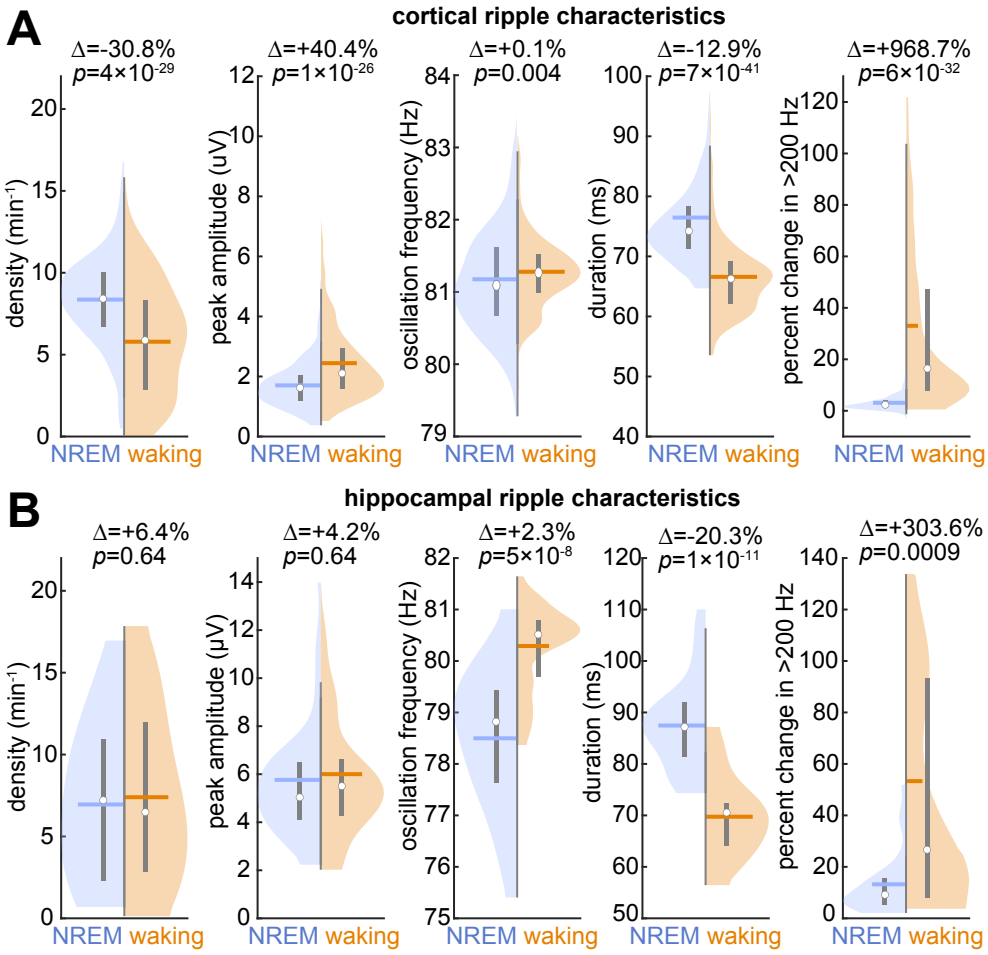

Fig. 2.2. Cortical and hippocampal ripple characteristics in NREM sleep and waking. (**A**) NREM sleep vs. waking cortical ripple density, peak 70-100Hz amplitude, frequency, duration, and percent change in mean >200Hz amplitude during ripples compared to a -2 to -1s baseline (*N*=273 channels; SEEG patients S1-17). (**B**) Same as (A) except hippocampal ripples (*N*=28 channels). Circles show medians; horizontal lines, means; vertical lines, interquartile ranges. FDR-corrected *p*-values, two-sided paired *t*-test. FDR=false discovery rate.

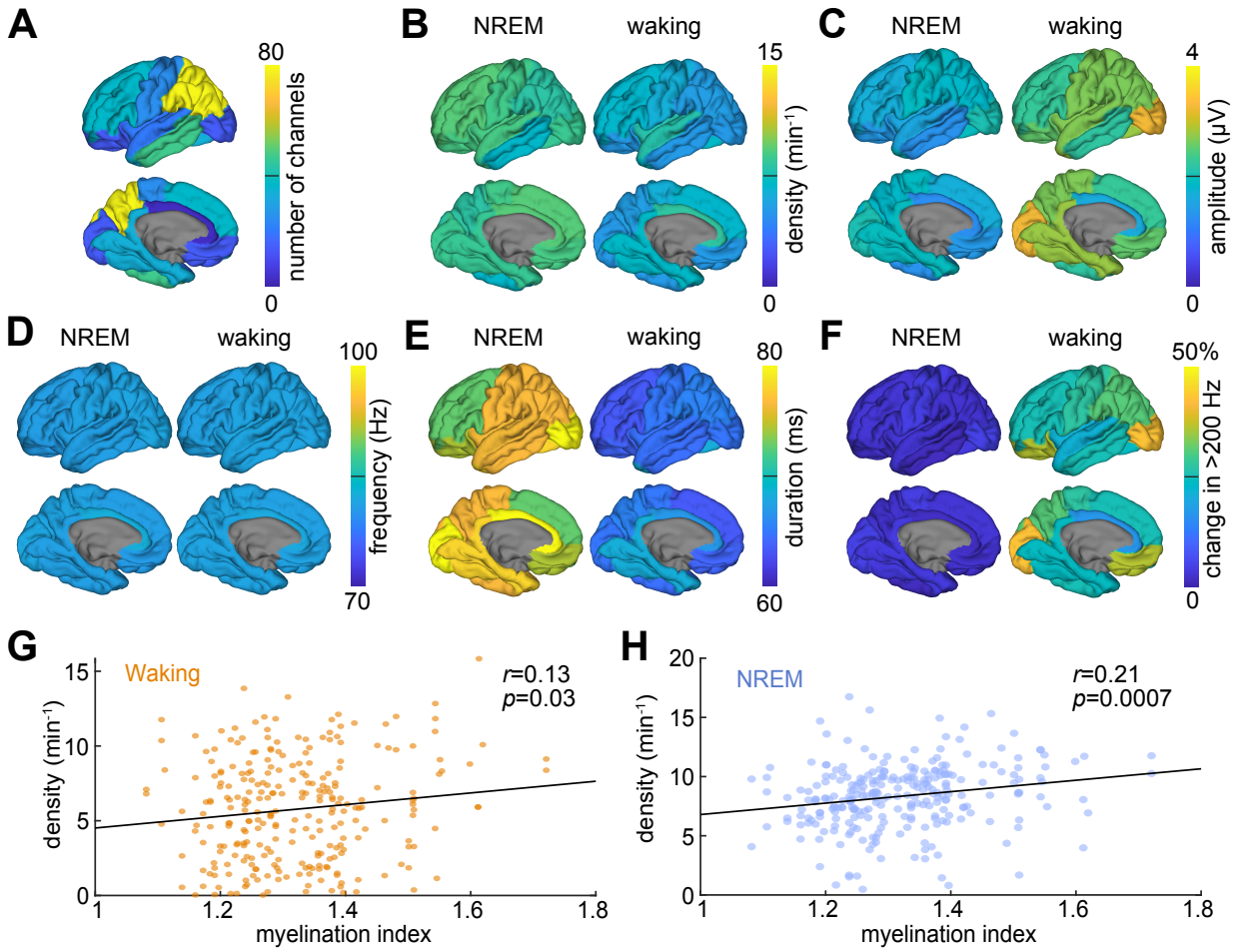

Fig. 2.3 Distributions of ripple characteristics across the cortex in NREM sleep and waking. (**A-F**) Cortical maps of channel coverage (**A**) as well as mean ripple densities (**B**), amplitudes (**C**), frequencies (**D**), durations (**E**), and changes in mean >200Hz analytic amplitude during ripples compared to baseline (-2 to -1s) (**F**) during NREM sleep and waking (*N*=273 channels; SEEG patients S1-17). Left and right hemisphere channels were combined and mapped onto a left hemisphere template brain. Parcellation scheme is specified in STable 2.6. Values for each cortical region are reported in Table 2.1. (**G-H**) Cortical ripple density was positively correlated with cortical parcel myelination index (i.e., lower densities in association compared to primary areas (Rosen et al., 2021)) during waking (**G**) and NREM sleep (**H**). Amplitude and oscillation frequency during waking and NREM sleep, and change in >200Hz amplitude during NREM sleep also had significant positive linear correlations, but duration in either state and change in >200Hz amplitude during waking were non-significant (SFig. 2.3).

Cortical ripples lock to sleep waves crucial for memory consolidation

NREM sleep is characterized by large downstates, often followed by upstates with spindles (Gonzalez et al., 2018; Mak-McCully et al., 2017). Hippocampal ripples tend to occur on the cortical down-to-upstate transition with spindles in rodents (Johnson et al., 2010; Siapas et al., 1998) and humans (Jiang et al., 2019a; Staresina et al., 2015). These precise oscillation couplings are important for memory

consolidation (Latchoumane et al., 2017). Previous studies have shown that cortical ripples occur on upstate and spindle peaks in cats (Grenier et al., 2001) and rats (Khodagholy et al., 2017), but these relationships have not been evaluated in humans. We detected downstates, upstates, and spindles (STable 2.2) and found that cortical ripples were precisely coupled to the sequence of sleep waves described above. Specifically, cortical ripples were generated on the down-to-upstate transition (Fig. 2.1A,E-H, Fig. 2.4A-B,D, SFig. 2.2A), often on spindles (Fig. 2.1A,E, Fig. 2.4A,C, STable 2.3), with a preference for spindles preceding upstates (Fig. 2.4E). These results suggest that cortical ripples may help to facilitate consolidation, guided by a sequential activation of sleep waves.

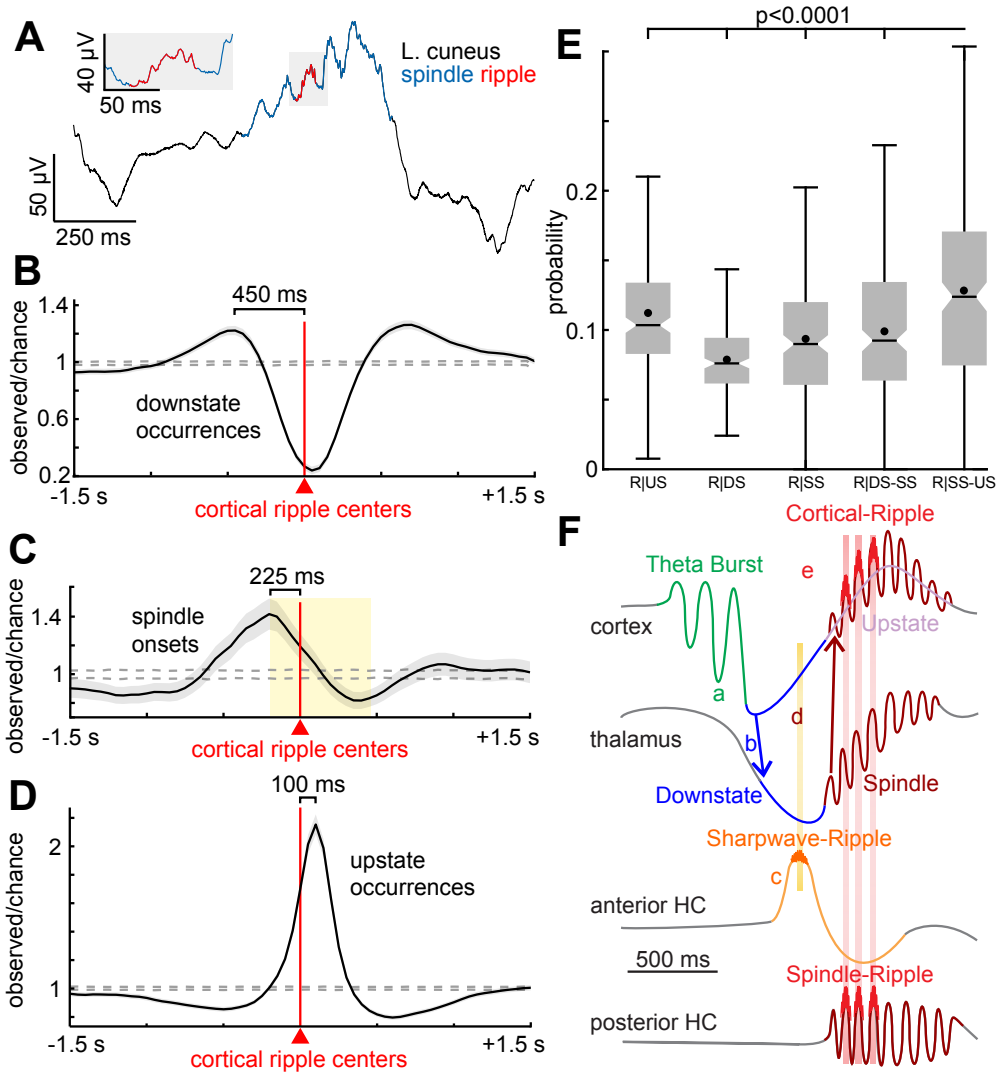

Fig. 2.4. Cortical ripples occur during sleep spindles on the down-to-upstate transition. (**A**) Example cortical ripple occurring during a spindle on a down-to-upstate transition. (**B**) Smoothed histogram shows average downstate peak times plotted relative to local cortical ripple centers at t=0 across significant channels (N=258/273, patients S1-17). Dashed lines show 99% confidence interval of the null distribution (200 shuffles/channel). (**C-D**) Same as (B) except spindle onsets (N=80/273) (**C**) with shaded area indicating average spindle duration, and downstate peaks (N=260/273) (**D**). (**E**) Probabilities of ripple centers (R) preceding upstates (US), following downstates (DS), or occurring during spindles (SS), spindles following downstates (DS-SS), or spindles preceding upstates (SS-US; N=212 channels from patients S1-17; minimum 20 events of each type required per channel). The time window used following downstates or preceding upstates was 634ms, which was the average spindle duration. The probability of a ripple occurring was greatest during spindles preceding upstates (post-FDR p<0.0001, paired two-sided t-test). (**F**) Timing of ripples, spindles, and down-to-upstates across structures. A cortical theta burst leads to a downstate (Gonzalez et al., 2018) (*a*) which triggers a thalamic-downstate (*b*) and rebound hippocampal sharpwave-ripple (Jiang et al., 2019a) (*c*) arriving at the cortex rebooting from its downstate; meanwhile, the thalamic-downstate enables h and T currents to generate a spindle projected to the cortex (Mak-McCully et al., 2017) (*d*) with phase-locked posterior hippocampal spindle-ripples (Jiang et al., 2019b). Overall, cortical ripples during NREM sleep occur on the down-to-upstate slope, often during spindles (*e*). HC=hippocampus.

Pyramidal cell firing precedes interneuron firing at cortical ripple peaks

Using microelectrode array recordings from granular/supragranular layers of lateral temporal cortex during NREM sleep, we detected ripples (Fig. 2.5A) as well as action-potentials, which were sorted into those arising from putative single pyramidal cells or interneurons (SFig. 2.4, STable 2.4). We found that interneurons showed a strong tendency to fire at the peak of the ripple, whereas pyramidal cells fired shortly before (Fig. 2.5B). We have previously shown that, in humans, upstates (Csercsa et al., 2010) and spindles (Dickey et al., 2021a) are associated with increased unit-firing rates. Since cortical ripples are precisely coupled to these events (Fig. 2.4), their occurrence on upstates and spindles implies an underlying phasic depolarization, which can generate ~80Hz oscillations in computational and experimental models via pyramidal-interneuron feedback inhibition (Bazhenov et al., 2008; Buzsaki, 2015). Depolarization causes basket cells to fire synchronously, inhibiting other basket cells and pyramids via $GABA_A$. Pyramids fire upon recovery, exciting basket cells as they recover, leading to another cycle. As this model would predict, we found that pyramids and interneurons were strongly phase-locked to cortical ripples (Fig. 2.5B-C), with pyramidal significantly leading interneuron spiking (Fig. 2.5D). Furthermore, interneurons fired at ripple peak, when pyramidal somatic inhibition would be maximal, as found in cats (Grenier et al., 2001). Similarly, ripple amplitude was higher in waking than NREM sleep (Figs. 2.2B, 3C), consistent with relative depolarization of pyramidal membrane potential during waking. Phasic depolarization during waking ripples was also suggested by increased >200Hz amplitude (Figs. 2.2, 3F). Thus, human cortical ripples are associated with strong tonic and phase-locked increases in pyramidal and interneuron firing, and are likely generated by a sudden depolarization triggering pyramidal-interneuron feedback oscillations (Fig. 2.5E).

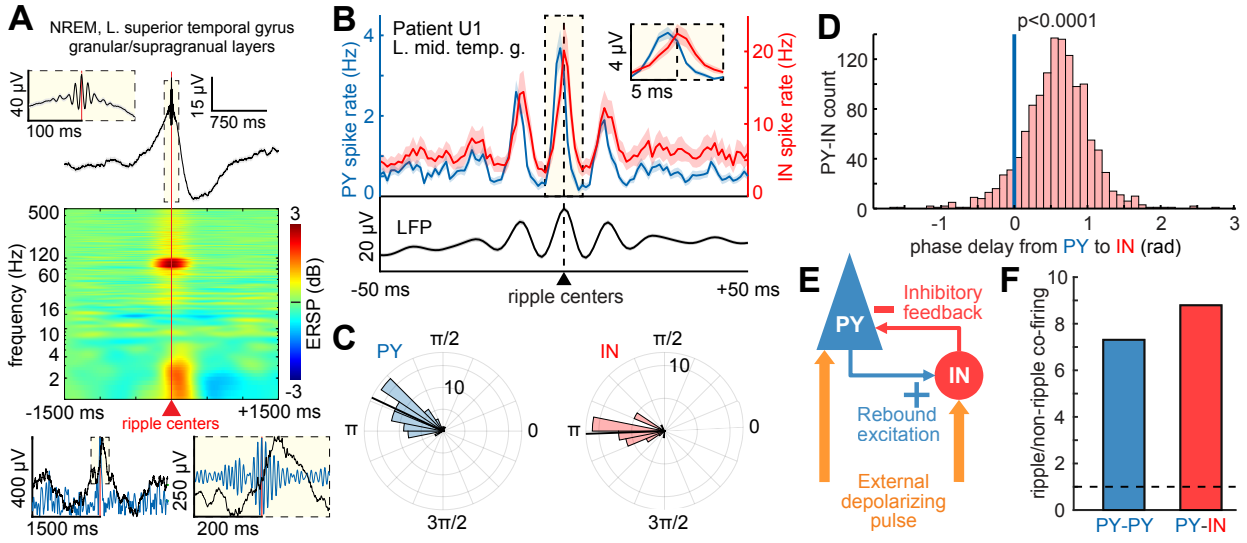

Fig. 2.5. Pyramidal cell firing leads interneuronal at cortical ripple peaks. (**A**) Superior temporal gyrus granular/supragranular layer ripples detected during NREM sleep in a Utah Array recording. Top shows average broadband LFP, middle shows average time-frequency, and bottom shows single trial example trace in broadband LFP (black) and 70-100Hz bandpass (blue, left–analytic amplitude, right–sweep). (**B**) Mean broadband LFP locked to cortical ripple centers (black) and associated local PY (*N*=69) and IN (*N*=23) spike rates during NREM sleep. (**C**) Circular mean 70-100Hz phase of spikes of each PY (*N*=73, mean=2.70rad, $p=2\times10^{-7}$, Hodges-Ajne test) and IN (*N*=36, mean=3.18rad, p≈0) during local cortical ripples (minimum 30 spikes per unit). PY spiking preceded IN spiking by 0.48rad ($p=2\times10^{-7}$, Watson-Williams test). (**D**) Circular mean ripple phase-lags of spikes from each PY (*N*=73) to each IN (*N*=36) (*N*=1280 unit pairs, mean=0.58±0.46rad, $p=1\times10^{-268}$, one-sample one-sided *t*-test). (**E**) Pyramidal Interneuron Network Gamma ripple generation mechanism consistent with single-unit recordings, animal studies (Stark et al., 2014), and modelling (Buzsáki et al., 2012). Abrupt depolarization causes synchronous PY and IN firing, which then spike rhythmically separated by fixed intervals due to recurrent inhibition. (**F**) Pairs of pyramidal cells (PY-PY) co-fire ~7 times more often within 5ms of each other during ripples compared to randomly selected epochs in between ripples matched in number and duration to the ripples. Similarly, pyramidal-interneuron (PY-IN) pairs co-fire ~9 times more during ripples. IN=putative interneuron, PY=putative pyramidal.

Cortical ripples group co-firing with timing optimal for spike-timing-dependent plasticity

The increased phase-locked unit firing and occurrence of ripples on spindles on the down-to-upstate transition suggest that ripples may facilitate cortical plasticity (Dickey et al., 2021a). This could occur through short latency co-firing between units that leads to STDP. Indeed, we found a large increase during ripples of short latency (<5ms) co-firing between pyramidal-pyramidal unit pairs and pyramidal-interneuron unit pairs (Fig. 2.5F). Specifically, there was an increase in co-firing during ripples vs. non-ripples (PY-PY: 7.31 fold increase, $p=6\times10^{-193}$, *N*=7846, *t*=30.5; PY-IN: 8.79 fold increase, $p=1\times10^{-177}$, *N*=2113, *t*=29.0; paired two-sided *t*-test). Non-ripple comparison periods were randomly selected epochs

between ripples matched in number and duration. There was also a significant increase in short-latency co-firing in actual ripples, as compared to co-firing when the spike times within the ripples were randomly shuffled (PY-PY: 1.27 fold increase, $p=3\times10^{-12}$, $N=7846$, $t=7.0$; PY-IN: 1.18 fold increase, $p=2\times10^{-15}$, $N=2113$, $t=7.9$; paired two-sided t-test). This latter finding indicates that the increase in co-firing is not simply due to an increase in the overall firing rates of units during ripples, or even their rhythmicity, but rather a specific organization of co-firing by the phase of individual ripple cycles. Thus, ripples create a necessary and sufficient condition for STDP, and therefore may underlie the crucial contribution of these nested waves to consolidation (Dickey et al., 2021a).

Cortical ripples mark 'replay' of spatiotemporal activity patterns

Hippocampal ripples in NREM sleep mark the assembly of spatiotemporal firing patterns reproducing the sequential attributes of events from the preceding waking, supporting cortical replay and consolidation (Buzsaki, 2015; Rasch et al., 2013). However, cortical ripples have not been associated with replay during NREM sleep. Our group previously identified waking spatiotemporal patterns of high gamma (70-190Hz) activity across widespread cortical areas that recurred more often in the following compared to preceding sleep nights (Fig. 2.6A). These events also coupled to upstates, spindles and hippocampal ripples (Jiang et al., 2017). In new analyses of these data (STable 2.5), we found that the high gamma events that comprised these sequences of putative replay were strongly linked to cortical ripples (Fig. 2.6B-E), supporting the possibility that cortical ripples contribute to replay underlying the consolidation of memories in the cortex.

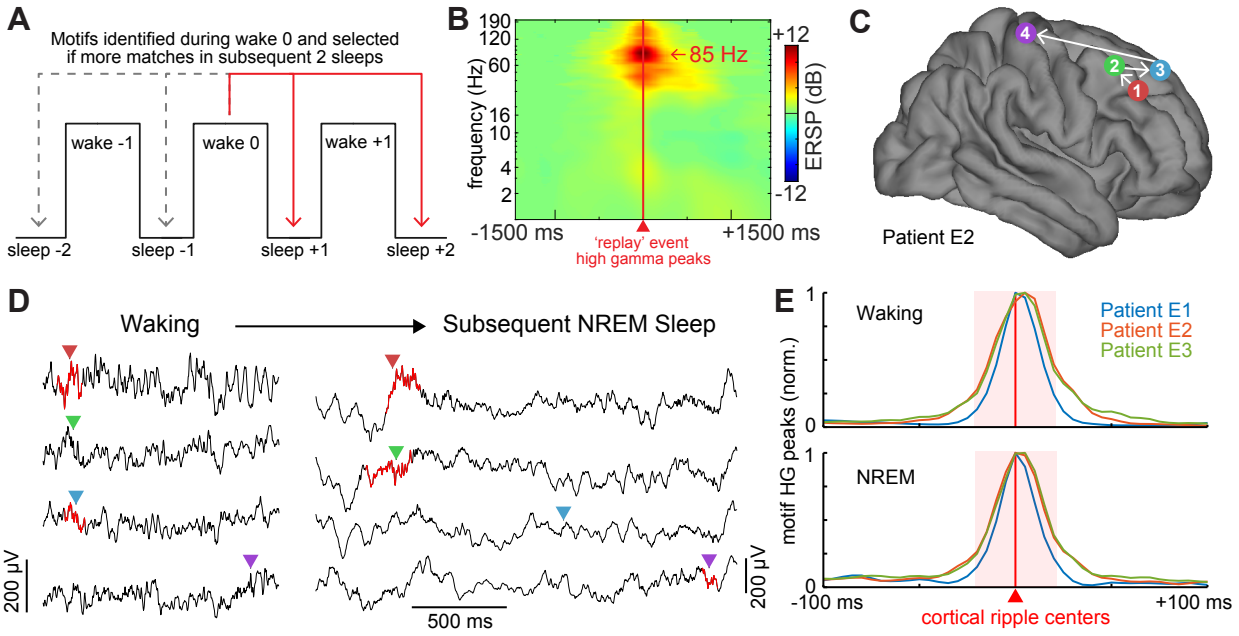

Fig. 2.6. Cortical ripples during NREM sleep are associated with spatiotemporal activity patterns that recur from previous waking. (**A**) Schematic for comparing the number of matching spatiotemporal patterns ('Motifs') of high gamma (70-190Hz) peaks from waking to preceding versus subsequent 2 sleeps (Jiang et al., 2017). All 3 patients had significantly more waking Motif matches to the subsequent compared to the preceding 2 sleeps (p<0.00001, two-sided binomial test, expected value=0.5). Events that were "exact matches" (i.e., common channels had same temporal order), which occurred more during the subsequent compared to the preceding 2 sleeps, were selected to test if they were related ripples. (**B**) Average time-frequency plot centered on Motif high gamma peaks shows focal activation in the ripple band. (**C-D**) Spatiotemporal high gamma peak sequence from an example Motif superimposed on a template brain (**C**) and as broadband LFP traces with ripples indicated in red (**D**). (**E**) Average Motif high gamma peak times plotted relative to local cortical ripple centers.

Discussion:

The current study provides the first comprehensive characterization of cortical ripples during waking and NREM sleep and provides the first evidence for their role in memory consolidation in humans. Using intracranial recordings, we report that human cortical ripples are widespread during NREM sleep in addition to waking. Basic ripple characteristics (occurrence rate, amplitude, oscillation frequency, duration, distribution across cortical areas) are very similar in cortex vs. hippocampus, and NREM sleep vs. waking. These characteristics are similar to those of rodents with two exceptions. First, the center frequency of human ripples is ~80Hz (Jiang et al., 2019a), whereas in rodents it is ~130Hz (Buzsaki, 2015). Conceivably, the larger human brain may require more time for cortico-cortical and

hippocampo-cortical integration than the rodent brain. The second apparent difference between humans and rodents is in cortical distribution. A previous rodent study found that cortical ripples were restricted to association cortex (Khodagholy et al., 2017), and consistent observations were reported in humans (Vaz et al., 2019). In contrast, we recorded cortical ripples in all areas sampled, with approximately equal occurrence rates that were lower in association areas as indicated by the positive correlation between occurrence rate and myelination index.

In contrast to the similarity of basic properties, we found that ripples in waking vs. NREM sleep occur within much different immediate physiological contexts. In NREM sleep, cortical ripples are strongly associated with local upstates, downstates, and sleep spindles. Characteristically, ripples occur on the upslope ~100ms before the peak of the upstate. Previous studies found that sleep spindles (Dickey et al., 2021a) and upstates (Csercsa et al., 2010) are associated with strong increases in local unit-firing, and we found that also to be the case for cortical ripples during NREM sleep. Hippocampal ripples during NREM sleep in previous studies were also found to often occur during local sharpwaves or spindles (Jiang et al., 2019a, 2019b; Jiang et al., 2019c; Staresina et al., 2015).

Of course, sleep spindles and down-to-upstates are characteristic of NREM sleep and would not be expected to occur with waking ripples. In addition, during waking, we found no other lower-frequency wave to be consistently associated with ripples. However, both cortical and hippocampal ripples occurred during greatly increased local >200Hz amplitude activity, a surrogate for unit-firing (Mukamel et al., 2005). Thus, the local contexts of both cortical and hippocampal ripples, in both NREM and waking, are sudden increases in local excitability lasting ~70ms. NREM and waking are different in that the depolarizing pulse is organized by endogenous sleep rhythms in NREM, but appears to be related to exogenous input, such as a retrieval cue, during waking.

Computational neural models and experimental studies have found that depolarizing pulses can induce oscillations from ~20-160Hz (Buzsaki, 2015; Buzsáki et al., 2012). Depolarization causes synchronous pyramidal cell firing, which is inhibited for a fixed time by recurrent inhibition from local basket cells. The pyramidal cells then fire again, resulting in Pyramidal Interneuron Network Gamma

(PING). As predicted by this model, we found strong ripple phase-modulation of putative pyramidal and interneuronal firing, with pyramids regularly preceding interneurons. Our findings are also consistent with PING supplemented by synchronized basket cell firing and mutual inhibition (ING; Interneuron Network Gamma) (Bartos et al., 2002). Definitive mechanistic demonstration would require experiments not currently possible *in vivo* in humans (Stark et al., 2014).

A critical aspect of hippocampal-dependent declarative memory is the linkage of novel constellations of elements encoded in widespread cortical locations. Thus, for replay to facilitate consolidation, it must re-activate spatiotemporal patterns distributed across the cortex. Previously, we showed that widespread spatiotemporal high gamma patterns from waking recur more during subsequent than preceding NREM sleep (Jiang et al., 2017). Here, we found that the activity peaks that form these patterns are tightly coupled with cortical ripples, consistent with ripples having a role in recurrence and potentially replay.

Consolidation requires plasticity as well as replay to increase the strength of the connections embodying the memory. The prime candidate is STDP, which occurs when pre- and post-synaptic cells fire in close temporal proximity (Feldman, 2012). We show here that local neurons are much more likely to fire at delays optimal for STDP during ripples than control periods, and that co-firing is organized beyond what would be expected by a general increase in neuron firing. A similar increase is also observed during spindles and upstates in humans (Dickey et al., 2021a). Since we also show that NREM cortical ripples are temporally coordinated with spindles and upstates, this supports a synergistic facilitation of plasticity.

In summary, the current study provides the first report of cortical ripples during sleep in humans. Cortical ripples during NREM sleep were found to have basic characteristics (duration, oscillation frequency, occurrence rate, and widespread cortical distribution) that are very similar to those of cortical ripples during waking as well as hippocampal ripples. Unit-firing during human cortical NREM ripples supported the mechanism proposed for rodent hippocampal ripples, based on pyramidal-interneuron feedback. Cortical ripples during NREM characteristically occurred after downstates, during spindles,

shortly before the peak of the upstate, an association and timing important for consolidation of memories during NREM sleep. Furthermore, NREM cortical ripples occurred at the peaks of spatiotemporal activation patterns that recurred from waking, and modulated paired cell-firing so that they fulfilled a basic requirement for STDP. Overall, these results are consistent with human cortical ripples playing a key role in consolidation during NREM sleep.

Methods:

Patient selection

Data from a total of 21 patients (13 female, 32±13 years old) with pharmaco-resistant epilepsy undergoing intracranial recording for seizure onset localization preceding surgical treatment were included in this study (STables 2.1,4,5). Patients whose stereoelectroencephalography (SEEG) recordings were analyzed were only included in the study if they had no prior brain surgery; background EEG (with the exception of epileptiform transients) in the normal range; and electrodes implanted in what was eventually found to be non-lesional, non-epileptogenic cortex, as well as non-lesional, non-epileptogenic hippocampus (such areas were suspected to be part of the focus prior to implantation, or were necessary to pass through to reach suspected epileptogenic areas). In 3 of these patients, previously collected electrocorticography (ECoG; subdural grids and strips) recordings were analyzed.

Furthermore, 3 of these patients undergoing electrocorticography and SEEG recording for the clinical purpose of seizure localization were also implanted with an intracranial microelectrode (Utah Array) into tissue that was suspected based on pre-surgical evaluation to be included within the region of the therapeutic resection. The implantation of the array did not affect clinical monitoring. In every case, the tissue into which the array was implanted was later resected in order to gain access to the surgical focus beneath. In all of these patients the electrode was determined not to be implanted in an epileptogenic zone, and no seizures originated from the region of the array in any of the patients.

Patients were excluded from the study if they had prior brain surgery or did not have non-lesioned hippocampal and cortical channels that were not involved in the early stage of the seizure discharge and

did not have frequent interictal activity or abnormal local field potentials. Based on these criteria, 21 were included in this study out of a total of 84. All patients gave fully informed written consent for their data to be used for research as monitored by the local Institutional Review Boards at Cleveland Clinic and Partners HealthCare (including Massachusetts General Hospital).

Intracranial recordings

Patients were implanted with intracranial electrodes for ~7 days with continuous recordings for seizure onset localization. SEEG and ECoG electrode implantation and targeting were made for purely clinical purposes. SEEG recordings (*N*=17 patients) were collected with a Nihon Kohden JE-120 amplifier at 1000Hz sampling (patients S1-17). Standard clinical electrodes were 0.8Mm diameter, with 10-16 2mm long contacts at 3.5-5mm pitch (~150 contacts/patient). ECoG recordings were collected at 500Hz (patient E1) or 512Hz (patients E2-3) using 128-channel clinical cable telemetry systems (STable 2.5).

Microelectrode recordings from 3 patients implanted with a Utah Array were also analyzed (STable 2.4). The Utah Array is a 10x10 microelectrode array with corners omitted and 400μm contact pitch (Fernández et al., 2014; Keller et al., 2010; Waziri et al., 2009). Each silicon probe is 1 or 1.5Mm long with a base of 35-75μm that tapers to 3-5μm. The probes are insulated except for the platinum-coated tip. Data were acquired at 30kHz (Blackrock Microsystems) with a 0.3-7.5KHz bandpass. Data were referenced with respect to a distant reference wire.

Electrophysiology pre-processing

Offline data preprocessing was performed in MATLAB 2019b and LFPs were inspected visually using the FieldTrip toolbox (Oostenveld et al., 2011). SEEG data were downsampled to 1000Hz with anti-aliasing and 60Hz notch filtered (zero-phase) with 60Hz harmonics up to 480 Hz. Transcortical contact pairs were identified using both anatomical location (using the pre-operative MRI aligned to the post-operative CT), and physiological properties (high amplitude, coherence and inversion of spontaneous

activity between contacts), and selected such that no 2 pairs shared a contact. All SEEG analyses were done using bipolar derivations of adjacent contacts in cortical or hippocampal gray matter in order to ensure that activity was locally generated (Mak-McCully et al., 2015).

Channel selection

Channels were excluded from the study if they were in lesioned tissue, involved in the early stages of the seizure discharge, had frequent interictal activity, or abnormal local field potentials. From the total 2129 bipolar channels (1202 left hemisphere) in the 17 SEEG patients (S1-17), 28 hippocampal (16 left hemisphere) and 273 transcortical (133 left hemisphere) bipolar channels were selected for the analyses (STable 2.1). Polarity was corrected for individual bipolar channels such that downstates were negative and upstates were positive. This was accomplished by ensuring that during NREM sleep, negative peaks were associated with decreased and positive peaks were associated with increased mean ±100ms 70-190Hz analytic amplitude, an index of cell-firing that is strongly modulated by downstates and upstates (Csercsa et al., 2010).

Electrode localization

Cortical surfaces were reconstructed from the pre-operative whole-head T1-weighted structural MR volume using the standard FreeSurfer recon-all pipeline (Fischl, 2012). Atlas-based automated parcellation (Fischl et al., 2004) was used to assign anatomical labels to regions of the cortical surface in the Destrieux (Destrieux et al., 2010) atlas. In addition, automated segmentation was used to assign anatomical labels to each voxel of the MR volume, including identifying voxels containing hippocampal subfields (Iglesias et al., 2015). In order to localize the SEEG contacts, the post-implant CT volume was registered to the MR volume, in standardized 1mm isotropic FreeSurfer space, using the general registration module (Johnson et al., 2007) in 3D Slicer (Fedorov et al., 2012). The position of each SEEG contact, in FreeSurfer coordinates, was then determined by manually annotating the centroids of electrode contact visualized in the co-registered CT volume. Each transcortical contact pair was assigned an

anatomical parcel from the atlas above by ascertaining the parcel identities of the surface vertex closest to the contact-pair midpoint. Subcortical contacts were assigned an anatomical label corresponding to the plurality of voxel segmentation labels within a 2-voxel radius. Transcortical contact pair locations were registered to the fsaverage template brain for visualization by spherical morphing (Fischl et al., 1999). To plot values on a template brain, channel means were averaged for each cortical region (with the two hemispheres combined) and then morphed onto a left hemisphere ico5 fsaverage template. Cortical regions are amalgamations of the Desikan parcels (Desikan et al., 2006) as specified in STable 2.6.

Myelination indices

A cortical area's hierarchical position is inversely proportional to its degree of myelination and this is indexed by the ratio between T1-weighted and T2-weighted MRI contrast (Glasser et al., 2011). Group average (N=1065 healthy young adults) myelination indices for each of the 360 parcels in the HCP-MMP1.0 atlas (Glasser et al., 2016) were previously obtained using the Human Connectome Project dataset (Rosen et al., 2021). These indices were then assigned to SEEG bipolar channels based on the HCP parcel in which they were located.

Time-frequency analyses

Average time-frequency plots of the ripple event-related spectral power (ERSP) were generated from the broadband LFP using EEGLAB (Delorme et al., 2004). Event-related spectral power was calculated from 1Hz to the Nyquist frequency (500Hz except for 250Hz in patient E1 and 256Hz in E2-3) with 1Hz resolution with ripple centers at t=0 by computing and averaging fast Fourier transforms with Hanning window tapering. Each 1Hz bin of the time-frequency matrix was normalized with respect to the mean power at -2000 to -1500ms and masked with two-tailed bootstrapped significance (N=200) with FDR correction and α=0.05 using -2000 to -1500ms as baseline.

Sleep and waking epoch selection

Epochs included in the study did not fall within at least 1 hour of a seizure and were not contaminated with frequent interictal spikes or artifacts. NREM sleep periods were selected from continuous overnight recordings where the delta (0.5-2Hz) analytic amplitude from the cortical channels was persistently increased (STable 2.1). Sleep epochs were confirmed by visual inspection to have normal appearing spindles, downstates, and upstates. Spindles, downstates, and upstates were also automatically detected (see "Sleep graphoelement detection"), and quantification of these events showed they had densities, amplitudes, and frequencies characteristic of NREM sleep (STable 2.2). Waking periods were selected from continuous daytime recordings that had persistently low cortical delta as well as high cortical alpha (8-12 Hz), beta (20-40Hz), and high gamma (70-190Hz) analytic amplitudes. When the data included electrooculography (EOG; *N*=15/17 SEEG patients), waking periods also required that the 0.5-40Hz analytic amplitude of the EOG trace was increased. Waking epochs were required to be separated from periods of increased delta by at least 30 minutes.

Ripple detection

The median center frequency of hippocampal ripples in 9 studies was ~85Hz in humans (Axmacher et al., 2008; Bragin et al., 1999; Clemens et al., 2007; Jiang et al., 2019b; Le Van Quyen et al., 2008; Norman et al., 2019; Staba et al., 2004; Staresina et al., 2015; Vaz et al., 2019), whereas in rodents, sharpwave-ripple frequency is ~120-140Hz. In humans, putative 80Hz hippocampal ripples have the same characteristic relation to sharpwaves, intra-hippocampal localization, modulation by sleep stage, and relation to cortical sleep waves as in rodents, and occur in hippocampi that have no signs of epileptic involvement. Furthermore, in rodent hippocampus the distinction between higher frequency gamma bursts and ripples is not always sharp, leading to the suggestion that for simplicity they both be referred to as 'ripples' (Stark et al., 2014), which we follow here.

Ripple detection was performed in the same way for all structures and states and was based on a previously described hippocampal ripple detection method (Jiang et al., 2019a, 2019b). Requirements for

inclusion and criteria for rejection were determined using an iterative process across patients, structures, and states. Data were bandpassed at 60-120Hz and the top 20% of 20ms moving root-mean-squared peaks were detected. It was further required that the maximum z-score of the analytic amplitude of the 70-100Hz bandpass was greater than 3 and that there were at least 3 distinct oscillation cycles in the 120Hz lowpassed signal, determined by shifting a 40ms window in increments of 5ms across ±50ms relative to the ripple midpoint and requiring that at least 1 window have at least 3 peaks. Adjacent ripples within 25ms were merged. Ripple centers were determined as the time of the maximum positive peak in the 70-100Hz bandpass. To reject epileptiform activities or artifacts, ripples were excluded if the absolute value of the z-score of the 100Hz highpass exceeded 7 or if they occurred within 2s of a ≥1mV/ms change in the LFP. Ripples were also excluded if they fell within ±500ms of putative interictal spikes, detected as described below. To exclude events that could be coupled across channels due to epileptiform activity, we excluded ripples that coincided with a putative interictal spike on any cortical or hippocampal SEEG or ECoG channel included in the analyses. Events in SEEG and ECoG recordings that had only one prominent cycle or deflection in the broadband LFP that manifested as multiple cycles above detection threshold in the 70-100Hz bandpass were excluded if the largest valley-to-peak or peak-to-valley absolute amplitude in the broadband LFP was 2.5 times greater than the third largest. For each channel, the mean ripple-locked LFP and mean ripple band were visually examined to confirm that there were multiple prominent cycles at ripple frequency (70-100Hz) and the mean time-frequency plot was examined to confirm there was a distinct increase in power within the 70-100Hz band. In addition, multiple individual ripples in the broadband LFP and 70-100Hz bandpass from each channel were visually examined to confirm that there were multiple cycles at ripple frequency without contamination by artifacts or epileptiform activity. Channels that did not contain ripples that meet these criteria were excluded from the study.

Interictal spike detection and rejection

Ripples and sleep graphoelements were excluded if they were within ±500ms from putative IIS detected as follows. A high frequency score was computed by smoothing the 70-190Hz analytic amplitude with a 20ms boxcar function and a spike template score was generated by computing the cross-covariance with a template interictal spike. The high frequency score was weighted by 13 and the spike score was weighted by 25, and an IIS was detected when these weighted sums exceeded 130. In each patient, detected IIS and intervening epochs were visually examined from hippocampal (when included) and cortical channels to confirm high detection sensitivity and specificity.

Sleep graphoelement detection

Downstates and upstates were detected as previously described (Jiang et al., 2019a, 2019b), where data from each channel were bandpassed from 0.1-4Hz (zero-phase shift) and consecutive zero crossings separated by 0.25-3s were selected. The top 10% amplitude peaks were selected and the polarity of each signal was inverted if needed so that downstates were negative and upstates were positive by confirming that the average analytic amplitude of the 70-190Hz bandpass ±100ms around peaks was greater for upstates than downstates.

Spindles were detected as previously described (Hagler et al., 2018), where data were bandpassed at 10-16Hz, then the absolute values were smoothed via convolution with a tapered 300ms Tukey window, and median values were subtracted from each channel. Data were normalized by the median absolute deviation and spindles were detected when peaks exceeded 1 for at least 400ms. Onsets and offsets were marked when these amplitudes fell below 1. Putative spindles that coincided with large increases in lower (4-8Hz) or higher (18-25Hz) band power were rejected to exclude broadband events as well as theta bursts, which may extend into the lower end of the spindle range (Gonzalez et al., 2018).

Ripple temporal relationships

Peri-cortical ripple time histograms of cortical graphoelements or Motif high gamma peaks on the same channel were computed. Gaussian smoothed (250ms window) event counts were found in 50ms bins for graphoelements within ±1500ms around cortical ripple centers at t=0. A null distribution was generated by shuffling the event times relative to the ripples at t=0 within this 3s window 200 times per channel. Pre-FDR p-values were computed by comparing the observed and null distributions within each bin over ±1000ms. These p-values were then FDR-corrected across bins and channels (Benjamini et al., 1995). A channel was considered to have a significant modulation if it had 3 or more consecutive bins with FDR-corrected p-values less than α=0.05. Whether events were leading or lagging cortical ripples at t=0 was computed for each channel with a two-sided binomial test with expected value of 0.5, using event counts in the 1000ms before vs. 1000ms after t=0. Plots had 50ms Gaussian smoothed event counts with 50ms bins.

Conditional probabilities of a ripple given the following graphoelements or their sequences were computed: downstate, spindle, upstate, downstate–spindle, and spindle–upstate. A ripple given a spindle (R | SS) was determined if the ripple center occurred during the spindle (average spindle duration was 634ms). A ripple was considered to precede an upstate or follow a downstate if the ripple center occurred 634ms before or after the peak of the upstate or downstate, respectively.

Unit detection, classification, quality, and isolation

Unit detection and classification was performed according to our published procedures (Chan et al., 2014; Dehghani et al., 2016; Dickey et al., 2021a; Eichenlaub et al., 2020; Le Van Quyen et al., 2016; Peyrache et al., 2012; Teleńczuk et al., 2017). Data were bandpassed at 300-3000Hz and putative unit spikes were detected when the filtered signal exceeded 5 times the estimated standard deviation of the background noise. Units were k-means clustered using the first three principal components of each spike. Overlaid spikes were examined visually and those with abnormal waveforms were excluded. Based on

their waveforms, firing rates, and autocorrelograms, action potentials were clustered as arising from putative pyramidal cells or interneurons. Putative pyramidal cells had spike rates of ~0.1-0.8Hz, long valley-to-peak and half width intervals, sharp autocorrelations, and bimodal inter-spike interval (ISI) distributions, reflecting a propensity to fire in bursts (STable 2.4). By contrast, putative interneurons had spike rates of ~1-5Hz, short valley-to-peak and half width intervals, broad autocorrelations, and a predominantly unimodal ISI distribution.

Single unit quality and isolation were confirmed according to previously established guidelines (Kamiński et al., 2020). Unit spikes were verified to well-exceed the noise floor based on large peak signal-to-noise ratios (SFig. 2.4A). Since the neuronal spiking refractory period is about 3ms, the percent of ISIs less than 3ms estimates the degree of single unit contamination by spikes from different units, which was very low among the units included in this study (SFig. 2.4B). Furthermore, single units detected on the same contact were highly separable according to their projection distances (Pouzat et al., 2002) (SFig. 2.4C). Lastly, temporal stability of unit spikes over time was confirmed based on consistency of the mean waveform shape and amplitude of each unit across recording quartiles.

Analyses of unit spiking during ripples

Unit spiking was analyzed with respect to local ripples detected on the same contact. Ripple phases of unit spikes were determined by finding the angle of the Hilbert transform of the 70-100Hz bandpassed signal (zero phase shift) at the times of the spikes. The circular mean ripple phase was determined for each unit (Berens, 2009). Phase analyses were only performed on units that had at least 30 spikes during local ripples. PY-PY and PY-IN unit pair co-firing within 5ms was assessed based on our previously published method (Dickey et al., 2021a). To evaluate co-firing when there was a ripple at either or both sites vs. baseline when there were no ripples occurring, we randomly selected non-ripple epochs matched in number and duration to the ripples but during which there were no ripples detected on either channel. Co-firing during ripples with observed vs. random spike times was computed by shuffling the spike times of each unit within the ripple epochs.

Cortical replay analyses

We performed new analyses on data from subjects 2-4 in Jiang et al. (2017) (STable 2.5). Analyses were performed on "Events" that were sequences of high gamma (70-190Hz) peaks identified during waking that recurred during the following NREM sleep, and which were considered 'exact matches,' such that all common channels had the same temporal order. Events consisting of high gamma peaks were identified as follows: outlier high gamma peaks were counted in 2s windows moving in 50ms increments. Events were identified when windows had local maxima of high gamma outlier peaks (minimum 4). When there were multiple high gamma peaks from the same channel during a given Event, only the median high gamma peak position across these channels was used.

Spatiotemporal Motifs were selected using methods from rat cortical electrophysiology studies. Events were grouped according to spatial distribution similarity in R with the packages Fast Hierarchical Clustering Routine (Müllner, 2013) and Dynamic Tree Cut (Langfelder et al., 2008) using Phi-coefficient-derived distance matrices (Miller et al., 2014) and Ward's method (Müllner, 2013). Motifs, which occurred during waking and NREM sleep, were identified by grouping waking Events based on high gamma peak order and then matching them to NREM Events. Temporal order similarity for waking Events in each cluster was computed using the matching index (MI) algorithm, which was implemented as previously described (Ji et al., 2007), except using high gamma peaks in place of spike train convolutions in MATLAB with custom scripts and in R with the TraMineR toolbox (Gabadinho et al., 2011), with an additional heuristic criterion that only the channels in common for each comparison were used to calculate MI. This metric of pattern similarity required that each channel had a unique position in the sequence since channel pair orders were compared with the MI.

Each cluster of spatially similar waking Events was subsequently divided into subclusters. Motifs that included 90% of a given subcluster's Events in their neighborhoods, defined as 20% of the maximum distance between two Events for a given subcluster, were selected. These were then matched with MI to the Events in NREM sleep, and each representative was associated with a certain number of replay frames (i.e., NREM Events that matched the waking Motif, or "Motif-Event matches") for each NREM period. If

multiple Motifs matched to the same NREM Event the number of replay frames associated with each waking Motif for that night was incremented by $1/N$ instead of 1, where N was the number of waking Motifs matched to the Event. Therefore, the total increments from any given Event was equal to 1 regardless of the number of matching Motifs as long as there was at least one match. The resulting replay frame numbers for each NREM period were then normalized by the total number of Events found in that NREM period. Waking motifs were required to match at least 2 Events.

Counts were made for Motifs that had more Motif-Event matches during the preceding than following NREM sleeps. This was compared to the number with the reverse pattern with a two-sided binomial test with an expected value of 0.5. Motifs were only included if their total number of NREM Event matches across all 4 nights (2 preceding waking, 2 following) exceeded Motif-wise thresholds established by matching preceding sleep and post sleep Event to the same Motifs with the channel order randomly shuffled 1000 times.

Statistical analyses

All statistical tests were evaluated with $\alpha=0.05$. *P*-values involving multiple comparisons were FDR-corrected (Benjamini et al., 1995) as specified in the text. Box-and-whisker plots show median, mean, and interquartile range, with whiskers indicating 1.5 × interquartile range, and with outliers omitted. Significance of linear correlations were assessed using the significance of the correlation coefficient when there were at least 10 data points.

Data and code availability

The de-identified raw data that support the findings of this study are available from the corresponding authors upon reasonable request provided that the data sharing agreement and patient consent permit that sharing. The code that support the findings of this study are available from the corresponding authors upon reasonable request.

Supplementary Information:

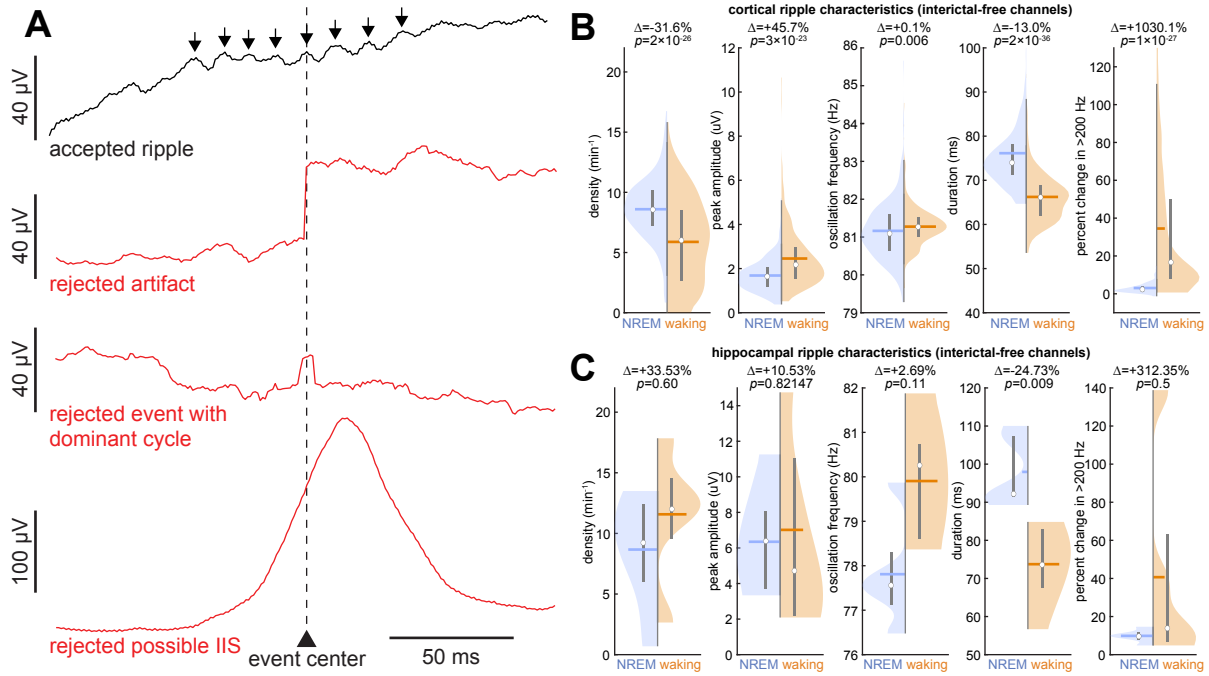

Supplementary Fig. 2.1. Ripple detection, event rejection, and characteristics of ripples detected on interictal-free channels. (**A**) Broadband LFP single sweeps show events that exceeded amplitude thresholds and were accepted for or rejected from the analyses: example accepted ripple with arrows indicating multiple 70-100Hz oscillation cycles, rejected artifact, rejected event with a single dominant cycle, and rejected possible IIS. Putative ripples within ±500ms of possible IIS detected on the same channel, as well as putative ripples coinciding with the sharp component of possible IIS on any cortical or hippocampal channel included in the analyses were rejected. (**B**) NREM sleep vs. waking cortical ripple density, peak 70-100Hz amplitude, frequency, duration, and percent change in mean >200Hz amplitude in interictal-free cortical channels (*N*=232 channels; patients S1-17). (**C**) Same as (**B**) except interictal-free hippocampal channels (*N*=5 channels; patients S4,6,9,17). IIS=interictal spike, LFP=local field potential.

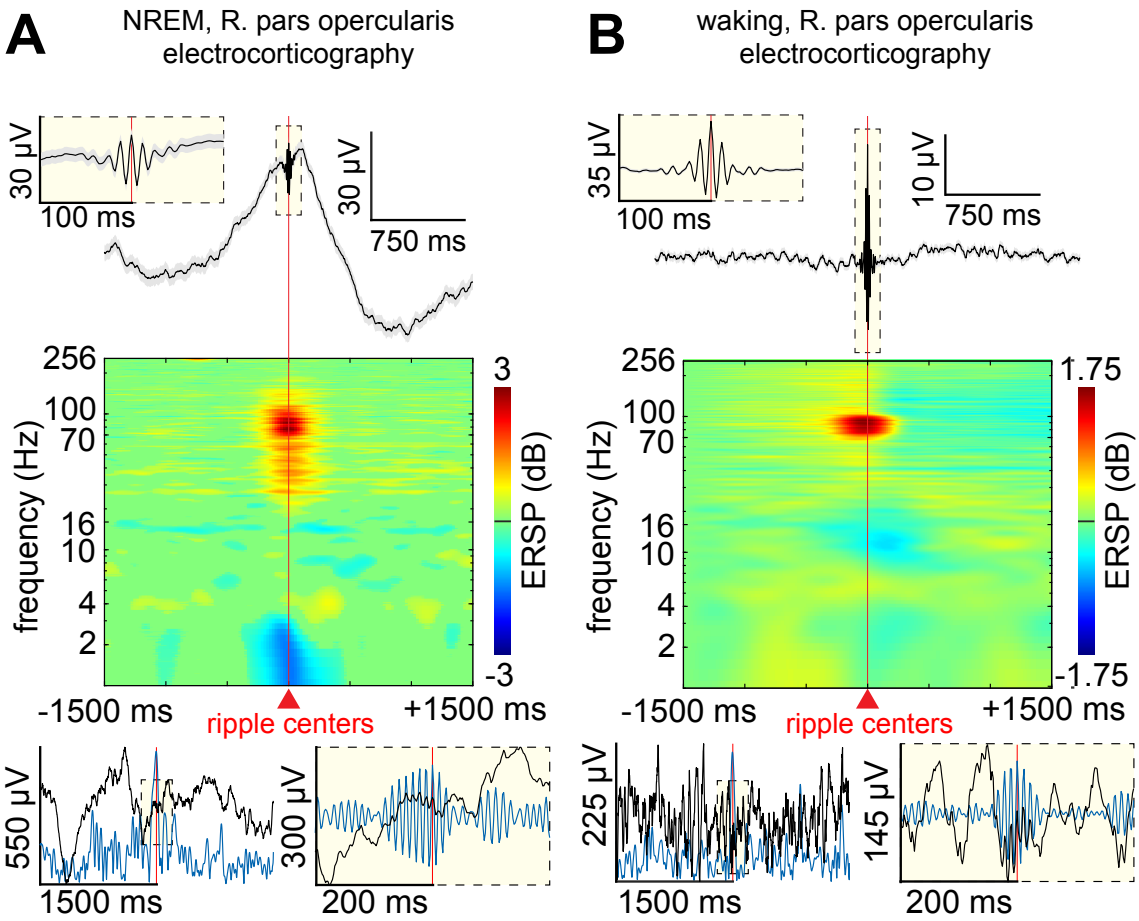

Supplementary Fig. 2.2. Cortical ripples detected in electrocorticography recordings. (**A-B**) Inferior frontal gyrus, pars opercularis ripples detected during NREM sleep (**A**) and waking (**B**) in an electrocorticography recording. Top shows average broadband LFP, middle shows average time-frequency, and bottom shows single trial example trace in broadband LFP (black) and 70-100Hz bandpass (blue, left–analytic amplitude, right–sweep).

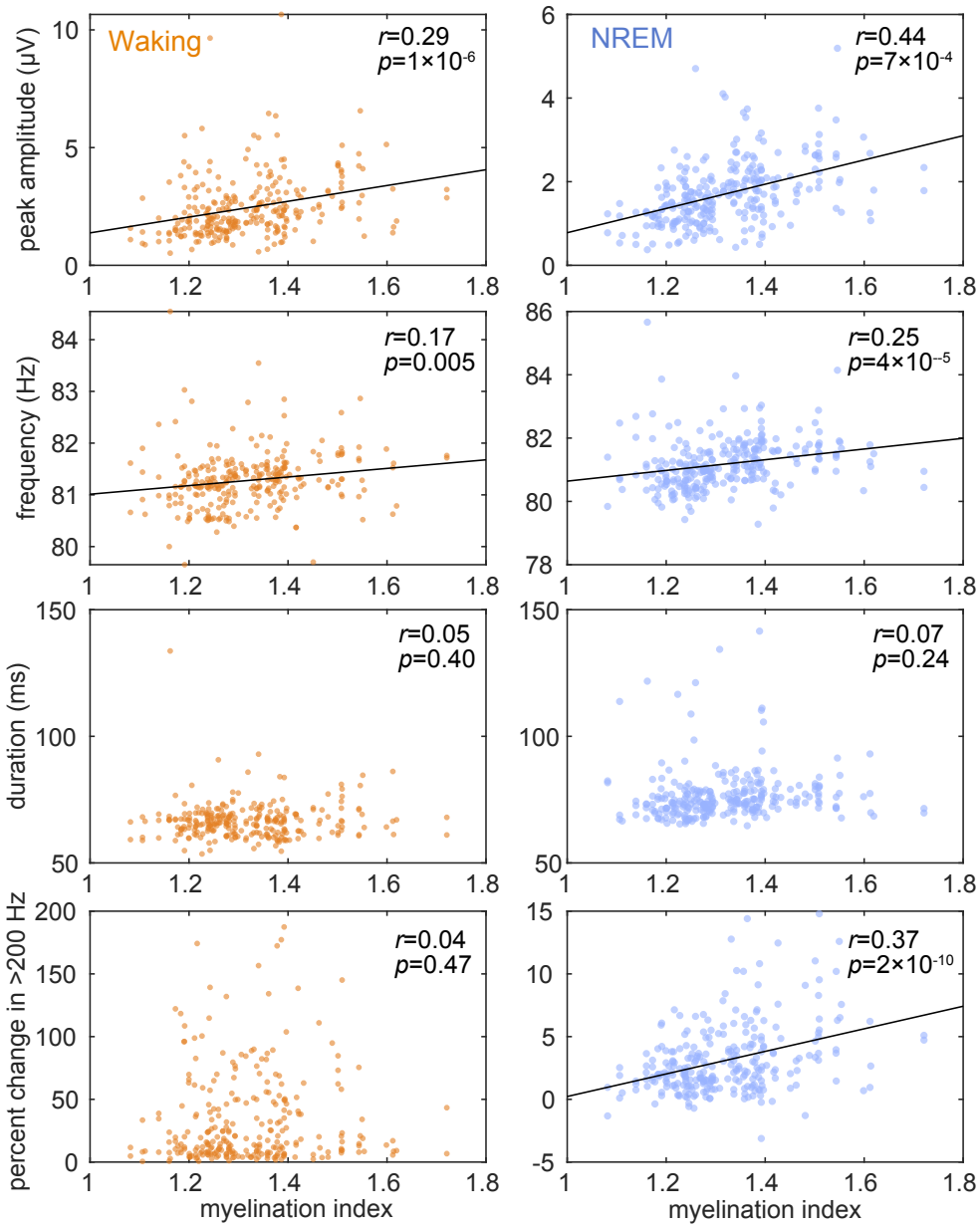

Supplementary Fig. 2.3. Cortical ripple characteristics versus myelination index. Cortical ripple peak amplitude, oscillation frequency, duration, and >200Hz amplitude modulation (*N*=273 channels). *P*-values report significance of the correlation coefficient. See Fig. 2.3G-H for density vs. myelination index.

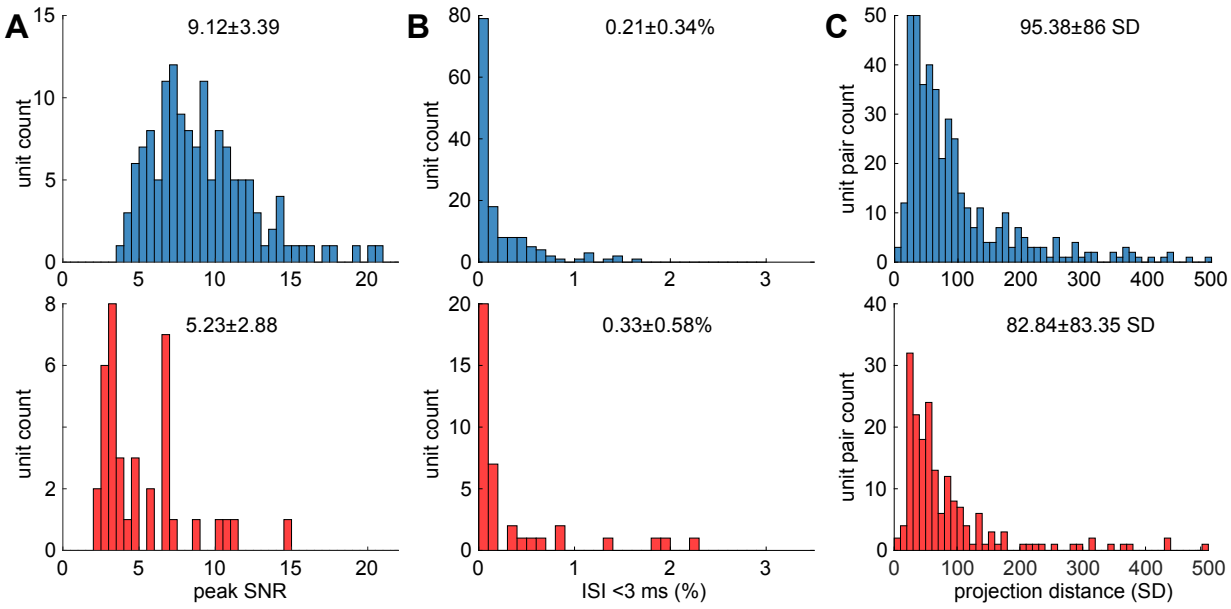

Supplementary Fig. 2.4. Single unit quality and isolation. (**A**) Peak SNR for PY (blue) and IN (red). (**B**) Percent of ISIs less than 3ms. (**C**) Pairwise projection distances in standard deviations between unit pairs detected by the same contact. Errors are standard deviations. IN=putative interneuron unit, ISI=inter-spike interval, PY=putative pyramidal unit, SNR=signal-to-noise ratio.

Supplementary Tables:

Supplementary Table 2.1. Stereoelectroencephalography patient demographics and data characteristics. Channels are the bipolar derivations included in the analyses. δ NREM / δ Waking reports the ratio of the mean of the delta (0.5-2Hz) analytic amplitude means across cortical channels during the NREM vs. waking epochs analyzed.

Patient	Age	Sex	Handedness	No. Cort. Ch.	No. Hipp. Ch.	NREM Dur. (hr)	Waking Dur. (hr)	δ NREM / δ Waking
S1	20	M	R	18 (L)	1 (L)	6.1	49.8	3.98
S2	58	F	R	22 (L)	2 (L)	23.7	23.8	2.35
S3	42	M	L	16 (3 L)	3 (2 L)	11.4	19.3	3.39
S4	18	F	L	15 (R)	2 (R)	2.7	2.2	3.02
S5	20	F	R	18 (7 L)	2 (R)	5.6	19.3	2.93
S6	22	M	LR	17 (L)	1 (L)	6.3	59.9	5.45
S7	30	F	R	13 (2 L)	1 (R)	20.5	76.7	4.46
S8	43	F	R	12 (L)	2 (L)	8.1	32.6	5.43
S9	16	M	R	16 (4 L)	1 (R)	16.3	4.8	2.50
S10	32	F	R	29 (3 L)	3 (1 L)	11.2	27.6	3.11
S11	21	F	L	8 (4 L)	3 (2 L)	16.0	52.6	3.04
S12	21	F	R	14 (13 L)	1 (L)	26.2	37.2	2.92
S13	29	F	R	15 (6 L)	2 (1 L)	8.6	24.6	3.75
S14	41	F	R	18 (R)	1 (R)	11.9	63.3	4.20
S15	24	M	R	21 (9 L)	1 (L)	11.8	11.6	3.27
S16	31	F	R	15 (7 L)	1 (L)	28.1	39.4	2.55
S17	21	M	R	6 (L)	1 (L)	11.3	18.9	1.41

Supplementary Table 2.2. Sleep graphoelement characteristics. Values are means and standard deviations across channels from SEEG patients S1-17.

	No. Events	Density (min^{-1})	Amplitude (μV)	Frequency (Hz)	Duration (ms)
Spindles	694168	3.0±3.0	9.7±4.5	12.4±0.7	633.5±67.2
Downstates	2649563	12.9±4.7	-79.1±56.6	N/A	N/A
Upstates	2922211	14.6±4.7	54.6±28.3	N/A	N/A

Supplementary Table 2.3. Sleep graphoelement–ripple coupling. Proportion of channels with significant peri-ripple modulations of graphoelements detected on the same channels within ±1000ms (e.g., Upstate | Cortical Ripple represents upstate peaks relative to cortical ripples at t=0; one-sided randomization test, 200 shuffles, 50ms non-overlapping bins, 3 consecutive bins with p<0.05 required for significance), and those with significant modulations that had significant sidedness preference around t=0 (p<0.05, one-sided binomial test, -1000 to -1ms vs. 1 to 1000ms, expected=0.5), and those with significant sidedness around 0 that had cortical ripples leading graphoelements (according to counts in -1000 to -1ms vs. 1 to 1000ms). In the calculations, upstate and downstate times were peaks and spindle times were onsets. *P*-values were FDR-corrected across channels and bins. See Fig. 2.4A-D for single sweep example and peri-ripple time histograms of cortical graphoelements and Fig. 2.4E for conditional probabilities.

Graphoelement | Ripple	Significant Modulation	Significant Sidedness	Cortical Ripple Leading
Downstate | Cortical Ripple	94.51% (258/273)	63.57% (164/258)	33.54% (56/164
Spindle | Cortical Ripple	29.3% (80/273)	73.75% (59/80)	28.81% (17/59)
Upstate | Cortical Ripple	95.24% (260/273)	83.85% (218/260)	86.70% (189/218)

Supplementary Table 2.4. Utah Array patient demographics and single unit characteristics. U1 and U3 are the same patients as E1 and E2, respectively (see Supplementary Table 2.5). Unit characteristic values are counts or means and standard deviations across units. Valley-to-peak amplitude, spike rate, valley-to-peak width, half-peak width, and bursting index were all significantly different between PY and IN (p<0.0001, two sample two-sided t-test). IN=putative interneuron unit, PY=putative pyramidal unit.

Utah Array Patient Demographics							
Patient	Age	Sex	Handedness	Implantation Location		Probe Length (mm)	NREM Duration (min)
U1 (E1)	51	F	R	Left middle temporal gyrus		1.0	200
U2	31	M	L	Left superior temporal gyrus		1.5	132
U3 (E2)	47	M	R	Right middle temporal gyrus		1.5	120
Single Unit Characteristics							
Unit Type	No. Units	No. Spikes	Valley-to-Peak Amplitude (μV)	Spike Rate (Hz)	Valley-to-Peak Width (ms)	Half-Peak Width (ms)	Bursting Index
PY	142	318386	89.57±59.46	0.19±0.17	0.49±0.06	0.61±0.04	0.05±0.03
IN	38	772769	42.26±26.11	1.73±1.72	0.30±0.05	0.35±0.05	0.01±0.02

Supplementary Table 2.5. Electrocorticography patient demographics. E1 and E2 are the same patients as U1 and U3, respectively (see Supplementary Table 2.4).

Patient	*Jiang et al. (2017)* Subject No.	Age	Sex	No. Ch.	Waking			NREM		
					Dur. (hr)	No. Events	Avg. High Gamma Peaks / Event	Dur. (hr)	No. Events	Avg. High Gamma Peaks / Event
E1 (U1)	2	51	F	44	6.59	5208	13.07	9.34	1251	9.47
E2 (U3)	3	47	M	65	14.88	5707	14.29	7.37	211	12.36
E3	4	54	F	75	9.83	16721	17.62	7.32	847	14.61

Supplementary Table 2.6. Relationships between cortical regions reported and Desikan parcels. First column lists the cortical regions described in this study, which are derived from an amalgamation of the cortical parcels from (Desikan et al., 2006) listed in the second column.

Cortical Region	Desikan Parcels
Orbitofrontal	frontal pole, lateral orbitofrontal, medial orbitofrontal, pars orbitalis
Prefrontal	caudal middle frontal, pars opercularis, pars triangularis, rostral middle frontal, superior frontal
Rolandic	paracentral, postcentral, precentral
Parietal	inferior parietal, superior parietal, supramarginal, precuneus
Occipital	cuneus, pericalcarine, lateral occipital
Superior Temporal / Insula	insula, superior temporal, transverse temporal
Lateral Temporal	banks of superior temporal gyrus, inferior temporal, middle temporal,
Ventral Temporal	entorhinal, fusiform, lingual, parahippocampal, temporal pole, isthmus cingulate
Cingulate	caudal anterior cingulate, rostral anterior cingulate, posterior cingulate

Chapter 2, in full, is a reprint of the material as it has been written in a manuscript submitted for publication: Dickey CW, Verzhbinsky IA, Jiang X, Rosen BQ, Kajfez S, Eskandar EN, Gonzalez-Martinez J, Cash SS, Halgren E. Cortical ripples provide the conditions for consolidation during NREM sleep in humans. Preprint available at *bioRxiv*. 2021. doi:10.1101/2021.05.11.443637.

Chapter 3: Widespread ripples synchronize human cortical activity during sleep, waking, and memory recall

Abstract:

Declarative memory encoding, consolidation, and retrieval require the integration of elements encoded in widespread cortical locations. The mechanism whereby such 'binding' of different components of mental events into unified representations occurs is unknown. The 'binding-by-synchrony' theory proposes that distributed encoding areas are bound by synchronous oscillations enabling enhanced communication. However, evidence for such oscillations is sparse. Brief high-frequency oscillations ('ripples') occur in the hippocampus and cortex, and help organize memory recall and consolidation. Here, using intracranial recordings in humans, we report that these ~70ms duration 80Hz ripples often couple (within ±500ms), co-occur (≥25ms overlap), and crucially, phase-lock (have consistent phase-lags) between widely distributed focal cortical locations during both sleep and waking, even between hemispheres. Cortical ripple co-occurrence is facilitated through activation across multiple sites, and phase-locking increases with more cortical sites co-rippling. Ripples in all cortical areas co-occur with hippocampal ripples but do not phase-lock with them, further suggesting that cortico-cortical synchrony is mediated by cortico-cortical connections. Ripple phase-lags vary across sleep nights, consistent with participation in different networks. During waking, we show that hippocampo-cortical and cortico-cortical co-ripples increase preceding successful delayed memory recall, when binding between the cue and response is essential. Ripples increase and phase-modulate unit-firing, and co-ripples increase high-frequency correlations between areas, suggesting synchronized unit-spiking facilitating information exchange. Co-occurrence, phase-synchrony, and high-frequency correlation are maintained with little decrement over very long distances (25cm). Hippocampo-cortico-cortical co-ripples appear to possess the essential properties necessary to support binding-by-synchrony during memory retrieval, and perhaps generally.

Introduction:

Ripples are brief high-frequency oscillations that have been well-studied in rodent hippocampus during non-rapid eye movement sleep (NREM), when they mark the replay of events from the previous waking period, and are critical for memory consolidation in the cortex (Buzsaki, 2015; Ego-Stengel et al., 2009; Maingret et al., 2016; Wilson et al., 1994). Recently, ripples were found in rat association cortex but not primary sensory or motor cortices during sleep, with increased coupling to hippocampal ripples in sleep following learning (Khodagholy et al., 2017). An earlier study reported ripples in waking and sleeping cat cortex, especially NREM (Grenier et al., 2001). In humans, cortical ripples have recently been identified during waking, and were more frequently found in lateral temporal than rolandic cortex. Hippocampal sharpwave-ripple occurrence and ripple coupling between parahippocampal gyrus and temporal association cortex are increased preceding memory recall in humans (Norman et al., 2019; Vaz et al., 2019), possibly facilitated through the replay of cortical neuron firing sequences established during encoding (Vaz et al., 2020). In rats, ripples co-occur between hippocampus and ~1mm^2 of parietal cortex in sleep following learning (Khodagholy et al., 2017), in mice, ripples propagate from the hippocampus to retrosplenial cortex (Nitzan et al., 2020), and in cats, ripple co-occurrence is reportedly limited to short distances (Grenier et al., 2001).

We recently reported, using human intracranial recordings, that ~70ms long ~80Hz ripples are ubiquitous in all regions of the cortex during NREM as well as waking (Dickey et al., 2021b). During waking, cortical ripples occur on local high frequency activity peaks. During sleep, cortical ripples occur, often during spindles, and typically on the down-to-upstate transition, with unit-firing patterns consistent with generation by pyramidal-interneuron feedback. We found that cortical ripples mark the recurrence of spatiotemporal activity patterns from preceding waking, and they group co-firing within the window of spike-timing-dependent plasticity. These findings are consistent with cortical ripples contributing to memory consolidation during NREM in humans.

While there is thus an emerging appreciation that hippocampal and cortical ripples have an important role in memory in humans and rodents, nothing is known of the network properties of cortical ripples. Specifically, it is not known if ripples co-occur or phase-synchronize between cortical sites, and if so, whether this is affected by distance or correlated with the reconstruction of declarative memories. These would be critical properties for cortical ripples to participate in the binding of different elements of memories that are represented in disparate cortical areas, the essence of hippocampus-dependent memory (Squire, 1992).

The binding of disparate elements of a memory is a specific case of a more general problem of how the various contents of a mental event are united into a single experience. Most often addressed is how different visual qualities of an object (e.g., color, shape, location, texture) are associated with each other (Treisman, 1999), but the 'binding problem' generalizes to how the contents of awareness are unified in a single stream of consciousness (Revonsuo et al., 1999). Modern accounts often rely on hierarchical and multimodal convergence. However, cortical processing is distributed, and it would be difficult to represent the combinatorial possibilities contained in all potential experiences with convergence, leading to the suggestion that temporal synchrony binds cortical areas (von der Malsburg, 1999). This hypothesis was first supported by phase-locked unit-firing and local field potentials (LFP) at 40-60Hz evoked by simple visual stimuli in the anesthetized cat primary visual cortex at distances <7mm (Gray et al., 1989). Although some further studies found similar results in other cortical areas, behaviors and species, as would be expected under the binding-by-synchrony hypothesis (Fries, 2009; Uhlhaas et al., 2009), others have been less successful (Shadlen et al., 1999). Synchronous high gamma oscillations have also been criticized as providing no mechanism for neuronal interaction beyond generic activation (Merker, 2013; Shadlen et al., 1999).

Here, using human intracranial stereoelectroencephalography (SEEG) recordings, we find that ripples co-occur, and remarkably, phase-synchronize across all lobes and between both hemispheres, with little decrement, even at long distances. Furthermore, ripple co-occurrence is enhanced between cortical sites as well as between the cortex and hippocampus preceding successful delayed recall. Co-rippling was

progressively above that expected as it involved a larger proportion of sites, and this led to progressively stronger phase-locking. Single-unit firing increased during, and phase-locked to, cortical ripples, providing a basic requirement for ripples to enhance communication via gain-modulation and coincidence detection. Enhanced communication was supported by our finding of increased high-frequency correlation between even distant co-rippling regions. These characteristics suggest that distributed, phase-locked cortical ripples possess the properties that may allow them to help integrate different components of a memory. More generally, ripples may help to 'bind' different aspects of a mental event encoded in widespread cortical areas into a coherent representation.

Results:

Ripple detection during NREM and waking

Ripples were detected using intracranial cortical and hippocampal recordings in 17 patients (STable 3.1) undergoing monitoring to localize seizure foci during NREM and waking. Bipolar contact derivations were used to measure local field potentials (LFP). Ripples were detected only on channels in non-lesional, non-epileptogenic areas. Ripples were required to have 3 or more cycles of increased 70-100Hz amplitude that did not contain epileptiform activity or artifacts. Ripples were also required not to occur at the time of putative interictal spikes detected on any other channel to exclude events that could be spuriously coupled due to epileptiform activity.

Cortical ripples were detected in all lobes of both hemispheres during NREM and waking (Fig. 3.1A-B). Cortical and hippocampal ripples were consistently ~70-85ms long ~80Hz oscillations (Fig. 3.1A-B). Specifically, cortical ripples during NREM had an average and standard deviation density of 8.36±2.69min^{-1}, amplitude of 1.70±0.75μV, duration of 76.47±10.14ms, and frequency of 81.18±0.78Hz, and during waking had a density of 5.79±3.41min^{-1}, amplitude of 2.44±1.31μV, duration of 66.59±7.17ms, and frequency of 81.28±0.55Hz, with a strong association of high-frequency (>200Hz) amplitude during waking ripples (Fig. 3.1C-D; *N*=273 channels). Hippocampal ripples during NREM had an average and standard deviation density of 6.95±4.80min^{-1}, amplitude of 5.76±2.58μV, duration of

87.46±9.05ms, and frequency of 78.50±1.34Hz, and during waking had a density of 7.40±5.47min^{-1}, amplitude of 6.00±3.16μV, duration of 69.74±7.91ms, and frequency of 80.29±0.85Hz (*N*=28 channels). A standard deviation of <1Hz in ripple frequency in all circumstances suggests the possibility that local channel and network properties underlie a consistent resonant frequency.

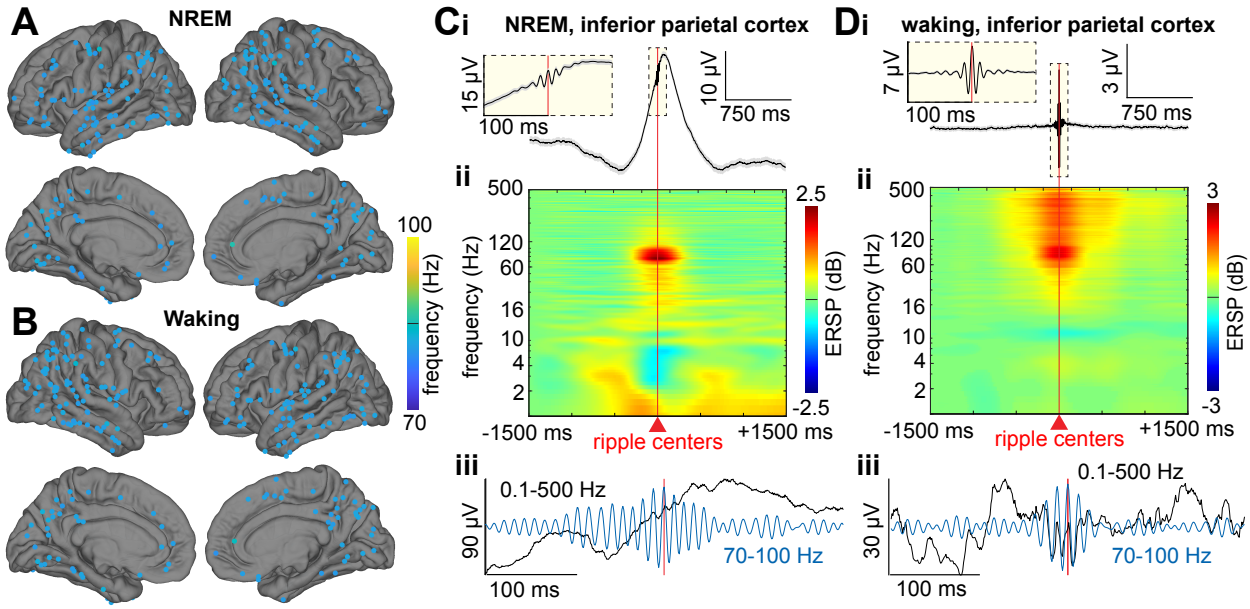

Fig. 3.1. Cortical ripple generation during NREM and waking. (**A**) Cortical ripple oscillation frequencies across the cortex during NREM. Each marker depicts the average ripple frequency in a given channel (*N*=273 channels from SEEG patients S1-17). Color range spans the ripple band used for detection (70-100Hz). Note the highly consistent frequencies across lobes, between hemispheres, and between NREM and waking. (**B**) Same as (A) except for waking. (**C**) Average broadband LFP (**i**) and time-frequency (**ii**) across cortical ripples, and example broadband ripple (**iii**) unfiltered single sweeps (black), and 70-100Hz bandpass (blue) during NREM. Recording is from a channel in inferior parietal cortex. (**D**) Same as (A) except inferior parietal cortex ripples during waking. Error shows SEM. SEEG=stereoelectroencephalgography, bipolar recordings.

Cortical ripples couple and co-occur across widespread regions

We hypothesized that ripples couple (defined here as occurrence within ±500ms) and even more importantly co-occur (≥25ms overlap) between cortical sites, which would be crucial for widespread information integration. We discovered that cortical ripples frequently and strongly couple with each other during both NREM (*N*=4487/4550 significant channel pairs, randomization test, post-FDR $p<0.05$) and waking (*N*=4478/4550), between all cortical areas sampled (Fig. 3.2A, Table 3.1), including between

hemispheres. The proportion of cortico-cortical channel pairs that were significantly coupled during NREM (98.6%) was not significantly different than that proportion during waking (98.4%; p=0.44, χ^2=0.61, df=1).

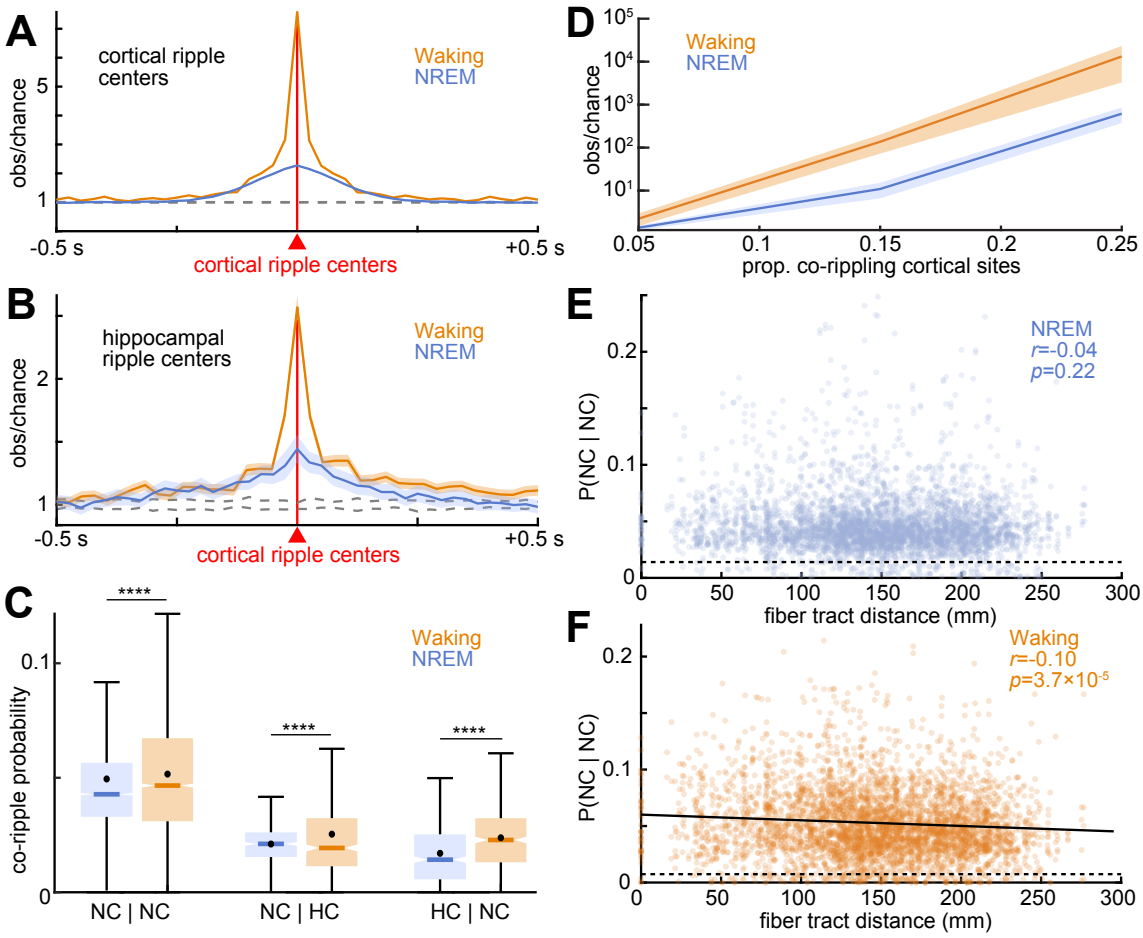

Fig. 3.2. Cortico-cortical and hippocampo-cortical ripples couple and co-occur during waking and NREM. (**A**) Cortico-cortical ripple time delays reveal strong coupling (occurring within 500ms of each other without necessarily overlapping) between nearly all sites during NREM (N=4487/4550 significant channel pairs) and waking (N=4478/4550; post-FDR p<0.05, randomization test). Dashed lines show 99% confidence interval of the null distribution (200 shuffles/channel pair). (**B**) Same as (A) except hippocampal ripple coupling with cortical ripples (NREM: N=133/461; waking: N=401/461). (**C**) Conditional co-occurrence probabilities of cortico-cortical and hippocampo-cortical ripples overlapping for at least 25ms (i.e., probability of a ripple in a particular channel given a ripple in another particular channel) are greater during waking than NREM (****post-FDR p<0.0001, two-sided paired t-test). (**D**) Observed over chance cortical ripple co-occurrence (logarithmic scale) increases with the number of sites co-rippling. (**E**) Cortical ripple co-occurrence probabilities during NREM are stable with increasing intervening fiber tract distance (linear mixed-effects with subject as random effect). Dashed line indicates chance. (**F**) Same as (E) except for waking. Fit is linear least-squares regression. Error shows SEM.

Table 3.1. Cortical ripple coupling with cortical or hippocampal ripples: frequency and order. *Significant Modulation:* Proportion of channel pairs with a significant increase in the conditional probability of a ripple occurring in the first channel given that one occurred within ±500ms in the second (e.g., Hipp-R | Cort-R refers to hippocampal ripples occurring within ±500ms relative to cortical ripples at t=0; one-sided randomization test, 200 shuffles, 25ms non-overlapping bins, 3 consecutive bins with p<0.05 required for significance). During NREM, conditional probabilities are shown separately for those hippocampal ripples associated with sharpwaves (Hipp-SWR) and sleep spindles (Hipp-SSR) as well as all ripples (Hipp-R). *Significant Sidedness:* Those with significant modulations that had significant sidedness preference around t=0 (p<0.05, two-sided binomial test, expected=0.5, -500 to -1ms vs. 1 to 500ms). *Cortical Ripple Leading:* Those with significant sidedness around 0 that had cortical ripples leading (according to counts within -500 to -1ms vs. 1 to 500ms). During NREM, Hipp-R and Hipp-SWR led Cort-R, and during waking, Cort-R led Hipp-R (*=p<0.05, two-sided binomial test, expected value=0.5), resulting in a significant preference for cortical ripples to lead hippocampal ripples in waking vs. NREM (p<0.00001, χ^2=51.59, df=1).

Ripple | Ripple	Significant Modulation	Significant Sidedness	Cortical Ripple Leading
	NREM		
Cort-R | Cort-R	98.62% (4487/4550)	3.50% (157/4487)	N/A
Hipp-R | Cort-R	28.85% (133/461)	31.58% (42/133)	33.33% (14/42)*
Cort-R | Hipp-R	29.28% (135/461)	31.11% (42/135)	33.33% (14/42)*
Hipp-SWR | Cort-R	19.74% (91/461)	45.05% (41/91)	24.39% (10/41)*
Cort-R | Hipp-SWR	20.61% (95/461)	44.21% (42/95)	21.43% (9/42)*
Hipp-SSR | Cort-R	12.15% (56/461)	17.85% (10/56)	50% (5/10)
Cort-R | Hipp-SSR	11.71% (54/461)	22.22% (11/54)	41.67% (5/12)
	Waking		
Cort-R | Cort-R	98.42% (4478/4550)	8.13% (364/4478)	N/A
Hipp-R | Cort-R	86.98% (401/461)	22.44% (90/401)	84.44% (76/90)*
Cort-R | Hipp-R	87.42% (403/461)	22.33% (90/403)	84.44% (76/90)*

Critically, we found that short latency coupling led to co-occurrence (≥25ms overlap) of these ~70ms long ripples, with slightly but significantly higher probabilities during waking than NREM (Fig. 3.2C). The percent of cortico-cortical channel pairs with significant ripple co-occurrence was very high and nearly equal during NREM (N=2218/2275, 97.5%) vs. waking (N=2225/2275, 97.8%). Thus, nearly all cortico-cortical channel-pairs couple and co-occur above chance during both sleep and waking.

Hippocampal and cortical ripples couple and co-occur, especially during waking, but at lower rates than cortico-cortical

As previously found (Vaz et al., 2019), ripples in many hippocampo-cortical channel-pairs were also significantly coupled (Fig. 3.2B, Table 3.1) during both NREM (N=133/461) and waking (N=401/461), but at a significantly lower rate than cortico-cortical pairs in both states (NREM: $p<0.00001$, $\chi^2=2832.0$, df=1; Waking: $p<0.00001$, $\chi^2=213.3$, df=1). Unlike cortico-cortical pairs, the proportion of significant hippocampo-cortical pairs was higher during waking (87.0%) than NREM (28.9%, $p<0.00001$, $\chi^2=319.61$, df=1). Of note, these findings of cortico-cortical and hippocampo-cortical couplings were maintained when only cortical and hippocampal channels that were free of interictal spikes at any time were analyzed (STable 3.2).

Overlapping co-occurrence of human ripples between cortex and hippocampus do not appear to have been studied *per se*, but would also be expected to occur given their coupling. Indeed, we found significant co-occurrence of ripples in 81.1% (N=374/461) of hippocampo-cortical site-pairs during waking, and 34.7% (N=160/461) during NREM. Higher hippocampo-cortical co-occurrence during waking compared to NREM was significant ($p<0.00001$, $\chi^2=203.8$, df=1). In addition, these percentages for hippocampo-cortical co-occurrences (81.1% waking; 34.7% NREM) are significantly lower than for cortico-cortical site-pairs (97.5% waking; 97.8% NREM) (NREM: $p<0.00001$, $\chi^2=1328.8$, df=1; waking: $p<0.00001$, $\chi^2=1250.1$, df=1*).* Thus, ripples in hippocampal and cortical sites do couple and co-occur, but at a substantially lower rate than between cortical sites.

Hippocampal ripples lead cortical during NREM and *vice versa* during waking

The order of rippling in the hippocampus versus cortex is of interest, given the hypothesized transfer of information from hippocampus to cortex during sleep consolidation, and from cortex to hippocampus during waking memory encoding. During NREM, 31.58% (42/133) of the hippocampo-cortical pairs that were significantly coupled had a significant sidedness preference, where one channel's ripples led the other's (Table 3.1; post-FDR $p<0.05$, two-sided binomial test, expected value=0.05).

Among these significant pairs, hippocampal ripples led cortical ripples in 66.7% (28/42). By contrast, during waking, 22.4% (90/401) of the pairs with significant coupling showed a sided preference, with cortical ripples leading hippocampal ripples in 84.4% (76/90). This overall preference for hippocampal ripples to lead cortical ripples during NREM, and *vice versa* during waking was highly significant (p=4.3×10^{-9}, χ^2=34.5, df=1).

In the above results, we considered all ripples that met our quality criteria. However, studies of ripples in rodent hippocampus commonly focus on ripples that occur on a slower sharpwave (Buzsaki, 2015). In humans, anterior hippocampal ripples during NREM typically occur on sharpwaves (Jiang et al., 2019a), whereas posterior hippocampal ripples are often associated with spindles (Jiang et al., 2019b). Sharpwave-ripples have stronger associations with sleep waves in prefrontal cortex areas supporting contextual aspects of episodic memory, whereas spindle-ripples can phase-lock with spindles in parietal areas supporting detailed autobiographical recollection. Here, we found that hippocampal sharpwave-ripples significantly preceded cortical ripples by ~250ms (SFig. 3.1A; p=0.002, two-sided binomial test, expected value=0.5), whereas spindle-ripples were concurrent (SFig. 3.1B; p=1). These results reinforce a previous suggestion that ripples make sequential contributions to consolidation (Jiang et al., 2019b). Overall, as predicted by models of hippocampo-cortical interaction for memory, hippocampal ripples usually lead cortical during sleep, and cortical usually lead hippocampal during waking.

Cortical ripple co-occurrence is facilitated through activation across multiple sites

In each patient, we found that when two of the sampled cortical sites co-rippled, one or more additional sites could also be co-rippling (SFig. 3.2). To test if two cortical sites co-rippling made it more likely for other sites also to co-ripple, we computed a χ^2 test of proportions for all possible groups of three cortical channels under the null hypothesis that the co-occurrence of channel A and B has no relation to the co-occurrence of A and C. We found that two sites co-rippling often made it more likely for another site to co-ripple, with an average of 14.1% of significant channel-triplets across patients during NREM

and 38.8% during waking (patient specific results reported in STable 3.3, χ^2 test of proportions, FDR-corrected *p*-values across channel-triplets within subjects).

In further support that co-rippling is facilitated through activation across multiple sites, we found that the level relative to chance for multiple locations to co-ripple increased with the number of locations co-rippling (>2) (Fig. 3.2D). The increase was pronounced, such that the observed probability relative to baseline of 25% of all channels was ~10^4 during waking and ~5×10^3 during NREM. Thus, co-rippling appears to beget more co-rippling, suggesting the possibility of self-reinforcing spread.

Cortical ripples co-occur robustly across distance

Binding by ripples requires that they co-occur across widespread cortical areas. We compared conditional probabilities of cortico-cortical ripple co-occurrences (i.e., the probability of a ripple in one cortical site given a ripple in another cortical site, requiring ≥25ms overlap) against white-matter streamline distances between cortical sites. Streamline distances were computed using the 360 parcels of the HCP-MMP1.0 atlas (Glasser et al., 2016), as determined by probabilistic diffusion MRI tractography (Behrens et al., 2007), and are population averages from (Rosen et al., 2021). We found that cortico-cortical co-rippling probability did not decrease with fiber tract distance during NREM (Fig. 3.2E, r=-0.04, p=0.22, linear mixed-effects), but rather was maintained up to 25cm separation, across lobes and between hemispheres. During waking, co-rippling probabilities were also maintained across this distance range, albeit with a weak but significant negative linear relationship (Fig. 3.2F, r=-0.10, p=3.7×10^{-5}).

Ripples in all cortical areas co-occur with hippocampal ripples

It was previously reported that ripple coupling occurs between the parahippocampal gyrus and 16.4% of lateral temporal electrodes but only 3.3% of Rolandic (Vaz et al., 2019). This seems to be consistent with the anatomical location of the hippocampus at the apex of the cortical hierarchy (Felleman et al., 1991). However, we found that hippocampal ripples co-occurred with ripples in all cortical areas at approximately equal rates in both NREM and waking. Taking the myelination index as a

measure of the location of different areas on the sensorimotor to association cortex hierarchy, in which association areas are less myelinated (Glasser et al., 2011), we found a weak but significant effect during NREM but not waking. During NREM, hippocampo-cortical co-occurrence was positively correlated (r=0.15) with myelination (p=0.01), indicating that hippocampal ripples are slightly more likely to co-occur with ripples in primary cortical areas (SFig. 3.3). Possibly, even if the hippocampus is more directly connected with high-level cortices, it indirectly co-ripples with all cortical areas via the dense cortico-cortical co-rippling networks described above.

Cortico-cortical and hippocampo-cortical ripple co-occurrences precede recall

If ripples in different cortical regions bind the elements of a memory, it would be expected that cortical ripples co-occur preceding cued recall, which requires that those elements be co-activated. To test this hypothesis, we analyzed paired-associates memory task data from 5 SEEG patients (Fig. 3.3A, STables 3.1,4). Preceding delayed cued recall, there was a significant increase in cortical ripple occurrence ($p=1\times10^{-11}$) of 330% of chance, and an even greater increase in cortico-cortical ripple co-occurrence of 758% of chance (p=0.0004, linear mixed-effects; Fig. 3.3B-E). Furthermore, cortical ripple occurrence (p=0.002) and cortico-cortical (p=0.002) and hippocampo-cortical (p=0.008) ripple co-occurrence modulations were greater preceding delayed vs. immediate recall, which shared the same stimuli and responses. Finally, cortico-cortical (p=0.04) and hippocampo-cortical (p=0.004) co-rippling was enhanced preceding correct vs. incorrect delayed recall, which was not the case for cortical (p=0.08) or hippocampal (p=0.94) ripples generally. Delayed but not immediate recall of paired associates is severely impaired by hippocampal damage (Squire, 1992). These data demonstrate increased co-rippling between cortical sites and between the hippocampus and cortex during hippocampal-dependent retrieval of novel combinations of previously unrelated items. This finding supports the hypothesis that hippocampo-cortical and cortico-cortical co-rippling may contribute to the reconstruction of declarative memories in humans.

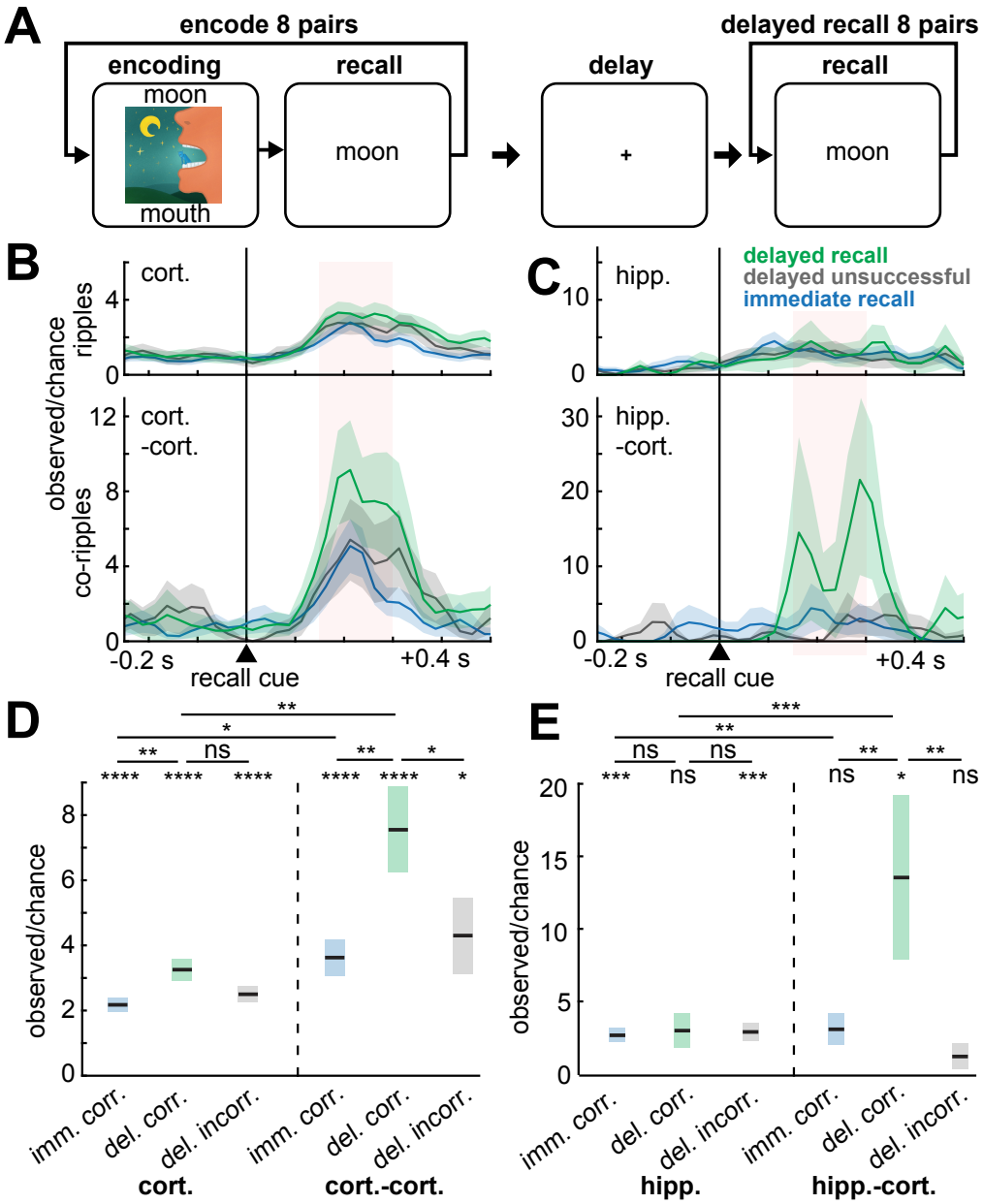

Fig. 3.3. Cortico-cortical and hippocampo-cortical ripple co-occurrences increase preceding recall. (**A**) Schematic of paired-associates memory task. Patients learned word pair associations and were subsequently cued with the first word to recall the second immediately following learning and then after a ~60s delay with distraction. (**B**) Cortical and cortico-cortical co-rippling increases following the stimulus cue triggering recall (delayed *N*=365 trials, immediate *N*=698 trials, patients S18-22). (**C**) Same as (B) except for hippocampal ripples and hippocampo-cortical co-ripples (delayed *N*=90 trials, immediate *N*=304 trials, patients S19,22). **(D-E)** Quantification of (B-C) during the shaded 150-300ms interval following stimulus cue onset preceding correct recall in the immediate or delayed condition, or incorrect recall (no attempt or incorrect response) in the delayed condition. Note that cortico-cortical and hippocampo-cortical co-occurrences preceding correct delayed recall have the greatest increases. Errors show SEM. Post-FDR *p<0.05, **p<0.01, ***p<0.001, ****p<0.0001, linear mixed-effects models.

Cortical ripples phase-lock across widespread regions

Phase-locked oscillations in widespread locations have been hypothesized to underlie integration ('binding') of different components of events across the cortical surface. For each channel-pair, we calculated the phase-locking value (PLV), a measure of the consistency of 70-100Hz phases between sites, independent of amplitude (Lachaux et al., 1999), across all of their co-ripple events in either NREM or waking. We found significant PLV of co-occurring ripples between all sampled cortical regions, including between hemispheres, in both states (Fig. 3.4A-C). Channel-pairs with significant PLV were more frequent during NREM than waking (Fig. 3.4C, STable 3.5; post-FDR $p<0.05$, randomization test; non-significant results in SFig. 3.4A-B). An example of consistent phase between two cortical locations across two co-ripples is shown in Fig. 3.4A. For each channel-pair, PLV was measured at each latency relative to the center of their co-ripple (Fig. 3.4B), and these time-courses were averaged across all significant channel-pairs (Fig. 3.4C). The increased PLV lasted for the entire period when the sites were co-rippling, and arose abruptly from baseline. PLV time-course was remarkably similar across channel-pairs. During sleep 2106/2275 cortico-cortical channel pairs had more than 40 co-occurring ripples, required for a reliable PLV estimate. Of these, 26.3% (554/2106) had significant PLV modulations. During waking, 1939/2275 had more than 40 co-occurring ripples, and 13.9% (269/1939) of these had significant PLV modulations (STable 3.5). In summary, distant pairs of sites throughout the cortex were found to have consistent phases during co-ripples in both NREM and waking.

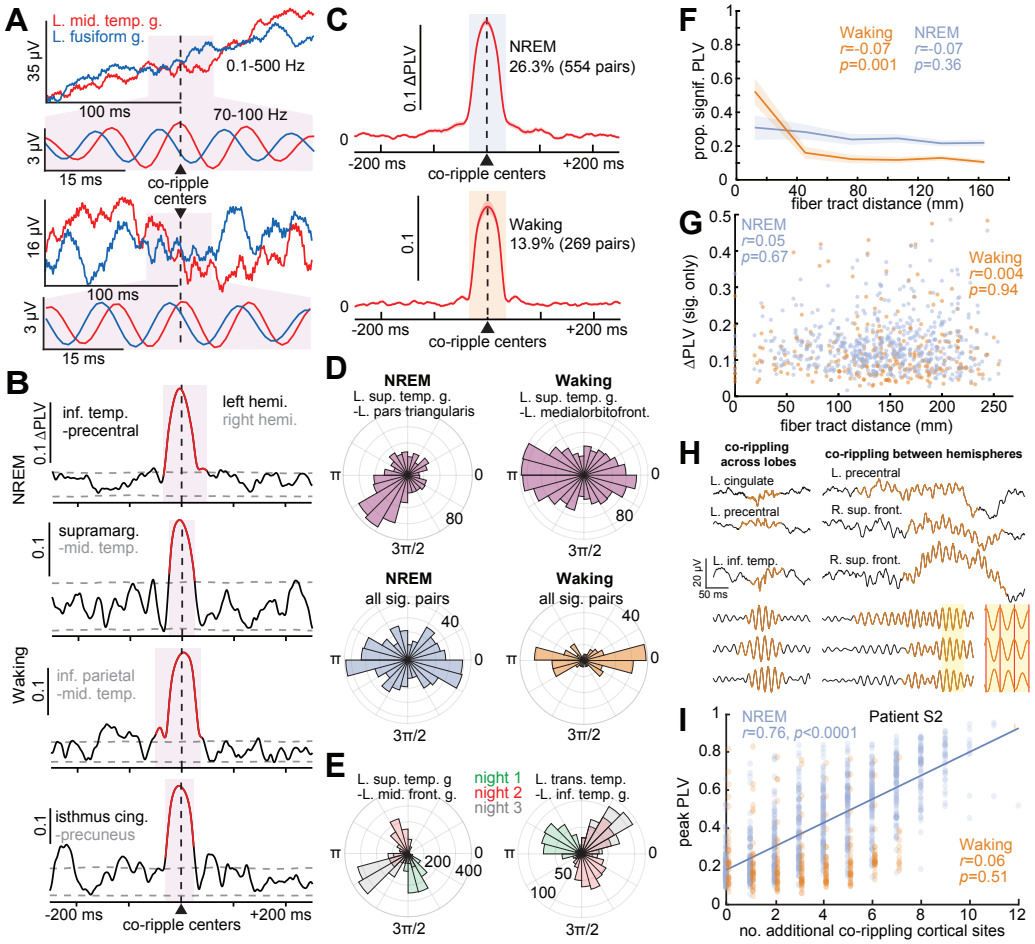

Fig. 3.4. Ripples phase-lock across wide separations in the cortex. (**A**) Two example pairs of co-occurring ripples in broadband LFP and 70-100Hz bandpass. A consistent phase-lag from the left middle temporal gyrus (red) to left fusiform gyrus (blue) is evident in the expanded bandpassed (70-100Hz) 50ms long traces centered on the co-ripple (pink background). (**B**) Example 70-100Hz PLV time-courses calculated between ripples co-occurring between ipsilateral and contralateral cortical sites (≥25ms overlap) in NREM and waking (red shows post-FDR $p<0.05$, randomization test, 200 shuffles/channel pair). (**C**) Average ΔPLVs (relative to -500 to -250ms) for cortical channel pairs with significant PLV modulations. A greater percentage of pairs had significant co-ripple PLV modulations during NREM (26.3%) than waking (13.9%). (**D**) Polar histograms of waking and NREM 70-100Hz phase-lags across co-ripples for two example cortico-cortical pairs with significant PLV modulations (top) and across channel pair circular means (bottom). Cortico-cortical phase-lags had a significant preference for ~0 or ~π during waking compared to NREM based on the counts within $0\pm\pi/6$ or $\pi\pm\pi/6$ vs. outside these ranges for NREM vs. waking ($p=5\times10^{-8}$, $\chi^2=29.75$, df=1). (**E**) Example co-ripple phase-lag distributions for different sleep nights. The dominant phase-lag for co-ripples changes across nights (color-coded). (**F**) Proportion of channel pairs with significant PLVs has a weak, non-significant decrease over distance during NREM and a weak but significant decrease, notably at shorter distances, during waking. (**G**) ΔPLV does not decrement with intervening fiber tract distance for channel-pairs with significant PLVs (linear mixed-effects with subject as random effect). (**H**) Single sweep broadband LFP and normalized 70-100Hz bandpass show waking ripples (orange) co-occurring across lobes (left) and between hemispheres (right). Note the consistency of ~0 or ~π phases in the shaded inset. (**I**) Peak PLV correlates with the number of additional cortical sites co-rippling during NREM in a sample patient (N=10/17 patients significant, post-FDR $p<0.05$, significance of the correlation coefficient) more often than waking (N=3/17). Fit is linear least-squares regression. PLV=phase-locking value.

Phase-locked co-ripples have a broader range of phase-lags in NREM compared to waking and may vary across nights

Having demonstrated significant phase-locking between cortical co-rippling sites, we evaluated the distribution of the circular mean phase angles across site pairs. We found that during NREM the average phase angles for different cortical site-pairs that had significant co-ripple phase-locking had a fairly even distribution from 0 to 2π radians (Fig. 3.4D left). However, during waking, co-ripple phase-lags across pairs tended to be ~0 or ~π (Fig. 3.4D right). This difference was significant ($p=5\times10^{-8}$, $\chi^2=29.75$, df=1; using counts within $0\pm\pi/6$ or $\pi\pm\pi/6$ vs. outside these ranges for NREM vs. waking). This observation suggests a greater tendency toward zero phase-lag during waking (we provide evidence below that the ~0 and ~π lags are functionally equivalent and may be due to a variability in fine-scale electrode contact placement relative to cortical layers). This may be related to the greater tendency of ripples to couple at near zero latency during waking (Fig. 3.2A).

We also tested whether phase-lags during NREM varied across nights. For each patient with multiple sleep nights ($N=16$), we compared the co-ripple phase-lags between all possible pairs of sleep nights within channel pairs that had significant PLV modulations. We found that 42.0% (1256/2426) of such pairs were significantly different in their phase-lags between nights (Fig. 3.4E; post-FDR $p<0.05$, Watson-Williams test; minimum 30 co-ripples per night per channel pair). These differences in co-ripple phase-lags between particular cortical sites suggest that they may participate in different networks across nights, as may happen, for example, when re-activating cortical representations associated with different memories. Similar phenomena have been noted in large-scale cortical models (Izhikevich et al., 2006).

Ripples phase-lock robustly across long distances

Since declarative memories characteristically unite disparate elements that are encoded in widespread cortical locations in both hemispheres, any neurophysiological process supporting their encoding, consolidation, or retrieval must likewise function across those distances. Thus, given that

cortico-cortical ripple co-occurrences do not decrement with distance (tested up to 200mm, Fig. 3.2E-F), we hypothesized that cortico-cortical co-ripple phase-locking also does not decrement with distance. Indeed, we found that, like ripple co-occurrences, the proportion of channel-pairs with significant PLV modulations (Fig. 3.4F; r=-0.07, p=0.36, linear mixed-effects) and the magnitude of these PLV modulations (Fig. 3.4G; r=0.05, p=0.67) did not significantly decrement with intervening fiber tract distance during NREM. During waking, there was a significant decrement in the proportion of channel-pairs with significant PLV modulations with distance, more notably at shorter distances (Fig. 3.4F; r=-0.07, p=0.001), but no decrement in the magnitude of significant channel-pair PLV modulations with distance (Fig. 3.4G; r=0.004, p=0.94). Thus, the physiological action supported by co-rippling may span the entire cortical surface.

Phase-locking increases with more cortical sites co-rippling

Ripples often phase-locked across multiple sites, including between hemispheres (Fig. 3.4H), and as described above we found that two sites co-rippling made it more likely that a third site was co-rippling. These findings raise the question of whether activation of widespread co-rippling networks facilitates greater network synchronization. We found a strong positive linear correlation between the number of sites co-rippling and the cortico-cortical co-ripple phase-locking peak amplitude (Fig. 3.4I). These results were again found when the ΔPLV (peak PLV minus baseline PLV) was used instead of the peak PLV (ΔPLV: N=7/17 patients significant during NREM, N=1/17 significant during waking, post-FDR p<0.05, significance of the correlation coefficient). Thus, the co-occurrence of ripples promotes further co-occurrence, which enhances phase-locking.

Hippocampo-cortical pairs rarely if ever phase-lock

Cortico-cortical phase-locking could be driven through a network of coupled cortical oscillators, a central driving mechanism, or a combination (Fig. 3.6A). Since hippocampal ripples strongly co-occur with cortical ripples (Fig. 3.2B), we investigated whether the hippocampus drives phase-locking of ripples

in the cortex by testing if there is phase-locking between hippocampo-cortical co-ripples. For hippocampo-cortical pairs during sleep, 277/461 had more than 40 co-occurring ripples, and 1.4% (4/277) of these had significant PLV modulations. During waking, 333/461 of the hippocampo-cortical channel-pairs had more than 40 co-occurring ripples, and 0.3% (1/333) of these had a significant PLV modulation (SFig. 3.4C-F; STable 3.5). Examination of electrode trajectories suggested that the hippocampal contacts with significant PLV with cortical sites were probably located in the subicular complex rather than the hippocampus proper, consistent with the finding in mice that ripple propagation from hippocampus to retrosplenial cortex is via the subiculum (Nitzan et al., 2020). Thus, it is unlikely that cortico-cortical ripple phase-locking is driven by common inputs from a hippocampal ripple, which supports the hypothesis that cortico-cortical co-ripple phase-locking is driven intracortically.

Cortical ripples are associated with increased and phase-modulated single unit firing

For ripples to have a role in the communication and integration of information between distant cortical sites requires that neuronal action-potentials coordinate with ripple occurrence and phase. We analyzed microarray recordings from human lateral temporal cortex granular/supragranular layers in 3 patients (STable 3.6) during NREM to test whether ripples modulate local single unit spiking. We detected spikes and sorted them into putative pyramidal (PY) and interneuron (IN) units based on waveform shapes and spike-timing characteristics, and verified that the units had large peak signal-to-noise ratios (PY: 9.12±3.39; IN: 5.23±2.88), had minimal interspike intervals that were <3ms (PY: 0.21±0.34%; IN: 0.33±0.58%; low percentages indicate minimal contamination by other units), and were well-isolated from one another based on the projection test (Pouzat et al., 2002) (PY: 95.38±86.00 SD; IN: 82.84±83.35 SD). We also detected ripples recorded by the array's microcontacts. We found that cortical ripples were associated with increased single unit-firing (Fig. 3.5A-B). Putative pyramidal cells had a 315% increase and putative interneurons had a 345% increase in spiking during ripples compared to baseline (randomly selected epochs in between ripples that were matched in number and duration to the ripples). Furthermore, unit-firing was strongly phase-modulated by the ripples (Fig. 3.5A), with 95%

(68/73) of putative pyramidal cells and 86% (31/36) of putative interneurons having significant 70-100Hz phase modulations during local ripples (Fig. 3.5C; post-FDR $p<0.05$, binomial test between phases within $0\pm\pi/2$ vs. $\pi\pm\pi/2$, expected value=0.5, minimum 30 spikes per unit across ripples). Thus, since unit spiking is coupled to the local ripple phase, and since ripple phases are synchronized at long distances, these data suggest that ripples coordinate unit spike-timing between wide separations in the cortex, which could enable phase selection, coincidence detection, re-entrant processing, and spike-timing-dependent plasticity (Fig. 3.6B). These basic neurophysiological processes would influence the cooperative selection of cell-assemblies between cortical areas, the essence of binding.

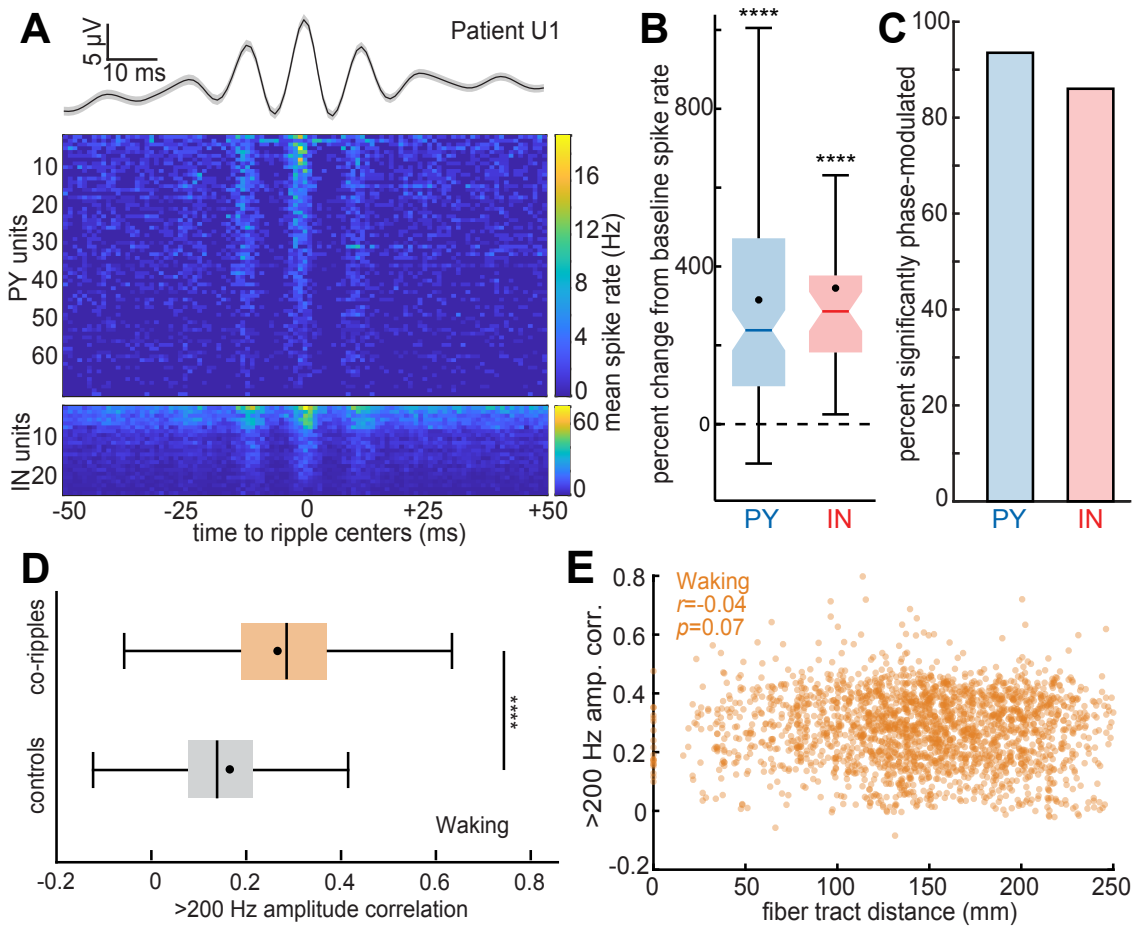

Fig. 3.5. Cortical ripples modulate local single unit spiking and synchronize high-frequency activity between distant regions. (**A**) Average cortical ripple broadband LFP and associated raster plot of pyramidal (PY) and interneuron (IN) mean spike rates across ripples during NREM. Note the phase-coupling of both PY and IN spiking to the ripple peaks. (**B**) Single unit spike rates increase during cortical ripples compared to baseline, which was comprised of randomly selected epochs in between ripples matched in number and duration (PY: *N*=133, mean=315%; IN: *N*=38, mean=345%; patients U1-3). (**C**) Single units are significantly phase-modulated by cortical ripples (PY: *N*=68/73 significant; IN: *N*=31/36 significant; binomial test between phases within 0±π/2 vs. π±π/2, expected value=0.5, minimum 30 spikes per unit across ripples). (**D**) Correlation of the >200Hz analytic amplitude, a proxy for unit spiking, increases during waking co-ripples compared to randomly selected preceding control periods (within -10 to -2 s) matched in number and duration (*N*=2275 SEEG channel pairs). ****p<0.0001, two-sided paired *t*-test. (**E**) Average >200Hz amplitude correlation between co-ripples for each cortical channel-pair does not decrement with fiber tract distance.

Co-rippling increases putative unit-activity correlation between distant cortical sites

Our findings that co-ripples are often phase-locked across distant sites, and that unit-firing is phase-locked to local ripples, together imply that unit-firing is also correlated across distant sites. We were unable to test this prediction directly because we did not perform microelectrode recordings of units

in multiple locations separated by more than ~5mm. Rather, as an indirect test, we used >200Hz amplitude from SEEG recordings as a proxy for unit-firing (Mukamel et al., 2005). During waking but not NREM, this measure was highly correlated when cortical sites were co-rippling vs. when they were not (Fig. 3.5D, $p=8\times10^{-303}$, two-sided paired *t*-test). Correlation between co-rippling sites did not significantly decrement with increasing distance between the sites (Fig. 3.5E; $r=-0.04$, $p=0.07$, significance of the correlation coefficient).

As described above, co-ripple phase-lags between channels tended to be near 0 or π, especially during waking. This could indicate that co-rippling sometimes represents a state of inhibited communication, or simply that our bipolar SEEG derivations had variable relationships to local ripple generating dipoles. To test these hypotheses, we compared the >200Hz amplitude correlations between sites, when the sites had co-ripple phase-lags of $0\pm\pi/6$ vs. $\pi\pm\pi/6$ (averaged within these ranges for each channel-pair). No significant difference was found for waking or NREM (Waking: $p=0.17$; NREM: $p=0.07$, two-sided paired *t*-test, $N=2275$ channel pairs), thus suggesting that the lags near 0 and π are functionally equivalent as would be expected if they are due to slight differences in electrode location relative to cortical lamina.

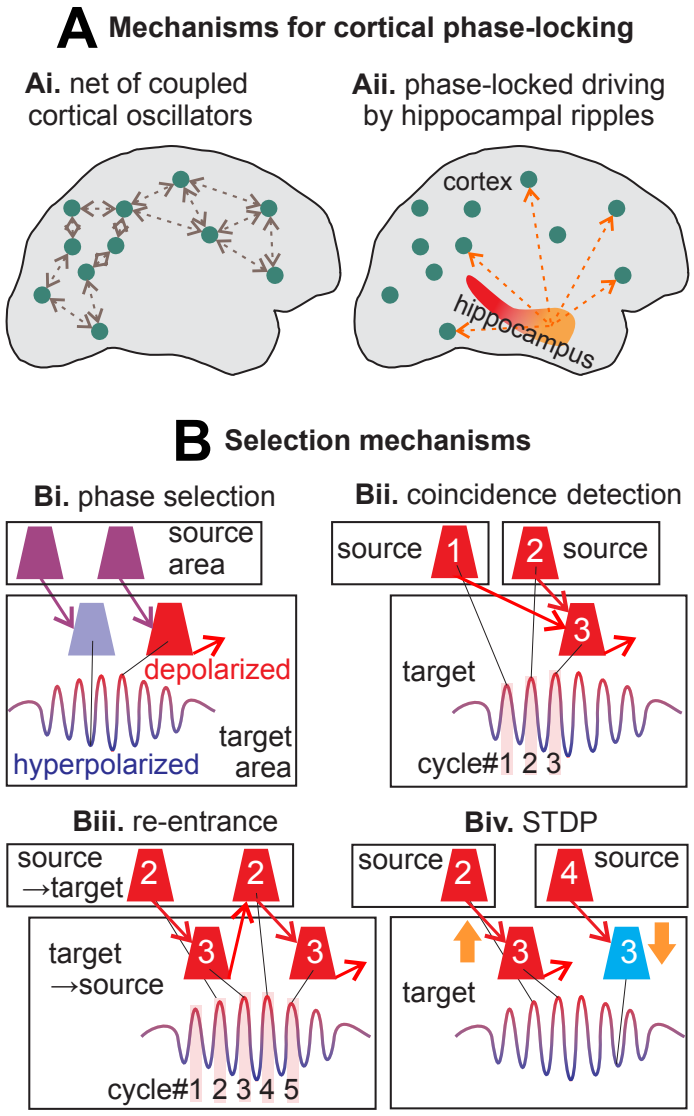

Fig. 3.6. Mechanisms of phase-locked networks of cortical ripples and their selection. (**A**) Potential mechanisms for ripple phase-locking across broad cortical regions: (**Ai**) multiple cortico-cortical re-entrant connections between the cortical oscillators; (**Aii**) distributed driving oscillations from a subcortical location (e.g., hippocampal ripples). (**B**) Multiple synergistic mechanisms enabled by cortico-cortical co-rippling could select a spatiotemporal neural network. (**Bi**) Spikes arriving at the hyperpolarized phase will be ineffective relative to those arriving at the depolarized phase in eliciting spikes in the rippling target area. (**Bii**) Coincident spikes arriving from two source areas that are phase-locked with the target area are more likely to trigger an action-potential, especially if they arrive in the depolarized phase. Note that conduction times between areas does not need to match the phase-lag but could equal the phase-lag plus multiples of the cycle time (e.g., cell #1→3). (**Biii**) Re-entrant activation across cycles could also result from reciprocal connections. (**Biv**) The synapses effectively evoking spikes (2→3) would be strengthened with spike-timing-dependent plasticity (STDP), whereas those arriving from a non-phase-locked area (4→3) would arrive after the target cell fires and thus be weakened. Whereas the mechanisms in (Bi-iii) would act synergistically to reinforce in-phase firing between co-rippling sites within a given ripple, the mechanism in (Biv) would act across ripples to reinforce a particular network of co-rippling sites.

Discussion:

Here, using human intracortical recordings, we show that ripples couple, co-occur, and phase-synchronize across all lobes and between both hemispheres, with little decrement, even at long distances. The rate of co-rippling above chance increased exponentially with the proportion of co-rippling sites, which was correlated with stronger phase-locking. Cortical neurons increased firing during ripples and phase-locked to them, a requisite for ripples to enhance interaction via gain-modulation and coincidence detection. Enhanced long-distance interaction during co-rippling between sites was supported by increased high-frequency correlation. In addition to spontaneously occurring during both NREM and waking, cortico-cortical and hippocampo-cortical ripple co-occurrence specifically increased preceding successful delayed recall. Overall, our results suggest that distributed, phase-locked cortical ripples possess the properties that may allow them to facilitate integration of the different elements comprising a particular declarative memory, or more generally, to help 'bind' different aspects of a mental event encoded in widespread cortical areas into a coherent representation.

Previous work showed that coupling of anterolateral temporal and parahippocampal ripples in humans increases prior to correct recall in paired-associates learning (Vaz et al., 2019). We show that such coupling also occurs between hippocampal and cortical ripples. Further, we show that immediate recall with no intervening distractor, a task with identical sensory and motor stimulation but that does not require the hippocampus (Squire, 1992), is not associated with increased hippocampo-cortical ripple coupling. Critically, given the importance of transcortical connections between sites encoding previously unrelated elements in declarative memory, we show that cortico-cortical ripple coupling also strongly increases prior to correct recall following a delay.

In addition to consolidation during sleep, the hippocampus is needed for memory formation during waking, as demonstrated by transient medial temporal inactivation (Halgren, 1990). Indeed, we found that spontaneous hippocampal ripples were more tightly coupled with cortical ripples in waking compared to NREM. However, unlike NREM, during which 67% of hippocampo-cortical channel-pairs with a significant order preference had hippocampal ripples preceding cortical, during waking the

opposite was true, with cortex leading in 85%. While speculative, these observations are consistent with the cortex generally providing information to the hippocampus for encoding during waking (when hippocampal ripples follow cortical), and then the hippocampus providing information to the cortex for consolidation during NREM (when hippocampal ripples precede cortical).

A novel finding of this study is that spontaneous cortical ripples couple (within ±500ms), co-occur (≥25ms overlap), and often phase-lock (synchronize) across large areas of both hemispheres during both sleep and waking. The minimal decrement with distance in co-occurrence or phase-locking suggests either a central driving oscillator, or a population origin, such as a web of coupled oscillators (Fig. 3.6A). The hippocampus is unlikely to act as a central driving oscillator because hippocampo-cortical coupling and co-rippling is rarer than cortico-cortical, and hippocampo-cortical phase-locking is essentially absent. A preponderance of cortico-cortical influences might be expected given that each cortical pyramidal cell receives input from thousands of other pyramids, whereas the fan-out from hippocampus (CA1 plus subiculum) to cortex is ~1:500, so each cortical pyramid gets on average less than 10 hippocampal synapses (Azevedo et al., 2009; Simić et al., 1997).

Conversely, a network of coupled oscillators is consistent with the finding in cats that section of the corpus callosum disrupts gamma-synchrony between V1 in the two hemispheres (Uhlhaas et al., 2009). Furthermore, the highly uniform ripple frequency observed across sites, cortical regions, and individual ripples suggests that local cellular and network mechanisms set the resonant oscillation frequency of each cortical module to the same 80Hz frequency, which are thereby prone to co-oscillate when excited and connected. A major role of cortico-cortical interactions in ripple co-occurrence and phase-locking is also suggested by the strong positive feedback we observed in the spread of cortico-cortical co-occurrence and the intensity of cortico-cortical phase-locking. Specifically, cortico-cortical co-occurrence probability during waking increases from about twice chance levels for two co-occurring sites to about 20,000 times chance for co-occurrence in 25% of the sites. Similarly, during NREM, peak cortical ripple PLV between sites increases linearly with the number of additional sites co-rippling, from

~0.2 with no additional sites to ~0.9 with twelve. Note that a PLV of 1.0 would indicate perfect consistency of phase between sites over all of their co-occurring ripples.

It may seem unlikely that cortico-cortical interactions could support zero-lag phase-locking at long distances, with minimal decrement up to 250mm as was demonstrated here. Cortico-cortical fibers are unlikely to conduct much faster than 10m/s, or 125mm between successive peaks of an 80Hz ripple (Waxman et al., 1977). However, synchronizing projections can still be effective at multiples of the cycle time, especially with recurrent connectivity (Fig. 3.6B), as is typical in the cortex. Actually, since long-range fibers are quite rare in human cortex, whereas local connectivity and U-fibers are dense, an astronomical number of possible multi-synaptic routes exist between any two cortical locations. Indeed, modelling studies show that phase-locked oscillations at ~80Hz can occur in extended cortical networks, even at zero lag, provided that the neurons have multiple-path recurrent connectivity (Bazhenov et al., 2008; Vicente et al., 2008). Thus, although direct evidence is lacking, the most likely possibility given our findings is that ripples co-occur and phase-lock due to emergent cortico-cortical interactions.

We found that cortico-cortical co-rippling and phase-locking show consistent differences between states. Although spontaneous cortical ripple occurrence density is higher in NREM, co-occurrence density is higher in waking. Accordingly, the likelihood of multiple sites co-rippling relative to chance grows more rapidly with number of sites during waking than NREM, the increase being about 25 times larger when 25% of sites are co-rippling. Overall, the proportion of ripple peaks that occur within 25ms of each other is about five times greater in waking than NREM. Furthermore, when co-ripples phase-lock they are more likely to be effectively synchronous in waking than NREM. These properties are consistent with a rapid highly synchronous recruitment of multiple cortical sites by a high activation during waking ripples, and by contrast, a sequential activation of NREM ripples. Higher activation is indicated by the greater increase in >200Hz amplitude during waking compared to NREM ripples. Conversely, NREM ripples tend to recruit sequentially across the cortex, with an increase in associated cell-firing.

A mean of about 16 widely-distributed cortical locations were sampled per patient. Assuming that a ripple generating module spans ~1mm^2 of cortical surface (unpublished data), this indicates that we

recorded from only ~1/10000th of the ripple modules. If the distances between a significant number of recording sites were less than the size of rippling modules, then there would be increased co-rippling found at short inter-contact distances. The absence of such an effect allows the proportion of recorded sites to be used as an estimate of the proportion of the cortex that is rippling. If so, then at times, as much as 25% of the cortex is co-rippling. Similarly, the usual proportion of the cortex co-rippling can be roughly estimated from the probability, given a ripple, that another site is co-rippling, ~8% (assuming that the ripple's lead-field is comparable to its module size).

Given the strong ripple phase-modulation of cell-firing we demonstrated, ripples can be expected to strongly modulate the effectiveness of arriving synaptic input, with spikes arriving on the depolarized phase being far more likely to trigger post-synaptic firing. Thus, there may be a strong selection for cells that project (even multi-synaptically) between co-rippling sites with a latency matching the phase-lag (possibly plus multiples of the cycle time, Fig. 3.6Bi). Additionally, when multiple sites co-ripple, then spikes that arrive together at a third location may have greatly enhanced effectiveness (i.e., the post-synaptic site acts as a coincidence detector, Fig. 3.6Bii) (Salinas et al., 2001). Synaptic phase-selection and coincidence detection are synergistic, and would further imply positive feedback due to recurrence (Fig. 3.6Iii). Connectivity between co-rippling locations supporting in-phase interactions would be progressive because the pre- and post-synaptic activation these mechanisms induce would strengthen in-phase connections via STDP (Fig. 3.6Biv). Note the requisite pre-condition for this progressive strengthening of in-phase connections is that there is consistency of phase-lags across all waking or NREM co-ripples of a site-pair, which is what our criterion for phase-locking required. However, the gain-modulation and coincidence detection mechanisms would also function between sites that are co-rippling but not phase-locked according to our criterion, because cross-site phase is still consistent within each co-ripple due to the small range of ripple frequencies (50% within ~0.3Hz of the mean). Thus, through gain modulation and coincidence detection (Fries, 2009), co-rippling may strongly select the distributed cortical network active during a co-rippling event.

Through these mechanisms, cortical ripples could activate and couple with distant but related encoding areas through progressive activation of a web of cortico-cortical positive feedback connections. The strongly increased probability of co-activation and phase-locking with increasing numbers of contacts already co-activating suggests positive feedback recruitment of the most interconnected and co-activated cells into a brief synchronous ripple. When locations join the rippling network and resonate with other members, their activity level increases. The function of the ripple could thus be to act as an amplifier through resonance, leading to the rapid assembly of a network encoding the various aspects of an event.

A potential role of co-ripples in facilitating the communication and integration of information between distant cortical sites requires both the synchronized oscillations in trans-membrane currents generating the co-ripples *per se*, and coordinated neuronal action-potentials. We show here that single putative pyramidal and interneurons in lateral temporal cortex increase their firing during ripples in a manner that is strongly modulated by the phase of the individual ripple cycles. Therefore, the cell-firing patterns necessary to support selection of activated neurons within the co-rippling locations using gain modulation and coincidence detection are in place. While we did not simultaneously record single units in multiple distant locations to directly confirm that they are co-firing, we obtained some indication that this may be the case by examining the envelope of >200Hz local field potentials. We found that the correlation between these envelopes in distant locations is greater when they are co-rippling, and furthermore, this increase in correlation does not decrease with distance, even if the sites are in different lobes or hemispheres.

The principle alternative proposed mechanism for binding relies on hierarchical convergence in multi-attribute, multisensory areas (Merker, 2013; Shadlen et al., 1999). This mechanism seems inconsistent with the highly distributed nature of cortical processing, and poses the difficulty how to pre-represent in a small cortical module each of the combinatorial possibilities of all elements contained in all potential experiences. However, the hippocampus seems to do this, albeit temporarily, with receptive fields that combine indicators of position from multiple modalities, as well as valence, history, and context (Eichenbaum, 2014). Hippocampal assembly of the different elements of an event does not

require integration across the hippocampus because these elements are available locally, having been pre-mixed by the entorhinal cortex and dentate gyrus. Thus, hippocampal ripples are for communication with the cortex rather than with other hippocampal sites, and indeed they are typically local within the hippocampus (Jiang et al., 2019b; Patel et al., 2013); rather, their crucial co-occurrences may be with widespread cortical ripples. In this view, binding of cortical elements can occur in the absence of hippocampal input if they are previously consolidated, because cortico-cortical co-rippling and phase-locking are dependent on intracortical processes.

In summary, the characteristics of co-occurring and phase-locked cortical ripples found in the current study appear to fulfill the central requirements for a neurophysiological process that could facilitate binding-by-synchrony. First, ripples occur in all regions of the cortex in both hemispheres (required by binding because the elements of experience are encoded throughout the cortex). Second, ripples occur spontaneously throughout waking and NREM (required since binding is a ubiquitous process), and are elevated during task periods when binding may be useful (such as reassembling the components of a memory). Third, ripples last ~70ms, a duration considered in the range of 'the psychological moment' (Wittmann, 2015). Fourth, ripples strongly increase local firing and firing-proxy >200Hz amplitude (required for inter-areal communication). Fifth, ripples strongly phase-modulate local putative pyramidal and interneuron firing in a manner consistent with input modulation (a primary hypothesized mechanism whereby oscillations selectively amplify particular neural assemblies). Sixth, ripples strongly co-occur and phase-lock between cortical sites indicating active cortico-cortical communication (required because without communication there cannot be integration). This strong phase-locking occurs between cortical sites but not between cortex and hippocampus, indicating that trans-cortical synchrony is probably intrinsic, i.e., not projected from elsewhere. Furthermore, co-occurrence and phase-locking is minimally affected by distance (required for integration of diverse elements). Finally, >200Hz amplitude is more correlated between sites when they are co-rippling, further suggesting interareal integration of unit-firing. Additional evidence from simultaneous distributed cellular level

recordings, as well as direct interventions in model systems, will be necessary to confirm that cortical co-ripples provide the neural substrate for binding.

Methods:

Patient selection

Data from a total of 25 patients (13 female, 31±11 years old) with pharmaco-resistant epilepsy undergoing intracranial recording for seizure onset localization preceding surgical treatment were included in this study (STable 3.1,6). Patients whose stereoelectroencephalography (SEEG) recordings were analyzed were only included in the study if they had no prior brain surgery; background EEG (with the exception of epileptiform transients) in the normal range; and electrodes implanted in what was eventually found to be non-lesional, non-epileptogenic cortex, as well as non-lesional, non-epileptogenic hippocampus (such areas were suspected to be part of the focus prior to implantation, or were necessary to pass through to reach suspected epileptogenic areas).

In addition, 3 of these patients were also implanted with an intracranial microelectrode (Utah Array) into cortical tissue that was suspected based on pre-surgical evaluation to be included within the region of the therapeutic resection (STable 3.6). The implantation of the array did not affect clinical monitoring. In all patients, the tissue into which the array was implanted was later resected to gain access to the surgical focus beneath, the electrode was determined not to be implanted in epileptogenic tissue, and seizures were determined not to originate from the area where the array was implanted.

Patients were excluded from the study if they had prior brain surgery or did not have non-lesioned hippocampal and cortical channels that were not involved in the early stage of the seizure discharge and did not have frequent interictal activity or abnormal local field potentials. Based on these criteria, 25 were included in this study out of a total of 83. All patients gave fully informed written consent for their data to be used for research as monitored by the local Institutional Review Boards at Cleveland Clinic, University of California, San Diego, Oregon Health & Science University, and Partners HealthCare (including Massachusetts General Hospital),

Intracranial recordings

Patients were implanted with intracranial electrodes for ~7 days with continuous recordings for seizure onset localization. SEEG electrode implantation and targeting were made for purely clinical purposes. SEEG recordings were collected with a Nihon Kohden JE-120 amplifier at 1000Hz sampling (patients S1-17), Natus Quantum LTM amplifier at 1024Hz (patients S18-19), or Natus Xltek EMU128FS (patients S20-22). Standard clinical electrodes were 0.8Mm diameter, with 10-16 2mm long contacts at 3.5-5mm pitch (~150 contacts/patient). In addition, patients S19 and S22 had electrodes with 0.5-2mm long contacts at 1-2mm pitch.

Electrophysiology pre-processing

Offline data preprocessing was performed in MATLAB 2019b and LFPs were inspected visually using the FieldTrip toolbox (Oostenveld et al., 2011). SEEG data were downsampled to 1000Hz with anti-aliasing and 60Hz notch filtered (zero-phase) with 60Hz harmonics up to 480 Hz. Transcortical contact pairs were identified using both anatomical location (using the pre-operative MRI aligned to the post-operative CT), and physiological properties (high amplitude, coherence and inversion of spontaneous activity between contacts), and selected such that no 2 pairs shared a contact, with the exception of the 1mm spaced hippocampal bipolar channels described above. All SEEG analyses were performed using bipolar derivations between contacts separated by 1-5 mm in cortical or hippocampal gray matter in order to ensure that activity was locally generated (Mak-McCully et al., 2015).

Channel selection

Channels were excluded from analysis if they were in lesioned tissue, involved in the early stages of the seizure discharge, had frequent interictal activity, or abnormal local field potentials. From the total 2772 bipolar channels (1326 left hemisphere) in the 22 SEEG patients (S1-22), 52 hippocampal (24 left hemisphere) and 403 transcortical (180 left hemisphere) bipolar channels were selected for the analyses

(STable 3.1). Polarity was corrected for individual bipolar channels such that downstates were negative and upstates were positive. This was accomplished by ensuring that during NREM, negative peaks were associated with decreased, and positive peaks were associated with increased, mean ±100ms 70-190Hz analytic amplitude, an index of cell-firing that is strongly modulated by downstates and upstates (Csercsa et al., 2010).

Electrode localization

Cortical surfaces were reconstructed from the pre-operative whole-head T1-weighted structural MR volume using the standard FreeSurfer recon-all pipeline (Fischl, 2012). Atlas-based automated parcellation (Fischl et al., 2004) was used to assign anatomical labels to regions of the cortical surface in the Destrieux (Destrieux et al., 2010) atlas. In addition, automated segmentation was used to assign anatomical labels to each voxel of the MR volume, including identifying voxels containing hippocampal subfields (Iglesias et al., 2015). In order to localize the SEEG contacts, the post-implant CT volume was registered to the MR volume, in standardized 1mm isotropic FreeSurfer space, using the general registration module (Johnson et al., 2007) in 3D Slicer (Fedorov et al., 2012). The position of each SEEG contact, in FreeSurfer coordinates, was then determined by manually annotating the centroids of electrode contact visualized in the co-registered CT volume. Each transcortical contact pair was assigned an anatomical parcel from the atlas above by ascertaining the parcel identities of the surface vertex closest to the contact-pair midpoint. Subcortical contacts were assigned an anatomical label corresponding to the plurality of voxel segmentation labels within a 2-voxel radius. Transcortical contact pair locations were registered to the fsaverage template brain for visualization by spherical morphing (Fischl et al., 1999). White-matter streamline distances between channels were computed using the 360 parcels of the HCP-MMP1.0 atlas (Glasser et al., 2016), as determined by probabilistic diffusion MRI tractography (Behrens et al., 2007), are population averages from (Rosen et al., 2021). When two channels were in the same HCP parcel the distance was considered to be 0.

Time-frequency analyses

Average time-frequency plots of the ripple event-related spectral power (ERSP) were generated from the broadband LFP using EEGLAB (Delorme et al., 2004). Event-related spectral power was calculated from 1Hz to 500Hz with 1Hz resolution with ripple centers at t=0 by computing and averaging fast Fourier transforms with Hanning window tapering. Each 1Hz bin of the time-frequency matrix was normalized with respect to the mean power at -2000 to -1500ms and masked with two-tailed bootstrapped significance (N=200) with FDR correction and α=0.05 using -2000 to -1500ms as baseline.

Sleep and waking epoch selection

Epochs included in the study did not fall within at least 1 hour of a seizure and were not contaminated with frequent interictal spikes or artifacts. NREM periods were selected from continuous overnight recordings where the delta (0.5-2Hz) analytic amplitude from the cortical channels was persistently increased (STable 3.1). Sleep epochs were confirmed by visual inspection to have normal appearing spindles, downstates, and upstates. Waking periods were selected from continuous daytime recordings that had persistently low cortical delta as well as high cortical alpha (8-12 Hz), beta (20-40Hz), and high gamma (70-190Hz) analytic amplitudes. When the data included electrooculography (EOG; N=15/17 SEEG patients S1-17), waking periods also required that the 0.5-40Hz analytic amplitude of the EOG trace was increased. Waking epochs were required to be separated from periods of increased delta analytic amplitude by at least 30 minutes.

Ripple detection

Ripple detection was performed in the same way for all structures and states and was based on a previously described hippocampal ripple detection method (Jiang et al., 2019a, 2019b). Requirements for inclusion and criteria for rejection were determined using an iterative process across patients, structures, and states. Data were bandpassed at 60-120Hz and the top 20% of 20ms moving root-mean-squared peaks were detected. It was further required that the maximum z-score of the analytic amplitude of the 70-

100Hz bandpass was greater than 3 and that there were at least 3 distinct oscillation cycles in the 120Hz lowpassed signal, determined by shifting a 40ms window in increments of 5ms across ±50ms relative to the ripple midpoint and requiring that at least 1 window have at least 3 peaks. Adjacent ripples within 25ms were merged. Ripple centers were determined as the time of the maximum positive peak in the 70-100Hz bandpass. To reject epileptiform activities or artifacts, ripples were excluded if the absolute value of the z-score of the 100Hz highpass exceeded 7 or if they occurred within 2s of a ≥1mV/ms change in the LFP. Ripples were also excluded if they fell within ±500ms of putative interictal spikes, detected as described below. To exclude events that could be coupled across channels due to epileptiform activity, we excluded ripples that coincided with a putative interictal spike on any cortical or hippocampal channel included in the analyses. Events that had only one prominent cycle or deflection in the broadband LFP that manifested as multiple cycles above detection threshold in the 70-100Hz bandpass were excluded if the largest valley-to-peak or peak-to-valley absolute amplitude in the broadband LFP was 2.5 times greater than the third largest. For each channel, the mean ripple-locked LFP and mean ripple band were visually examined to confirm that there were multiple prominent cycles at ripple frequency (70-100Hz) and the mean time-frequency plot was examined to confirm there was a distinct increase in power within the 70-100Hz band. In addition, multiple individual ripples in the broadband LFP and 70-100Hz bandpass from each channel were visually examined to confirm that there were multiple cycles at ripple frequency without contamination by artifacts or epileptiform activity. Channels that did not contain ripples that meet these criteria were excluded from the study.

Additional analyses were performed specifically on sharpwave-ripples and spindle-ripples detected according to our previous methods (Jiang et al., 2019a, 2019b). First, NREM data were bandpassed from 70-100Hz, and a putative ripple was detected when the 20ms moving root-mean-squared amplitude exceeded the 90th percentile. Ripples were required to have at least 3 distinct oscillation cycles as described above. Broadband LFP data ±2s around ripple centers underwent 1-D wavelet (Haar and Daubechies) decomposition to detect and remove sharp transients. Ripples were classified as sharpwave-ripples based on the similarity of the peri-ripple LFP to the 400ms average biphasic waveform template

created for each subject using 100-300 hand-marked hippocampal sharpwave-ripples, as quantified by the dot product between the template and the peri-ripple LFP (-100 to 300ms), and the absolute difference between the LFP value at the ripple center. Ripples were classified as spindle-ripples if the ripple center occurred during a hippocampal spindle, detected in the same way as described below for cortical spindles, on the same channel. Ripples could be classified as both sharpwave-ripples and spindle-ripples if they met both of these criteria.

Interictal spike detection and rejection

Ripples and sleep graphoelements were excluded if they were within ±500ms from putative IIS detected as follows. A high frequency score was computed by smoothing the 70-190Hz analytic amplitude with a 20ms boxcar function and a spike template score was generated by computing the cross-covariance with a template interictal spike. The high frequency score was weighted by 13 and the spike score was weighted by 25, and an IIS was detected when these weighted sums exceeded 130. In each patient, detected IIS and intervening epochs were visually examined from hippocampal and cortical channels (when present) to confirm high detection sensitivity and specificity.

Paired-associates memory task

Paired-associates memory task data were collected from 5 patients using Presentation (Neurobehavioral Systems). Patients were instructed to memorize a series of word pairs and to recall the second word when cued with the first. A word pair was presented with text and audio (pre-recorded speech) along with an integrating image that contained semantic content of both words. After each presentation, immediate recall was assessed by cuing the first word immediately after the offset of the word pair and image. The patient then attempted to recall the word aloud. This was repeated with 8 different pairs followed by a 6s break, and then delayed recall of the 8 pairs was assessed in the same order where the first word was cued and the patient attempted to recall the second word aloud. After 4s the integrating image was displayed. Delayed recall was only considered successful if the second word

was said aloud before the image appeared. This sequence was repeated 20 times for a total of 160 word pairs. For one patient (S18), the task was instead structured as 25 sets of 6 pairs with the integrating image shown during the encoding period but not during delayed recall, and instead during delayed recall the second word was presented after 5s. Delayed recall was only considered successful for this patient if the second word was said aloud before it was presented after 5s. Task performance by patient is summarized in STable 3.4.

During the task, audio containing the stimulus presentations and patient voice was split and simultaneously recorded into the task presentation computer and into the clinical amplifier system synchronously with the intracranial recordings. Stimulus markers sent by the task computer were also synchronized with the intracranial recordings. Scoring of behavioral data was done offline by listening, and recall onsets were identified offline using Audacity v2.4.2 through both visual examination of the task computer recorded audio waveforms and spectrograms and confirmation through listening. The computer recorded audio was downsampled with anti-aliasing to 1000Hz and cross-correlated with the audio recorded alongside the intracranial recordings to ensure high temporal precision of recall onsets.

Ripple occurrences and co-occurrences relative to the word cue (text and audio) preceding recall onsets prior to successful (i.e., correct response before the answer or integrating image was presented in the delayed condition) or unsuccessful (i.e., no response, incorrect response, or response after the answer or image was presented) were computed across trials, where each trial was an average across channels. Null distributions of occurrences were computed by randomly shuffling ripple or co-occurring ripple centers for each channel in each trial within ±3s from cue onset 10 times. Observed over chance (average of null) ripple occurrence and co-occurrence histograms had 25ms bins Gaussian-smoothed with a 100ms window. Trial-wise ripple occurrence and co-occurrence averages in the 150-300ms window following cue onset were computed for statistical analyses.

Ripple temporal relationships

Peri-cortical ripple time histograms of cortical or hippocampal ripples on a different channel were computed. Gaussian smoothed (window=250ms) ripple center counts in channel B were computed in 25ms bins within ±1500ms relative to ripple centers at t=0 in channel A. A null distribution was generated by shuffling (N=200 times) the times of ripple centers on channel B relative to the ripple centers on channel A (at t=0) within the ±1500 window. Pre-FDR p-values were calculated by comparing the observed and null distributions for each bin over ±500ms. P-values were then FDR-corrected for the number of channel pairs across patients multiplied by the number of bins per channel pair (Benjamini et al., 1995). A channel pair was determined to have a significant modulation if there were at least 3 consecutive bins with FDR-corrected p<0.05. Whether cortical ripples were leading or lagging was determined using a two-sided binomial test with expected value of 0.5, using event counts in the 500ms before vs. 500ms after t=0. For plots, 50ms Gaussian smoothed event counts with 50ms bins were used.

Cortical ripple co-occurrences

Ripple co-occurrences between channel pairs were identified by finding ripples that overlapped for at least 25ms. The center of the co-occurring ripple event was determined by finding the temporal center of the ripple overlap. Conditional probabilities of ripple co-occurrence were computed by finding the probability of co-occurrence (minimum 25ms overlap) between two channels given that there was a ripple in one of the channels, separately for each channel. This was done for P(NC|NC) (both orders), P(NC|HC), and P(HC|NC). To estimate the extent of co-rippling across the cortex at any moment, the probability that a given proportion of channels was co-rippling at any time point for each subject was computed.

Observed over chance cortical ripple co-occurrence was computed as a function of the number of sites co-rippling. Ripple co-occurrence of a given number of sites required that all of those sites had at least 25ms ripple overlap. Chance was computed for each patient by randomly shuffling the ripple epochs and inter-ripple epochs of all sites 200 times and calculating the mean number of co-occurrences for each

proportion of co-rippling sites (i.e., the number of channels co-rippling divided by the total number of channels, assessed for the minimum value of 2 or more channels co-rippling).

Cortical ripple co-occurrence significance for each channel pair was computed by comparing the number of observed co-occurrences (25ms minimum overlap) for each channel pair with a null co-occurrence distribution derived from shuffling ripples and inter-ripple intervals 200 times in a moving non-overlapping 5min window and counting co-occurrences.

Ripple phase-locking analyses

To evaluate the extent to which co-occurring ripples at different sites were synchronized at different times, we used the phase-locking value (PLV), an instantaneous measure of phase-locking (Lachaux et al., 1999). PLV time courses were computed using the analytic angle of the Hilbert transformed 70-100Hz bandpassed (zero-phase shift) signals of each channel pair when there were at least 40 co-ripples with a minimum of 25ms overlap for each. PLVs were computed for all such co-ripples for each channel pair across a ±500ms window relative to the temporal centers of the co-ripples. A null distribution was generated by selecting 200 random times within -10 to -2 s relative to each co-ripple center. For plotting, PLV traces were smoothed with a 10ms Gaussian window. Pre-FDR p-values were determined by comparing the observed and null distributions in 5ms duration bins within ±50ms around the co-ripple centers. These p-values were then FDR corrected across bins and channel pairs. A channel pair was considered to have significant phase-locking if it had 2 consecutive bins with post-FDR $p<0.05$. Phase-locking modulation was computed for each channel pair as the difference from the average baseline PLV within -500 to -250ms to the max PLV within ±50ms around the co-ripple center. Phase-locking as a function of the proportion of additional sites co-rippling was computed by identifying co-ripples on the two cortical channels of interest, then sorting these events into groups based on what proportion of additional sites had a ripple that overlapped with the co-ripple by any amount of time, and computing the peak PLV and ΔPLV around the co-ripple centers. Plots of the peak PLV for channel pairs as a function

of the number of additional sites co-occurring (e.g., 3 on the x-axis means 2+3=5 total sites co-rippling) are for channel pairs with significant PLV modulations.

Ripple phase-lag analyses

The phase-lag between co-occurring cortical ripples (25ms minimum overlap) was computed for channels with significant PLV modulations (see above) by finding the circular mean (Berens, 2009) of the angular difference between the two 70-100Hz bandpassed ripples during their overlapping period. The mean phase-lag for a given channel pair was computed by finding the circular mean of these circular means. For each channel pair that had a significant PLV modulation, differences in ripple phase-lags by sleep night were computed for each sleep night pair where both nights had at least 30 co-ripples using the Watson-Williams multi-sample test for equal means.

Unit detection, classification, quality, and isolation

Unit detection and classification was performed according to our published procedures (Chan et al., 2014; Dehghani et al., 2016; Dickey et al., 2021a; Eichenlaub et al., 2020; Le Van Quyen et al., 2016; Peyrache et al., 2012; Teleńczuk et al., 2017). Data were bandpassed at 300-3000Hz and putative unit spikes were detected when the filtered signal exceeded 5 times the estimated standard deviation of the background noise. Units were k-means clustered using the first three principal components of each spike. Overlaid spikes were examined visually and those with abnormal waveforms were excluded. Based on their waveforms, firing rates, and autocorrelograms, action potentials were clustered as arising from putative pyramidal cells or interneurons. Putative pyramidal cells had spike rates of ~0.1-0.8Hz, long valley-to-peak and half width intervals, sharp autocorrelations, and bimodal inter-spike interval (ISI) distributions, reflecting a propensity to fire in bursts (STable 3.6). By contrast, putative interneurons had spike rates of ~1-5Hz, short valley-to-peak and half width intervals, broad autocorrelations, and a predominantly unimodal ISI distribution.

Single unit quality and isolation were confirmed according to previously established guidelines (Kamiński et al., 2020). Unit spikes were verified to well-exceed the noise floor based on large peak signal-to-noise ratios (PY: 9.12±3.39; IN: 5.23±2.88). Since the neuronal spiking refractory period is about 3ms, the percent of ISIs less than 3ms estimates the degree of single unit contamination by spikes from different units, which was very low among the units included in this study (PY: 0.21±0.34%; IN: 0.33±0.58%). Furthermore, single units detected on the same contact were highly separable according to their projection distances (Pouzat et al., 2002) (PY: 95.38±86.00 SD; IN: 82.84±83.35 SD). Lastly, temporal stability of unit spikes over time was confirmed based on consistency of the mean waveform shape and amplitude of each unit across recording quartiles.

Analyses of unit spiking during ripples

Unit spiking was analyzed with respect to local ripples detected on the same contact. Ripple phases of unit spikes were determined by finding the angle of the Hilbert transform of the 70-100Hz bandpassed signal (zero-phase shift) at the times of the spikes. Unit spiking modulations during ripples were computed by comparing the number of spikes for each unit during ripples divided by the number during non-ripple epochs, i.e., epochs in between ripples, that were matched in number and duration to the ripples.

Statistical analyses

All statistical tests were evaluated with $\alpha=0.05$. All p-values involving multiple comparisons were FDR-corrected according to (Benjamini et al., 1995). FDR corrections across channel pairs were done across all channels pairs from all patients included in the analysis. Box-and-whisker plots show median, mean, and interquartile range, with whiskers indicating 1.5 × interquartile range with outliers omitted. Significance of linear correlations were assessed using the significance of the correlation coefficient when there were at least 10 data points.

In temporal analyses (i.e., peri-ripple time histograms), p-values were corrected across bins and all channels. To compute p-values using randomization tests, the observed test statistic (e.g., events per bin) was compared to the null distribution of test statistics. Null distributions were randomly selected from the same epochs using 200 iterations. The p-value was computed as the proportion of null test statistics that were equal to or greater/less than the observed test statistic. Randomization tests were one-sided according to whether the observed test statistic was greater than or less than the mean of the null test statistics. Order preferences (e.g., of ripples between channels) were assessed using a two-sided binomial test with an expected probability of 0.5. To determine if a circular distribution was non-uniform, the Hodges-Ajne test was used. To determine if two circular distributions had different circular means, a Watson-Williams multi-sample test was used. To test if co-rippling between two particular cortical sites made it more likely that additional cortical sites co-rippled, we computed a χ^2 test of proportions for all possible groups of three cortical channels under the null hypothesis that the co-occurrence of channel A and B has no relation to the co-occurrence of A and C. Each table was made from the number of ripples in A that co-occurred with a ripple in B only, or C only, or both, or neither, where A occurring with B or not B are the 2 rows, and A occurring with C or not C are the 2 columns.

In the paired-associates memory analysis, chance ripple occurrences (or co-occurrences) were computed for each trial as the average of 200 random shuffles per channel (pair) within ±3s from recall onset. Only trials where there was a successful recall (of the same word pair) in both the immediate and ~60s delayed conditions were included. Linear mixed-effects models were performed with the patient as the random effect, as follows:

$$\textit{(co-)ripples} \sim \textit{condition} + (1 \mid \textit{patient}) \quad (1)$$

Where *(co-)ripples* was the dependent variable computed as the average ripple rate (or co-ripple rate; minimum of 25ms overlap for each co-ripple) within 150-300ms following the stimulus cue preceding successful recall onset across trials, with the value for each trial as the average across channels, *condition* was 1) immediate recall or chance, 2) delayed recall or chance, 3) immediate recall or delayed recall (as a

ratio of observed over chance), or 4) successful recall or unsuccessful recall (as a ratio of observed over chance).

Linear mixed-effects models with the same structure as the one described above, with the patient as a random effect, were used to evaluate channel pair co-ripple metrics (co-occurrence probabilities, PLV modulations, and proportion of pairs with significant PLV modulations) with respect to fiber tract distance.

Differences in co-ripple phase-lag preferences between nights was assessed using the Watson-Williams multi-sample test for equal means. To test if unit spiking increase during ripples, a two-sample two-sided *t*-test was used to compare the spike counts during ripples vs. the spike counts during baseline periods selected in between ripples, which were matched in number and duration to the ripples. Ripple phase-modulations of spiking for each unit with at least 30 spikes during local ripples was assessed by comparing counts within $0 \pm \pi/2$ vs. $\pi \pm \pi/2$, with an expected value of 0.5.

Data availability

The de-identified raw data that support the findings of this study are available from the corresponding authors upon reasonable request provided that the data sharing agreement and patient consent permit that sharing.

Code availability

The code that support the findings of this study are available from the corresponding authors upon reasonable request.

Supplementary Information:

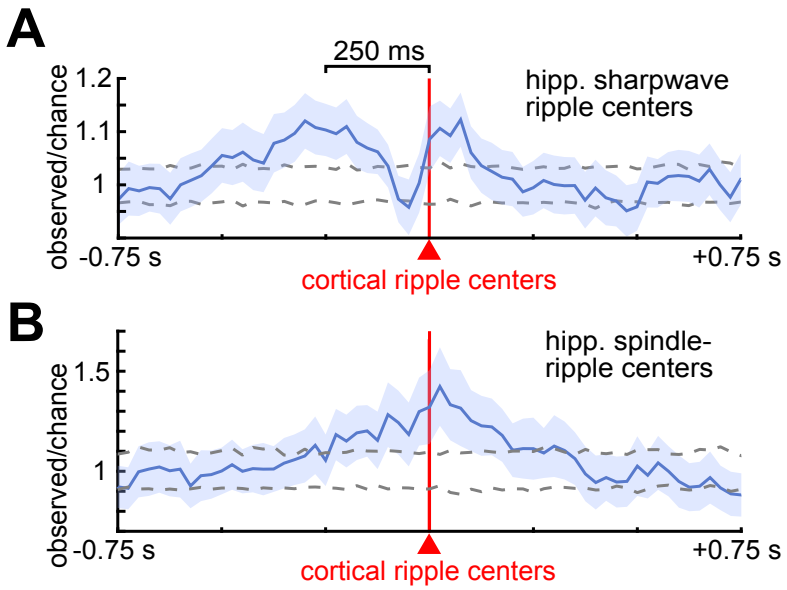

Supplementary Fig. 3.1. Hippocampal sharpwave ripples precede and spindle ripples coincide with cortical ripples. (**A-B**) Time delays from cortical to hippocampal sharpwave-ripples (**A**; *N*=91/461 significant channel pairs) and spindle-ripples (**B**; *N*=56/461 significant channel pairs) (**B**) during NREM sleep. Average is across significant channel pairs. Error shows SEM.

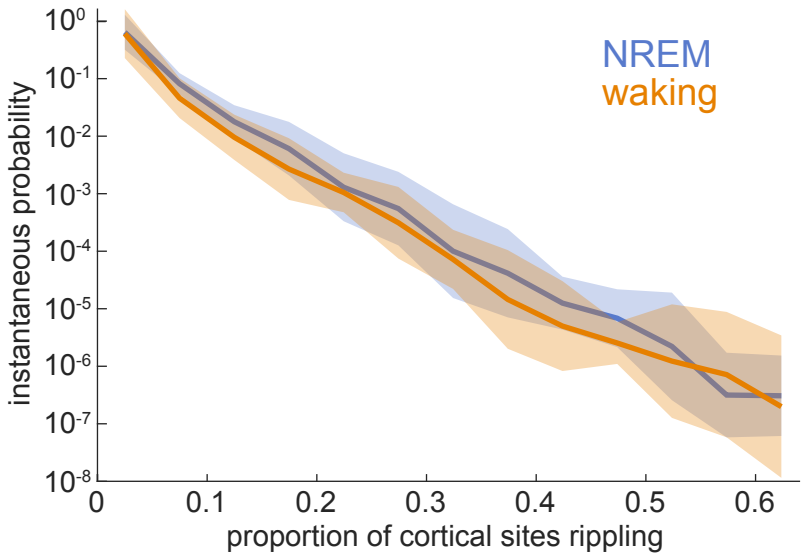

Supplementary Fig. 3.2. Instantaneous probabilities of the proportions of sites rippling. Mean log-probability of the proportion of channels that are rippling at any given time during NREM or waking (*N*=273 channels from patients S1-17). Note that random co-rippling would be expected to be greater during NREM because of the greater ripple density. However, the instantaneous probabilities are similar when larger proportions of sites co-rippling during NREM compared to waking. Thus the similar curves shown here implies a relatively greater increase over chance during waking, as shown in Fig. 3.2D. Data are binned in 0.05 increments. Error shows SEM.

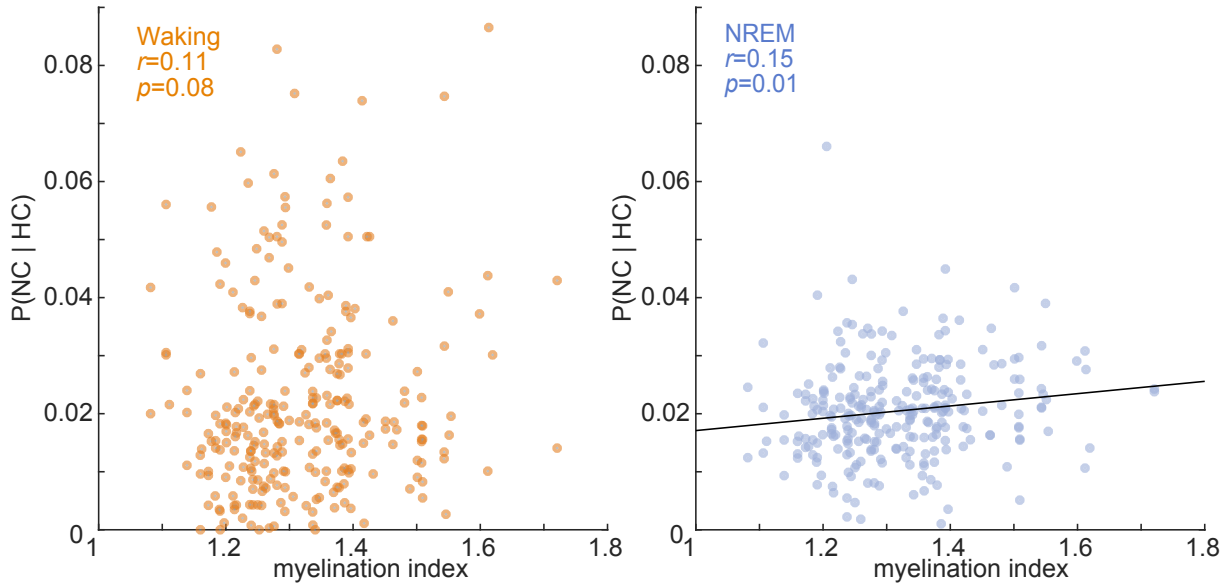

Supplementary Fig. 3.3. Hippocampo-cortical ripple co-occurrence as a function of cortical myelination index. Values are channel pair averages (each point is the average across pairs when there were multiple hippocampal channels in a patient) of the probability of a cortical ripple given a hippocampal ripple as a function of the cortical parcel myelination index (Rosen et al., 2021) (*N*=273). Co-occurrence required a minimum of 25ms overlap. HC=hippocampus, NC=neocortex.

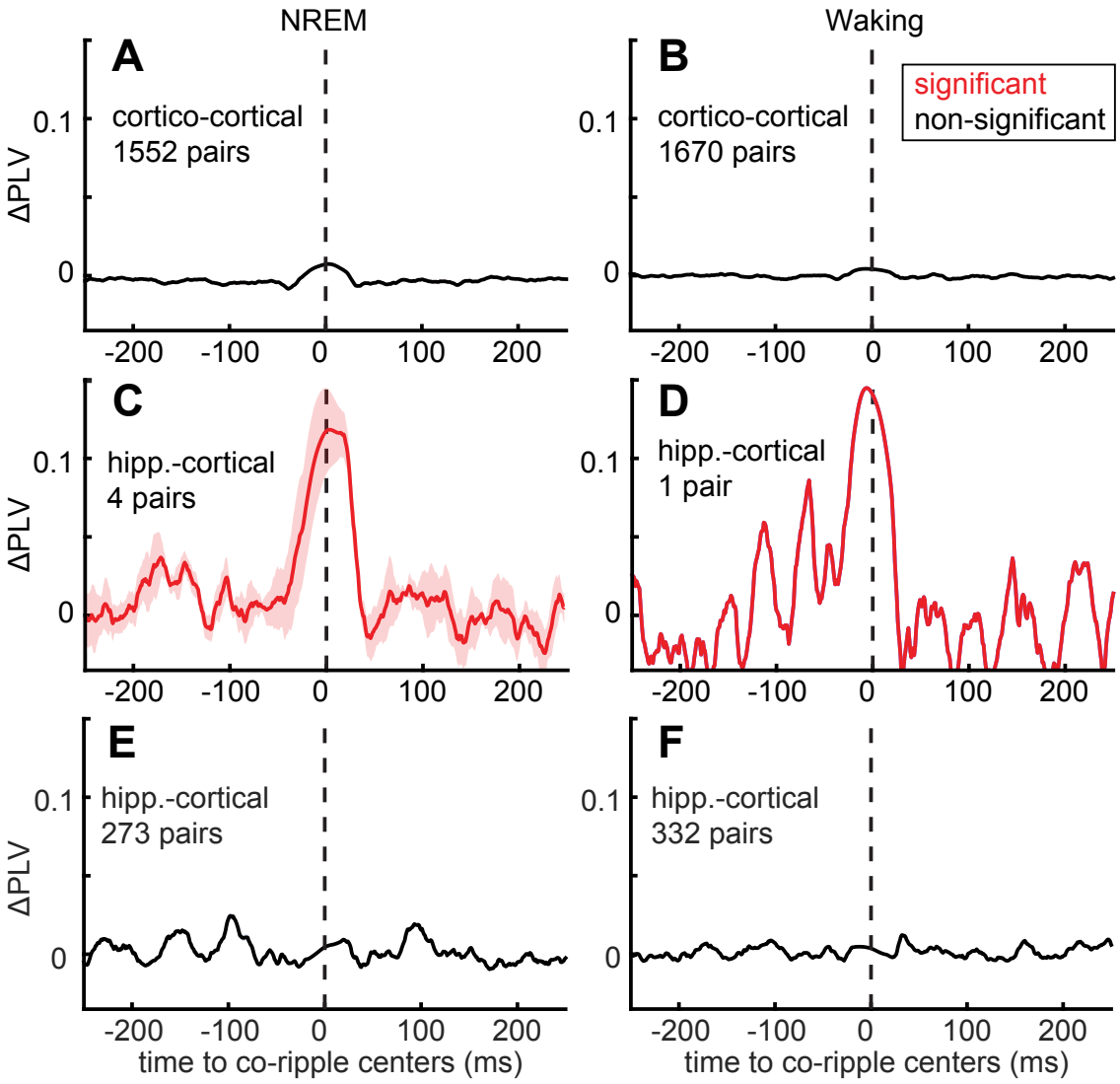

Supplementary Fig. 3.4. Non-significant cortico-cortical and significant and non-significant hippocampo-cortical ripple phase-locking results. (A-B) Average non-significant PLV time-courses locked to co-occurring ripples at *t*=0 for cortico-cortical pairs that had at least 40 co-occurring ripples during NREM (**A**) and waking (**B**). **(C-D)** Same as (A-B) except for hippocampo-cortical pairs with significant PLV responses. All significant hippocampo-cortical channel pairs localized to hippocampus proper and cortex. **(E-F)** Same as (C-D) except for non-significant PLV time-courses. Shaded error shows SEM. PLV=phase-locking value.

Supplementary Tables:

Supplementary Table 3.1. Stereoelectroencephalography patient demographics and data characteristics. Channels are the bipolar channels included in the analyses. δ NREM / δ Waking reports the ratio of the mean of the delta (0.5-2Hz) analytic amplitude means across cortical channels during the NREM vs. waking epochs analyzed.

Patient	Age	Sex	Hand.	No. Cort. Ch.	No. Hipp. Ch.	NREM Dur. (hr)	Waking Dur. (hr)	δ NREM / δ Waking	Paired-associates task
S1	20	M	R	18 (L)	1 (L)	6.1	49.8	3.98	-
S2	58	F	R	22 (L)	2 (L)	23.7	23.8	2.35	-
S3	42	M	L	16 (3 L)	3 (2 L)	11.4	19.3	3.39	-
S4	18	F	L	15 (R)	2 (R)	2.7	2.2	3.02	-
S5	20	F	R	18 (7 L)	2 (R)	5.6	19.3	2.93	-
S6	22	M	LR	17 (L)	1 (L)	6.3	59.9	5.45	-
S7	30	F	R	13 (2 L)	1 (R)	20.5	76.7	4.46	-
S8	43	F	R	12 (L)	2 (L)	8.1	32.6	5.43	-
S9	16	M	R	16 (4 L)	1 (R)	16.3	4.8	2.50	-
S10	32	F	R	29 (3 L)	3 (1 L)	11.2	27.6	3.11	-
S11	21	F	L	8 (4 L)	3 (2 L)	16.0	52.6	3.04	-
S12	21	F	R	14 (13 L)	1 (L)	26.2	37.2	2.92	-
S13	29	F	R	15 (6 L)	2 (1 L)	8.6	24.6	3.75	-
S14	41	F	R	18 (R)	1 (R)	11.9	63.3	4.20	-
S15	24	M	R	21 (9 L)	1 (L)	11.8	11.6	3.27	-
S16	31	F	R	15 (7 L)	1 (L)	28.1	39.4	2.55	-
S17	21	M	R	6 (L)	1 (L)	11.3	18.9	1.41	-
S18	25	M	R	38 (R)	0	N/A	N/A	N/A	✓
S19	32	M	L	21 (R)	8 (R)	N/A	N/A	N/A	✓
S20	34	M	R	22 (20 L)	0	N/A	N/A	N/A	✓
S21	38	F	R	21 (13 L)	0	N/A	N/A	N/A	✓
S22	23	M	R	28 (14 L)	16 (8 L)	N/A	N/A	N/A	✓

Supplementary Table 3.2. Cortical ripple coupling with cortical or hippocampal ripples in interictal-free channels. While the coupling analyses presented in the main text were performed between non-epileptogenic sites, during periods that did not exhibit frequent interictal spikes or artifacts(Jiang et al., 2019c), and with ripples that were not contaminated with interictal spikes or artifacts, additional analyses were run on a subset of hippocampal (*N*=5 channels from patients S4,6,9,17) and cortical channels (*N*=232 channels from patients S1-17) that did not have interictal spikes. These results demonstrate that cortico-cortical and hippocampo-cortical ripple coupling during both NREM and waking is present in the cases when both sites are free of interictal spikes. Numbers in parentheses are channel pair counts. *P*-values were FDR-corrected across channel pairs and bins. SSR=sleep spindle-ripple, SWR=sharpwave-ripple.

Ripple | Ripple	Significant Modulation	
	NREM	Waking
Cort-R | Cort-R	98.90% (3246/3282)	97.99% (3216/3282)
Hipp-R | Cort-R	26.78% (15/56)	64.28% (36/56)

Supplementary Table 3.3. Percent of channel-triplets where the number of triple co-occurrences significantly exceeded those that would be expected given the number of double co-occurrences of the constituent channel pairs. To test if the co-rippling between two particular cortical sites makes it more likely that other cortical sites will participate, we computed a χ^2 test of proportions for all possible groups of three cortical channels under the null hypothesis that the co-occurrence of channel A and B has no relation to the co-occurrence of A and C. *P*-values were FDR-corrected across channels for each patient. Error is SD.

Patient	% Significant	
	NREM	Waking
S1	9.7%	65.3%
S2	58.5%	60.6%
S3	12.3%	6.8%
S4	1.5%	0.4%
S5	1.1%	17.9%
S6	19.7%	46.5%
S7	4.9%	40.2%
S8	1.8%	96.8%
S9	23.4%	4.5%
S10	7.6%	80%
S11	0%	66.1%
S12	17.3%	5.2%
S13	5.9%	50.8%
S14	29.8%	74.3%
S15	17.4%	17.8%
S16	29.5%	22.2%
S17	0%	4.8%
Average	14.1±15.2%	38.8±31.2%

Supplementary Table 3.4. Paired-associates memory task performance for individual patients. Values indicate successful recall counts divided by total recall cues and average time from recall cue presentation to successful recall onset. Word pair recall was considered successful when the second word was correctly stated aloud following the visual and auditory presentation of the first word. Immediate recall was assessed immediately following the presentation of the word pair to be learned and delayed recall was after ~60s.

Patient	Immediate Recall		Delayed Recall	
	Accuracy	Time to Recall (s)	Accuracy	Time to Recall
S18	150/150	1.18±0.14	139/150	1.47±0.45
S19	157/160	1.35±0.13	66/160	1.82±0.66
S20	86/104	0.95±0.15	33/104	2.57±0.60
S21	158/160	1.07±0.23	103/160	1.76±0.66
S22	147/160	1.10±0.21	24/160	2.19±0.73

Supplementary Table 3.5. Significant cortico-cortical and hippocampo-cortical ripple PLVs. Channel pairs that had ≥40 co-occurring ripples with ≥25ms overlap were used to compute the PLVs and test for significant modulations. Signif. PLV / co-occurring reports the percent of the channels with ≥40 co-occurring ripples that had significant PLVs. Sig. PLV / all reports the percent of all channels (no minimum co-occurrence requirement) that had significant PLVs. Results are for patients S1-17. *P*-values were computed using a randomization test (200 shuffles/channel pair, 5ms bins within ±50ms relative to ripple temporal centers), and were FDR-corrected for multiple bins and channel pairs, and at least 2 consecutive bins with post-FDR $p<0.05$ were required for a pair to be significant.

Channel pair type	No. Channel Pairs	State	>40 Co-occurring Ripples	Signif. PLV / Co-occurring	Signif. PLV / All pairs
Cort ↔ Cort	2275	Sleep	2106	26.3% (554/2106)	24.4% (554/2275)
		Waking	1939	13.9% (269/1939)	11.8% (269/2275)
Hipp ↔ Cort	461	Sleep	277	1.4% (4/277)	0.9% (4/461)
		Waking	333	0.3% (1/333)	0.2% (1/461)

Supplementary Table 3.6. Single unit characteristics and patient demographics. Errors are standard deviations. IN=putative interneuron, PY=putative pyramidal.

Utah Array Patient Demographics							
Patient	Age	Sex	Handedness	Array Implantation Location		Probe Length (mm)	NREM Duration (min)
U1	51	F	R	Left middle temporal gyrus		1.0	200
U2	31	M	L	Left superior temporal gyrus		1.5	132
U3	47	M	R	Right middle temporal gyrus		1.5	120
Single Unit Characteristics							
Unit Type	No. Units	No. Spikes	Valley-to-Peak Amplitude (μV)	Spike Rate (Hz)	Valley-to-Peak Width (ms)	Half-Peak Width (ms)	Bursting Index
PY	142	318386	89.57±59.46	0.19±0.17	0.49±0.06	0.61±0.04	0.05±0.03
IN	38	772769	42.26±26.11	1.73±1.72	0.30±0.05	0.35±0.05	0.01±0.02

Chapter 3, in full, is a reprint of the material as it has been written in a manuscript submitted for publication: Dickey CW, Verzhbinsky IA, Jiang X, Rosen BQ, Kajfez S, Stedelin B, Shih JJ, Ben-Haim S, Raslan AM, Eskandar EN, Gonzalez-Martinez J, Cash SS, Halgren E. Widespread ripples synchronize human cortical activity during sleep, waking, and memory recall. Preprint available at *bioRxiv*. 2021. doi:10.1101/2021.02.23.432582.

Chapter 4: Conclusions

In conclusion, using human intracranial macro- and micro-electrode recordings, I have shown how cortical and hippocampal waves and associated single unit spiking are coordinated to provide essential conditions for memory in humans.

In Chapter 1, I showed that sleep spindles – recorded from granular/supragranular layers of human lateral temporal cortex – are associated with tonic and phase-locked increases in single unit spiking, leading to co-firing between units with short delays optimal for spike-timing-dependent plasticity (STDP). Critical to a possible role in memory consolidation, this increase in co-firing was greatest when spindles occurred on the down-to-upstate transition. Co-firing, spindle co-occurrence, and spindle coherence were greatest within about 2 mm. Crucially, increased co-firing between units on different contacts depended on high spindle coherence between those contacts. Spindles propagated at ~0.28 m/s, consistent with local travel via unmyelinated conduction, with multiple propagation patterns associated with distinct co-firing sequences. Thus, spindles generate necessary conditions for dynamic patterns of STDP during human non-rapid eye movement (NREM) sleep.

In Chapter 2, I demonstrated that the human cortex generates ripples (~70 ms long ~80 Hz oscillations) during NREM sleep, in addition to waking. Ripples had similar characteristics (occurrence rate, amplitude, frequency, and duration) in all cortical areas sampled, including all lobes of both hemispheres, as well as the hippocampus, during both NREM sleep and waking, with the exception of associated very-high-frequency activity that was stronger during waking. I showed that during NREM sleep, cortical ripples are generated on the down-to-upstate transition during spindles, and that single unit-firing is phase-locked to cortical ripples, leading to increased co-firing within the window of STDP. Thus, cortical ripples may have a synergistic role with spindles to facilitate STDP. Furthermore, I demonstrated that cortical ripples are linked to spatiotemporal activity patterns during NREM sleep that ‘replay’ from the previous waking period. These results show that cortical ripples provide the conditions for consolidation during NREM sleep in humans.

In Chapter 3, I showed that cortical ripples co-occur and phase-synchronize across the cortex, with little decay up to very long distances (25 cm). Ripple co-occurrences were enhanced preceding successful delayed memory recall, supporting the hypothesis that cortico-cortical co-rippling contributes to the reconstruction of declarative memories in humans. Furthermore, cortical ripples, which were associated with tonically increased and phase-coupled cell-firing, had increased very-high-frequency activity correlations between widespread areas, suggesting facilitated information exchange. Thus, cortical ripples appear to possess key properties that are necessary for the binding of information across sites for memory and possibly cognition in general.

References

Andrillon, T., Nir, Y., Staba, R. J., Ferrarelli, F., Cirelli, C., Tononi, G., & Fried, I. (2011, Dec 7). Sleep spindles in humans: insights from intracranial EEG and unit recordings. *J Neurosci, 31*(49), 17821-17834. 10.1523/JNEUROSCI.2604-11.2011

Axmacher, N., Elger, C. E., & Fell, J. (2008). Ripples in the medial temporal lobe are relevant for human memory consolidation. *Brain, 131*(7), 1806-1817.

Azevedo, F. A., Carvalho, L. R., Grinberg, L. T., Farfel, J. M., Ferretti, R. E., Leite, R. E., Jacob Filho, W., Lent, R., & Herculano-Houzel, S. (2009, Apr 10). Equal numbers of neuronal and nonneuronal cells make the human brain an isometrically scaled-up primate brain. *J Comp Neurol, 513*(5), 532-541. 10.1002/cne.21974

Barthó, P., Hirase, H., Monconduit, L., Zugaro, M., Harris, K. D., & Buzsáki, G. (2004, Jul). Characterization of neocortical principal cells and interneurons by network interactions and extracellular features. *J Neurophysiol, 92*(1), 600-608. 10.1152/jn.01170.2003

Bartos, M., Vida, I., Frotscher, M., Meyer, A., Monyer, H., Geiger, J. R., & Jonas, P. (2002). Fast synaptic inhibition promotes synchronized gamma oscillations in hippocampal interneuron networks. *Proceedings of the National Academy of Science, 99*(20), 13222-13227.

Bazhenov, M., Rulkov, N. F., & Timofeev, I. (2008, Jul 16). Effect of synaptic connectivity on long-range synchronization of fast cortical oscillations. *J Neurophysiol*.

Behrens, T. E. J., Berg, H. J., Jbabdi, S., Rushworth, M. F. S., & Woolrich, M. W. (2007, 2007/01/01/). Probabilistic diffusion tractography with multiple fibre orientations: What can we gain? *NeuroImage, 34*(1), 144-155. 10.1016/j.neuroimage.2006.09.018

Benjamini, Y., & Hochberg, Y. (1995). Controlling the False Discovery Rate: A Practical and Powerful Approach to Multiple Testing. *Journal of the Royal Statistical Society. Series B (Methodological), 57*(1), 289-300.

Berens, P. (2009). CircStat: a MATLAB toolbox for circular statistics. *J Stat Softw, 31*(10), 1-21.

Bettinardi, R. G. (2020). (https://www.mathworks.com/matlabcentral/fileexchange/62957-computecohen_d-x1-x2-varargin). *MATLAB Central File Exchange*.

Bragin, A., Engel, J., Jr., Wilson, C. L., Fried, I., & Buzsaki, G. (1999). High-frequency oscillations in human brain. *Hippocampus, 9*(2), 137-142.

Buzsaki, G. (2015). Hippocampal sharp wave-ripple: A cognitive biomarker for episodic memory and planning. *Hippocampus, 25*(10), 1073-1188. doi:10.1002/hipo.22488

Buzsáki, G. (1998). Memory consolidation during sleep: a neurophysiological perspective. *J Sleep Res, 7 Suppl 1*, 17-23. 10.1046/j.1365-2869.7.s1.3.x

Buzsáki, G., & Wang, X. J. (2012). Mechanisms of gamma oscillations. *Annu Rev Neurosci, 35*, 203-225. 10.1146/annurev-neuro-062111-150444

Calabrese, A., & Paninski, L. (2011, Mar 15). Kalman filter mixture model for spike sorting of non-stationary data. *J Neurosci Methods, 196*(1), 159-169. 10.1016/j.jneumeth.2010.12.002

Chan, A. M., Dykstra, A. R., Jayaram, V., Leonard, M. K., Travis, K. E., Gygi, B., Baker, J. M., Eskandar, E., Hochberg, L. R., Halgren, E., & Cash, S. S. (2014, Oct). Speech-specific tuning of neurons in human superior temporal gyrus. *Cereb Cortex, 24*(10), 2679-2693. 10.1093/cercor/bht127

Clemens, Z., Molle, M., Eross, L., Barsi, P., Halasz, P., & Born, J. (2007, Nov). Temporal coupling of parahippocampal ripples, sleep spindles and slow oscillations in humans. *Brain, 130*(Pt 11), 2868-2878. 10.1093/brain/awm146

Clopath, C. (2012, Jun). Synaptic consolidation: an approach to long-term learning. *Cogn Neurodyn, 6*(3), 251-257. 10.1007/s11571-011-9177-6

Contreras, D., Destexhe, A., Sejnowski, T. J., & Steriade, M. (1997, Feb 1). Spatiotemporal patterns of spindle oscillations in cortex and thalamus. *J Neurosci, 17*(3), 1179-1196. 10.1523/jneurosci.17-03-01179.1997

Cox, R., Hofman, W. F., & Talamini, L. M. (2012). Involvement of spindles in memory consolidation is slow wave sleep-specific. *Learn Mem, 19*(7), 264-267. 10.1101/lm.026252.112

Cruikshank, S. J., Lewis, T. J., & Connors, B. W. (2007, Apr). Synaptic basis for intense thalamocortical activation of feedforward inhibitory cells in neocortex. *Nat Neurosci, 10*(4), 462-468. 10.1038/nn1861

Csercsa, R., Dombovari, B., Fabo, D., Wittner, L., Eross, L., Entz, L., Solyom, A., Rasonyi, G., Szucs, A., Kelemen, A., Jakus, R., Juhos, V., Grand, L., Magony, A., Halasz, P., Freund, T. F., Magloczky, Z., Cash, S. S., Papp, L., Karmos, G., Halgren, E., & Ulbert, I. (2010, Sep). Laminar analysis of slow wave activity in humans. *Brain, 133*(9), 2814-2829. 10.1093/brain/awq169

Cutts, C. S., & Eglen, S. J. (2014, Oct 22). Detecting pairwise correlations in spike trains: an objective comparison of methods and application to the study of retinal waves. *J Neurosci, 34*(43), 14288-14303. 10.1523/jneurosci.2767-14.2014

Davis, Z. W., Muller, L., Martinez-Trujillo, J., Sejnowski, T., & Reynolds, J. H. (2020, Oct 7). Spontaneous travelling cortical waves gate perception in behaving primates. *Nature*. 10.1038/s41586-020-2802-y

De Gennaro, L., & Ferrara, M. (2003, Oct). Sleep spindles: an overview. *Sleep Med Rev, 7*(5), 423-440. S1087079202902522

DeFelipe, J., Alonso-Nanclares, L., & Arellano, J. I. (2002, Mar-Jun). Microstructure of the neocortex: comparative aspects. *J Neurocytol, 31*(3-5), 299-316. 10.1023/a:1024130211265

Dehghani, N., Cash, S. S., & Halgren, E. (2011, Dec). Emergence of synchronous EEG spindles from asynchronous MEG spindles [Research Support, N.I.H., Extramural]. *Hum Brain Mapp, 32*(12), 2217-2227. 10.1002/hbm.21183

Dehghani, N., Peyrache, A., Telenczuk, B., Le Van Quyen, M., Halgren, E., Cash, S. S., Hatsopoulos, N. G., & Destexhe, A. (2016). Dynamic balance of excitation and inhibition in human and monkey neocortex. *Scientific reports, 6*.

Delevich, K., Tucciarone, J., Huang, Z. J., & Li, B. (2015, Apr 8). The mediodorsal thalamus drives feedforward inhibition in the anterior cingulate cortex via parvalbumin interneurons. *J Neurosci, 35*(14), 5743-5753. 10.1523/jneurosci.4565-14.2015

Delorme, A., & Makeig, S. (2004). EEGLAB: an open source toolbox for analysis of single-trial EEG dynamics including independent component analysis. *Journal of Neuroscience Methods, 134*, 9-21.

Desikan, R. S., Segonne, F., Fischl, B., Quinn, B. T., Dickerson, B. C., Blacker, D., Buckner, R. L., Dale, A. M., Maguire, R. P., Hyman, B. T., Albert, M. S., & Killiany, R. J. (2006, Jul 1). An automated labeling system for subdividing the human cerebral cortex on MRI scans into gyral based regions of interest. *NeuroImage, 31*(3), 968-980.

Destexhe, A., & Sejnowski, T. J. (2003, Oct). Interactions between membrane conductances underlying thalamocortical slow-wave oscillations. *Physiol Rev, 83*(4), 1401-1453. 10.1152/physrev.00012.2003

Destrieux, C., Fischl, B., Dale, A., & Halgren, E. (2010, Oct 15). Automatic parcellation of human cortical gyri and sulci using standard anatomical nomenclature. *Neuroimage, 53*(1), 1-15. 10.1016/j.neuroimage.2010.06.010

Dickey, C. W., Sargsyan, A., Madsen, J. R., Eskandar, E. N., Cash, S. S., & Halgren, E. (2021a, 2021/02/15). Travelling spindles create necessary conditions for spike-timing-dependent plasticity in humans. *Nat Commun, 12*(1), 1027. 10.1038/s41467-021-21298-x

Dickey, C. W., Verzhbinsky, I. A., Jiang, X., Rosen, B. Q., Kajfez, S., Eskandar, E. N., Gonzalez-Martinez, J., Cash, S. S., & Halgren, E. (2021b). Cortical ripples provide the conditions for consolidation during NREM sleep in humans. *bioRxiv (in process)*.

Diekelmann, S., & Born, J. (2010, Feb). The memory function of sleep. *Nat Rev Neurosci, 11*(2), 114-126. 10.1038/nrn2762

Donoho, D. L., & Johnstone, I. M. (1994). Ideal spatial adaptation by wavelet shrinkage. *Biometrika, 81*(3), 425-455. 10.1093/biomet/81.3.425

Ego-Stengel, V., & Wilson, M. A. (2009, Jan). Disruption of ripple-associated hippocampal activity during rest impairs spatial learning in the rat. *Hippocampus, 20*(1), 1-10. 10.1002/hipo.20707

Eichenbaum, H. (2014, 2014/11/01). Time cells in the hippocampus: a new dimension for mapping memories. *Nature Reviews Neuroscience, 15*(11), 732-744. 10.1038/nrn3827

Eichenlaub, J.-B., Jarosiewicz, B., Saab, J., Franco, B., Kelemen, J., Halgren, E., Hochberg, L. R., & Cash, S. S. (2020). Replay of Learned Neural Firing Sequences during Rest in Human Motor Cortex. *Cell reports, 31*(5), 107581.

Fedorov, A., Beichel, R., Kalpathy-Cramer, J., Finet, J., Fillion-Robin, J. C., Pujol, S., Bauer, C., Jennings, D., Fennessy, F., Sonka, M., Buatti, J., Aylward, S., Miller, J. V., Pieper, S., & Kikinis,

R. (2012, Nov). 3D Slicer as an image computing platform for the Quantitative Imaging Network. *Magn Reson Imaging, 30*(9), 1323-1341. 10.1016/j.mri.2012.05.001

Feldman, D. E. (2012). The spike-timing dependence of plasticity. *Neuron, 75*(4), 556-571.

Felleman, D. J., & VanEssen, D. C. (1991). Distributed hierarchical processing in the primate cerebral cortex. *Cerebral Cortex, 1*, 1-47.

Fernández, E., Greger, B., House, P. A., Aranda, I., Botella, C., Albisua, J., Soto-Sánchez, C., Alfaro, A., & Normann, R. A. (2014, 2014-July-21). Acute human brain responses to intracortical microelectrode arrays: challenges and future prospects [Hypothesis & Theory]. *Frontiers in Neuroengineering, 7*(24). 10.3389/fneng.2014.00024

Fernandez, L. M. J., & Lüthi, A. (2020, Apr 1). Sleep Spindles: Mechanisms and Functions. *Physiol Rev, 100*(2), 805-868. 10.1152/physrev.00042.2018

Fischl, B. (2012). FreeSurfer. *NeuroImage, 62*(2), 774-781.

Fischl, B., Sereno, M. I., Tootell, R. B., & Dale, A. M. (1999). High-resolution intersubject averaging and a coordinate system for the cortical surface. *Hum Brain Mapp, 8*(4), 272-284.

Fischl, B., Van Der Kouwe, A., Destrieux, C., Halgren, E., Segonne, F., Salat, D. H., Busa, E., Seidman, L. J., Goldstein, J., Kennedy, D., Caviness, V., Makris, N., Rosen, B., & Dale, A. M. (2004, Jan). Automatically parcellating the human cerebral cortex. *Cereb Cortex, 14*(1), 11-22.

Fries, P. (2009). Neuronal Gamma-Band Synchronization as a Fundamental Process in Cortical Computation. *Annual Review of Neuroscience, 32*(1), 209-224. 10.1146/annurev.neuro.051508.135603

Gabadinho, A., Ritschard, G., Mueller, N. S., & Studer, M. (2011). Analyzing and visualizing state sequences in R with TraMineR. *Journal of Statistical Software, 40*(4), 1-37.

Gelinas, J. N., Khodagholy, D., Thesen, T., Devinsky, O., & Buzsáki, G. (2016, Jun). Interictal epileptiform discharges induce hippocampal-cortical coupling in temporal lobe epilepsy. *Nat Med, 22*(6), 641-648. 10.1038/nm.4084

Glasser, M. F., Coalson, T. S., Robinson, E. C., Hacker, C. D., Harwell, J., Yacoub, E., Ugurbil, K., Andersson, J., Beckmann, C. F., & Jenkinson, M. (2016). A multi-modal parcellation of human cerebral cortex. *Nature*.

Glasser, M. F., & Van Essen, D. C. (2011, Aug 10). Mapping human cortical areas in vivo based on myelin content as revealed by T1- and T2-weighted MRI. *J Neurosci, 31*(32), 11597-11616. 10.1523/JNEUROSCI.2180-11.2011

Gonzalez, C. E., Mak-McCully, R. A., Rosen, B. Q., Cash, S. S., Chauvel, P. Y., Bastuji, H., Rey, M., & Halgren, E. (2018, Nov 14). Theta Bursts Precede, and Spindles Follow, Cortical and Thalamic Downstates in Human NREM Sleep. *J Neurosci, 38*(46), 9989-10001. 10.1523/jneurosci.0476-18.2018

Gray, C. M., Konig, P., Engel, A. K., & Singer, W. (1989, Mar 23). Oscillatory responses in cat visual cortex exhibit inter-columnar synchronization which reflects global stimulus properties. *Nature, 338*(6213), 334-337.

Grenier, F., Timofeev, I., & Steriade, M. (2001). Focal synchronization of ripples (80-200 Hz) in neocortex and their neuronal correlates. *J Neurophysiol, 86*(4), 1884-1898.

Hagler, D. J., Jr., Ulbert, I., Wittner, L., Erőss, L., Madsen, J. R., Devinsky, O., Doyle, W., Fabó, D., Cash, S. S., & Halgren, E. (2018, Mar 21). Heterogeneous Origins of Human Sleep Spindles in Different Cortical Layers. *J Neurosci, 38*(12), 3013-3025. 10.1523/jneurosci.2241-17.2018

Halassa, M. M., Siegle, J. H., Ritt, J. T., Ting, J. T., Feng, G., & Moore, C. I. (2011, Jul 24). Selective optical drive of thalamic reticular nucleus generates thalamic bursts and cortical spindles. *Nat Neurosci, 14*(9), 1118-1120. 10.1038/nn.2880

Halgren, E. (1990). Insights from evoked potentials into the neuropsychological mechanisms of reading. In A. Scheibel & A. Weschsler (Eds.), *Neurobiology of Cognition* (pp. 103-150). Guilford.

Halgren, M., Fabó, D., Ulbert, I., Madsen, J. R., Erőss, L., Doyle, W. K., Devinsky, O., Schomer, D., Cash, S. S., & Halgren, E. (2018, Feb 1). Superficial Slow Rhythms Integrate Cortical Processing in Humans. *Sci Rep, 8*(1), 2055. 10.1038/s41598-018-20662-0

Halgren, M., Ulbert, I., Bastuji, H., Fabó, D., Erőss, L., Rey, M., Devinsky, O., Doyle, W. K., Mak-McCully, R., Halgren, E., Wittner, L., Chauvel, P., Heit, G., Eskandar, E., Mandell, A., & Cash, S. S. (2019, Nov 19). The generation and propagation of the human alpha rhythm. *Proc Natl Acad Sci U S A, 116*(47), 23772-23782. 10.1073/pnas.1913092116

Hartigan, J. A., & Hartigan, P. M. (1985, 1985/03). The Dip Test of Unimodality. *Ann. Statist., 13*(1), 70-84. 10.1214/aos/1176346577

Hirsch, J. A., & Gilbert, C. D. (1991, Jun). Synaptic physiology of horizontal connections in the cat's visual cortex. *J Neurosci, 11*(6), 1800-1809. 10.1523/jneurosci.11-06-01800.1991

Iglesias, J. E., Augustinack, J. C., Nguyen, K., Player, C. M., Player, A., Wright, M., Roy, N., Frosch, M. P., McKee, A. C., Wald, L. L., Fischl, B., & Van Leemput, K. (2015, Jul 15). A computational atlas of the hippocampal formation using ex vivo, ultra-high resolution MRI: Application to adaptive segmentation of in vivo MRI. *NeuroImage, 115*, 117-137. 10.1016/j.neuroimage.2015.04.042

Izhikevich, E. M., & Kuramoto, Y. (2006). Weakly Coupled Oscillators. In J.-P. Françoise, G. L. Naber, & T. S. Tsun (Eds.), *Encyclopedia of Mathematical Physics* (pp. 448-453). Academic Press. 10.1016/B0-12-512666-2/00106-1

Ji, D., & Wilson, M. A. (2007, Jan). Coordinated memory replay in the visual cortex and hippocampus during sleep. *Nat Neurosci, 10*(1), 100-107. 10.1038/nn1825

Jiang, X., Gonzalez-Martinez, J., & Halgren, E. (2019a). Coordination of Human Hippocampal Sharpwave Ripples during NREM Sleep with Cortical Theta Bursts, Spindles, Downstates, and Upstates. *The Journal of Neuroscience, 39*(44), 8744-8761. 10.1523/jneurosci.2857-18.2019

Jiang, X., Gonzalez-Martinez, J., & Halgren, E. (2019b). Posterior hippocampal spindle-ripples co-occur with neocortical theta-bursts and down-upstates, and phase-lock with parietal spindles during NREM sleep in humans. *The Journal of Neuroscience*, 2858-2818. 10.1523/jneurosci.2858-18.2019

Jiang, X., Gonzalez-Martinez, J., Cash, S. S., Chauvel, P., Gale, J., & Halgren, E. (2019c). Improved identification and differentiation from epileptiform activity of human hippocampal sharp wave ripples during NREM sleep. *Hippocampus*.

Jiang, X., Shamie, I., K. Doyle, W., Friedman, D., Dugan, P., Devinsky, O., Eskandar, E., Cash, S. S., Thesen, T., & Halgren, E. (2017, 2017/12/12). Replay of large-scale spatio-temporal patterns from waking during subsequent NREM sleep in human cortex. *Scientific reports, 7*(1), 17380. 10.1038/s41598-017-17469-w

Johnson, H., Harris, G., & Williams, K. (2007). BRAINSFit: mutual information rigid registrations of whole-brain 3D images, using the insight toolkit. *Insight J*.

Johnson, L. A., Euston, D. R., Tatsuno, M., & McNaughton, B. L. (2010, Feb 17). Stored-trace reactivation in rat prefrontal cortex is correlated with down-to-up state fluctuation density. *J Neurosci, 30*(7), 2650-2661. 10.1523/JNEUROSCI.1617-09.2010

Kalmbach, B. E., Buchin, A., Long, B., Close, J., Nandi, A., Miller, J. A., Bakken, T. E., Hodge, R. D., Chong, P., de Frates, R., Dai, K., Maltzer, Z., Nicovich, P. R., Keene, C. D., Silbergeld, D. L., Gwinn, R. P., Cobbs, C., Ko, A. L., Ojemann, J. G., Koch, C., Anastassiou, C. A., Lein, E. S., & Ting, J. T. (2018, Dec 5). h-Channels Contribute to Divergent Intrinsic Membrane Properties of Supragranular Pyramidal Neurons in Human versus Mouse Cerebral Cortex. *Neuron, 100*(5), 1194-1208.e1195. 10.1016/j.neuron.2018.10.012

Kamiński, J., Brzezicka, A., Mamelak, A. N., & Rutishauser, U. (2020, Apr 22). Combined Phase-Rate Coding by Persistently Active Neurons as a Mechanism for Maintaining Multiple Items in Working Memory in Humans. *Neuron, 106*(2), 256-264.e253. 10.1016/j.neuron.2020.01.032

Keller, C. J., Truccolo, W., Gale, J. T., Eskandar, E., Thesen, T., Carlson, C., Devinsky, O., Kuzniecky, R., Doyle, W. K., Madsen, J. R., Schomer, D. L., Mehta, A. D., Brown, E. N., Hochberg, L. R., Ulbert, I., Halgren, E., & Cash, S. S. (2010, Jun). Heterogeneous neuronal firing patterns during interictal epileptiform discharges in the human cortex. *Brain, 133*(Pt 6), 1668-1681. 10.1093/brain/awq112

Khodagholy, D., Gelinas, J. N., & Buzsáki, G. (2017). Learning-enhanced coupling between ripple oscillations in association cortices and hippocampus. *Science, 358*(6361), 369-372. 10.1126/science.aan6203

Klinzing, J. G., Niethard, N., & Born, J. (2019, Oct). Mechanisms of systems memory consolidation during sleep. *Nat Neurosci, 22*(10), 1598-1610. 10.1038/s41593-019-0467-3

Lachaux, J. P., Rodriguez, E., Martinerie, J., & Varela, F. J. (1999). Measuring phase synchrony in brain signals. *Hum Brain Mapp, 8*(4), 194-208.

Langfelder, P., Zhang, B., & Horvath, S. (2008, Mar 1). Defining clusters from a hierarchical cluster tree: the Dynamic Tree Cut package for R. *Bioinformatics, 24*(5), 719-720. 10.1093/bioinformatics/btm563

Latchoumane, C.-F. V., Ngo, H.-V. V., Born, J., & Shin, H.-S. (2017). Thalamic Spindles Promote Memory Formation during Sleep through Triple Phase-Locking of Cortical, Thalamic, and Hippocampal Rhythms. *Neuron, 95*(2), 424-435.e426. 10.1016/j.neuron.2017.06.025

Laurie. (2020). Compare two proportions (Chi-square) (https://www.mathworks.com/matlabcentral/fileexchange/45966-compare-two-proportions-chi-square). *MATLAB Central File Exchange*.

Le Van Quyen, M., Bragin, A., Staba, R., Crépon, B., Wilson, C. L., & Engel, J. (2008). Cell Type-Specific Firing during Ripple Oscillations in the Hippocampal Formation of Humans. *The Journal of Neuroscience, 28*(24), 6104-6110. 10.1523/jneurosci.0437-08.2008

Le Van Quyen, M., Muller, L. E., Telenczuk, B., Halgren, E., Cash, S., Hatsopoulos, N. G., Dehghani, N., & Destexhe, A. (2016). High-frequency oscillations in human and monkey neocortex during the wake–sleep cycle. *Proceedings of the National Academy of Sciences, 113*(33), 9363-9368.

Lohmann, H., & Rörig, B. (1994, Jun 22). Long-range horizontal connections between supragranular pyramidal cells in the extrastriate visual cortex of the rat. *J Comp Neurol, 344*(4), 543-558. 10.1002/cne.903440405

Maingret, N., Girardeau, G., Todorova, R., Goutierre, M., & Zugaro, M. (2016, Jul). Hippocampo-cortical coupling mediates memory consolidation during sleep. *Nat Neurosci, 19*(7), 959-964. 10.1038/nn.4304

Mak-McCully, R. A., Rolland, M., Sargsyan, A., Gonzalez, C., Magnin, M., Chauvel, P., Rey, M., Bastuji, H., & Halgren, E. (2017, May 25). Coordination of cortical and thalamic activity during non-REM sleep in humans. *Nat Commun, 8*, 15499. 10.1038/ncomms15499

Mak-McCully, R. A., Rosen, B. Q., Rolland, M., Regis, J., Bartolomei, F., Rey, M., Chauvel, P., Cash, S. S., & Halgren, E. (2015, Jul-Aug). Distribution, Amplitude, Incidence, Co-Occurrence, and Propagation of Human K-Complexes in Focal Transcortical Recordings(1,2,3). *eneuro, 2*(4). 10.1523/ENEURO.0028-15.2015

McClelland, J. L., McNaughton, B. L., & O'Reilly, R. C. (1995, Jul). Why there are complementary learning systems in the hippocampus and neocortex: insights from the successes and failures of connectionist models of learning and memory. *Psychol Rev, 102*(3), 419-457. 10.1037/0033-295x.102.3.419

McCormick, D. A., Connors, B. W., Lighthall, J. W., & Prince, D. A. (1985). Comparative electrophysiology of pyramidal and sparsely spiny stellate neurons of the neocortex. *J Neurophysiol, 54*(4), 782-806.

McCormick, D. A., McGinley, M. J., & Salkoff, D. B. (2015, Apr). Brain state dependent activity in the cortex and thalamus. *Curr Opin Neurobiol, 31*, 133-140. 10.1016/j.conb.2014.10.003

Mednick, S. C., McDevitt, E. A., Walsh, J. K., Wamsley, E., Paulus, M., Kanady, J. C., & Drummond, S. P. (2013, Mar 6). The critical role of sleep spindles in hippocampal-dependent memory: a pharmacology study. *J Neurosci, 33*(10), 4494-4504. 10.1523/jneurosci.3127-12.2013

Merker, B. (2013). The efference cascade, consciousness, and its self: naturalizing the first person pivot of action control. *Front Psychol, 4*, 501. 10.3389/fpsyg.2013.00501

Miller, J.-e. K., Ayzenshtat, I., Carrillo-Reid, L., & Yuste, R. (2014). Visual stimuli recruit intrinsically generated cortical ensembles. *Proceedings of the National Academy of Sciences, 111*(38), E4053-E4061.

Mohan, H., Verhoog, M. B., Doreswamy, K. K., Eyal, G., Aardse, R., Lodder, B. N., Goriounova, N. A., Asamoah, B., AB, B. B., Groot, C., van der Sluis, S., Testa-Silva, G., Obermayer, J., Boudewijns, Z. S., Narayanan, R. T., Baayen, J. C., Segev, I., Mansvelder, H. D., & de Kock, C. P. (2015, Dec). Dendritic and Axonal Architecture of Individual Pyramidal Neurons across Layers of Adult Human Neocortex. *Cereb Cortex, 25*(12), 4839-4853. 10.1093/cercor/bhv188

Mukamel, R., Gelbard, H., Arieli, A., Hasson, U., Fried, I., & Malach, R. (2005, Aug 5). Coupling between neuronal firing, field potentials, and FMRI in human auditory cortex. *Science, 309*(5736), 951-954. 10.1126/science.1110913

Muller, L., Chavane, F., Reynolds, J., & Sejnowski, T. J. (2018, May). Cortical travelling waves: mechanisms and computational principles. *Nat Rev Neurosci, 19*(5), 255-268. 10.1038/nrn.2018.20

Muller, L., Piantoni, G., Koller, D., Cash, S. S., Halgren, E., & Sejnowski, T. J. (2016, Nov 15). Rotating waves during human sleep spindles organize global patterns of activity that repeat precisely through the night. *Elife, 5*. 10.7554/eLife.17267

Müllner, D. (2013). fastcluster: Fast hierarchical, agglomerative clustering routines for R and Python. *Journal of Statistical Software, 53*(9), 1-18.

Murakoshi, T., Guo, J. Z., & Ichinose, T. (1993, Dec 12). Electrophysiological identification of horizontal synaptic connections in rat visual cortex in vitro. *Neurosci Lett, 163*(2), 211-214.

Niethard, N., Ngo, H. V., Ehrlich, I., & Born, J. (2018, Sep 25). Cortical circuit activity underlying sleep slow oscillations and spindles. *Proc Natl Acad Sci U S A, 115*(39), E9220-e9229. 10.1073/pnas.1805517115

Nitzan, N., McKenzie, S., Beed, P., English, D. F., Oldani, S., Tukker, J. J., Buzsáki, G., & Schmitz, D. (2020, 2020/04/23). Propagation of hippocampal ripples to the neocortex by way of a subiculum-retrosplenial pathway. *Nat Commun, 11*(1), 1947. 10.1038/s41467-020-15787-8

Norman, Y., Yeagle, E. M., Khuvis, S., Harel, M., Mehta, A. D., & Malach, R. (2019). Hippocampal sharp-wave ripples linked to visual episodic recollection in humans. *Science, 365*(6454), eaax1030.

Oostenveld, R., Fries, P., Maris, E., & Schoffelen, J. M. (2011). FieldTrip: Open source software for advanced analysis of MEG, EEG, and invasive electrophysiological data. *Comput Intell Neurosci, 2011*, 156869. 10.1155/2011/156869

Patel, J., Schomburg, E. W., Berényi, A., Fujisawa, S., & Buzsáki, G. (2013). Local Generation and Propagation of Ripples along the Septotemporal Axis of the Hippocampus. *The Journal of Neuroscience, 33*(43), 17029-17041. 10.1523/jneurosci.2036-13.2013

Peng, Y., Mittermaier, F. X., Planert, H., Schneider, U. C., Alle, H., & Geiger, J. R. P. (2019, Nov 19). High-throughput microcircuit analysis of individual human brains through next-generation multineuron patch-clamp. *eLife, 8*. 10.7554/eLife.48178

Peyrache, A., Battaglia, F. P., & Destexhe, A. (2011, Oct 11). Inhibition recruitment in prefrontal cortex during sleep spindles and gating of hippocampal inputs. *Proc Natl Acad Sci U S A, 108*(41), 17207-17212. 10.1073/pnas.1103612108

Peyrache, A., Dehghani, N., Eskandar, E. N., Madsen, J. R., Anderson, W. S., Donoghue, J. A., Hochberg, L. R., Halgren, E., Cash, S. S., & Destexhe, A. (2012, Jan 31). Spatiotemporal dynamics of neocortical excitation and inhibition during human sleep. *Proceedings of the National Academy of Science, 109*(5), 1731-1736. 10.1073/pnas.1109895109

Peyrache, A., Khamassi, M., Benchenane, K., Wiener, S. I., & Battaglia, F. P. (2009, Jul). Replay of rule-learning related neural patterns in the prefrontal cortex during sleep. *Nat Neurosci, 12*(7), 919-926. 10.1038/nn.2337

Piantoni, G., Halgren, E., & Cash, S. S. (2017, Feb 1). Spatiotemporal characteristics of sleep spindles depend on cortical location. *Neuroimage, 146*, 236-245. 10.1016/j.neuroimage.2016.11.010

Pouzat, C., Mazor, O., & Laurent, G. (2002, 2002/12/31/). Using noise signature to optimize spike-sorting and to assess neuronal classification quality. *Journal of Neuroscience Methods, 122*(1), 43-57. 10.1016/S0165-0270(02)00276-5

Rasch, B., & Born, J. (2013, Apr). About sleep's role in memory. *Physiol Rev, 93*(2), 681-766. 10.1152/physrev.00032.2012

Revonsuo, A., & Newman, J. (1999, 1999/06/01/). Binding and Consciousness. *Consciousness and Cognition, 8*(2), 123-127. 10.1006/ccog.1999.0393

Rosanova, M., & Ulrich, D. (2005, Oct 12). Pattern-specific associative long-term potentiation induced by a sleep spindle-related spike train. *J Neurosci, 25*(41), 9398-9405. 10.1523/jneurosci.2149-05.2005

Rosen, B. Q., & Halgren, E. (2021). A whole-cortex probabilistic diffusion tractography connectome. *eneuro*, ENEURO.0416-0420.2020. 10.1523/eneuro.0416-20.2020

Salinas, E., & Sejnowski, T. J. (2001, Aug). Correlated neuronal activity and the flow of neural information. *Nat Rev Neurosci, 2*(8), 539-550.

Seeman, S. C., Campagnola, L., Davoudian, P. A., Hoggarth, A., Hage, T. A., Bosma-Moody, A., Baker, C. A., Lee, J. H., Mihalas, S., Teeter, C., Ko, A. L., Ojemann, J. G., Gwinn, R. P., Silbergeld, D. L., Cobbs, C., Phillips, J., Lein, E., Murphy, G., Koch, C., Zeng, H., & Jarsky, T. (2018, Sep 26). Sparse recurrent excitatory connectivity in the microcircuit of the adult mouse and human cortex. *Elife, 7*. 10.7554/eLife.37349

Seibt, J., Richard, C. J., Sigl-Glöckner, J., Takahashi, N., Kaplan, D. I., Doron, G., de Limoges, D., Bocklisch, C., & Larkum, M. E. (2017, Sep 25). Cortical dendritic activity correlates with spindle-rich oscillations during sleep in rodents. *Nat Commun, 8*(1), 684. 10.1038/s41467-017-00735-w

Shadlen, M. N., & Movshon, J. A. (1999). Synchrony unbound: a critical evaluation of the temporal binding hypothesis. *Neuron, 24*(1), 67-77, 111-125.

Siapas, A. G., & Wilson, M. A. (1998, Nov). Coordinated interactions between hippocampal ripples and cortical spindles during slow-wave sleep. *Neuron, 21*(5), 1123-1128.

Silber, M. H., Ancoli-Israel, S., Bonnet, M. H., Chokroverty, S., Grigg-Damberger, M. M., Hirshkowitz, M., Kapen, S., Keenan, S. A., Kryger, M. H., Penzel, T., Pressman, M. R., & Iber, C. (2007, Mar 15). The visual scoring of sleep in adults. *J Clin Sleep Med, 3*(2), 121-131.

Simić, G., Kostović, I., Winblad, B., & Bogdanović, N. (1997, Mar 24). Volume and number of neurons of the human hippocampal formation in normal aging and Alzheimer's disease. *J Comp Neurol, 379*(4), 482-494. 10.1002/(sici)1096-9861(19970324)379:4<482::aid-cne2>3.0.co;2-z

Skaggs, W. E., & McNaughton, B. L. (1996, Mar 29). Replay of neuronal firing sequences in rat hippocampus during sleep following spatial experience. *Science, 271*(5257), 1870-1873.

Squire, L. R. (1992). Memory and the hippocampus: A synthesis from findings with rats, monkeys and humans. *Psychological Review, 99*, 195-231.

Staba, R. J., Wilson, C. L., Bragin, A., Jhung, D., Fried, I., & Engel, J. (2004). High-frequency oscillations recorded in human medial temporal lobe during sleep. *Annals of Neurology, 56*(1), 108-115. doi:10.1002/ana.20164

Staresina, B. P., Bergmann, T. O., Bonnefond, M., van der Meij, R., Jensen, O., Deuker, L., Elger, C. E., Axmacher, N., & Fell, J. (2015, Nov). Hierarchical nesting of slow oscillations, spindles and ripples in the human hippocampus during sleep. *Nat Neurosci, 18*(11), 1679-1686. 10.1038/nn.4119

Stark, E., Roux, L., Eichler, R., Senzai, Y., Royer, S., & Buzsáki, G. (2014, Jul 16). Pyramidal cell-interneuron interactions underlie hippocampal ripple oscillations. *Neuron, 83*(2), 467-480. 10.1016/j.neuron.2014.06.023

Teleńczuk, B., Dehghani, N., Le Van Quyen, M., Cash, S. S., Halgren, E., Hatsopoulos, N. G., & Destexhe, A. (2017). Local field potentials primarily reflect inhibitory neuron activity in human and monkey cortex. *Scientific reports, 7*, 40211.

Telfeian, A. E., & Connors, B. W. (2003, Jun 5). Widely integrative properties of layer 5 pyramidal cells support a role for processing of extralaminar synaptic inputs in rat neocortex. *Neurosci Lett, 343*(2), 121-124. 10.1016/s0304-3940(03)00379-3

Thyng, K. M., Greene, C. A., Hetland, R. D., Zimmerle, H. M., & DiMarco, S. F. (2016). True colors of oceanography: Guidelines for effective and accurate colormap selection. *Oceanography, 29*(3), 9-13.

Timofeev, I., Grenier, F., Bazhenov, M., Houweling, A. R., Sejnowski, T. J., & Steriade, M. (2002). Short- and medium-term plasticity associated with augmenting responses in cortical slabs and spindles in intact cortex of cats in vivo. *The Journal of Physiology, 542*(2), 583-598. 10.1113/jphysiol.2001.013479

Townsend, R. G., & Gong, P. (2018). Detection and analysis of spatiotemporal patterns in brain activity. *PLoS computational biology, 14*(12), e1006643. 10.1371/journal.pcbi.1006643

Treisman, A. (1999, Sept). Solutions to the binding problem: progress through controversy and convergence. *Neuron, 24*(1), 105-110, 111-125.

Tremblay, R., Lee, S., & Rudy, B. (2016, Jul 20). GABAergic Interneurons in the Neocortex: From Cellular Properties to Circuits. *Neuron, 91*(2), 260-292. 10.1016/j.neuron.2016.06.033

Truccolo, W., Donoghue, J. A., Hochberg, L. R., Eskandar, E. N., Madsen, J. R., Anderson, W. S., Brown, E. N., Halgren, E., & Cash, S. S. (2011, May). Single-neuron dynamics in human focal epilepsy. *Nat Neurosci, 14*(5), 635-641. 10.1038/nn.2782

Uhlhaas, P., Pipa, G., Lima, B., Melloni, L., Neuenschwander, S., Nikolić, D., & Singer, W. (2009, 2009-July-30). Neural synchrony in cortical networks: history, concept and current status [Original Research]. *Front Integr Neurosci, 3*(17). 10.3389/neuro.07.017.2009

Vaz, A. P., Inati, S. K., Brunel, N., & Zaghloul, K. A. (2019, Mar 1). Coupled ripple oscillations between the medial temporal lobe and neocortex retrieve human memory. *Science, 363*(6430), 975-978. 10.1126/science.aau8956

Vaz, A. P., Wittig, J. H., Jr., Inati, S. K., & Zaghloul, K. A. (2020, Mar 6). Replay of cortical spiking sequences during human memory retrieval. *Science, 367*(6482), 1131-1134. 10.1126/science.aba0672

Vicente, R., Gollo, L. L., Mirasso, C. R., Fischer, I., & Pipa, G. (2008). Dynamical relaying can yield zero time lag neuronal synchrony despite long conduction delays. *Proceedings of the National Academy of Sciences, 105*(44), 17157-17162.

von der Malsburg, C. (1999, Sept). The what and why of binding: the modeler's perspective. *Neuron, 24*(1), 95-104, 111-125.

Waxman, S. G., & Swadlow, H. A. (1977). The conduction properties of axons in central white matter. *Prog Neurobiol, 8*(4), 297-324.

Waziri, A., Schevon, C. A., Cappell, J., Emerson, R. G., McKhann, G. M., 2nd, & Goodman, R. R. (2009, Mar). Initial surgical experience with a dense cortical microarray in epileptic patients undergoing craniotomy for subdural electrode implantation. *Neurosurgery, 64*(3), 540-545; discussion 545. 10.1227/01.NEU.0000337575.63861.10

Wilson, M. A., & McNaughton, B. L. (1994, Jul 29). Reactivation of hippocampal ensemble memories during sleep. *Science, 265*(5172), 676-679.

Wittenberg, G. M., & Wang, S. S. (2006, Jun 14). Malleability of spike-timing-dependent plasticity at the CA3-CA1 synapse. *J Neurosci, 26*(24), 6610-6617. 10.1523/jneurosci.5388-05.2006

Wittmann, M. (2015). *Wenn die Zeit stehen bleibt. Kleine Psychologie der Grenzerfahrungen* (1 ed.). Verlag C.H.Beck.

Xuereb, J. H., Perry, R. H., Candy, J. M., Perry, E. K., Marshall, E., & Bonham, J. R. (1991, Jun). Nerve cell loss in the thalamus in Alzheimer's disease and Parkinson's disease. *Brain, 114 (Pt 3)*, 1363-1379.